Journal of Biomedical Photonics & Engineering

by Samara State Aerospace University (SSAU)

Volume 1, Issue 2 (*June 2015*)

Editorial Board

Editor-In-Chief

Valery V. Tuchin - Saratov State University, Russia; Institute of Precision Mechanics and Control RAS, Russia; University of Oulu, Finland; Samara State Aerospace University, Russia

Deputy Editor-In-Chief

Valery P. Zakharov - Samara State Aerospace University, Russia

Editorial Board

Stefan Andersson-Engels (Lund University, Sweden), **Alexey N. Bashkatov** (Saratov State University, Russia), **Ekaterina Borisova** (Academician Emil Djakov Institute of Electronics, Bulgarian Academy of Sciences, Bulgaria), **Wei Chen** (University of Central Oklahoma, USA), **Arthur Chiou** (National Yang-Mind University, Taiwan), **Elina A. Genina** (Saratov State University, Russia), **Min Gu** (Swinburne University, Australia), **Nikolay G. Khlebtsov** (Institute of Biochemistry and Physiology of Plants and Microorganisms RAS, Russia), **Juergen Lademann** (Charite University Clinic, Germany), **Kirill V. Larin** (University of Houston, USA), **Martin Leahy** (University of Galway, Ireland), **Qingming Luo** (Huazhong University of Science and Technology, China), **Stephen J Matcher** (University of Sheffield, Great Britain), **Igor Meglinski** (University of Oulu, Finland), **Vladimir S. Pavelyev** (Image Processing Systems Institute RAS, Russia), **Francesco Pavone** (University of Florence, Italy), **Roberto Pini** (Institute of Applied Physics, Italy), **Igor A. Platonov** (Samara State Aerospace University, Russia), **Juergen Popp** (Institute of Photonic Technology, Germany), **Alexander V. Priezzhev** (Moscow State University, Russia), **David Sampson** (The University of Western Australia, Australia), **Alexander Savitsky** (Institute of Biochemistry RAS, Russia), **Alexander P. Shkurinov** (Moscow State University, Russia), **Peter So** (Massachusetts Institute of Technologies, USA), **Janis Spigulis** (University of Latvia, Latvia), **Ilya V.Turchin** (Institute of Applied Physics RAS, Russia), **Vladimir G. Volostnikov** (N.P.Lebedev Physical Institute, Russia), **Lihong V. Wang** (Washington University, USA), **Ruikang Wang** (University of Washington, USA), **Xunbin Wei** (Shanghai Jiao Tong University, China), **Dan Zhu** (Britton Chance Center for Biomedical Photonics, Huazhong University of Science and Technology, China).

Postal address:

39B Lukacheva st., room #301

Samara 443086, Russian Federation

© 2015 SSAU

Contents

Review papers

Tissue Optics and Photonics: Light-Tissue Interaction 98
by V.V. Tuchin

Regular papers

Dendritic crystallogram images classification 135
by R.A. Paringer, A.V. Kupriyanov, and N.Y. Ilyasova

Zernike phase spatial filter for measuring the aberrations of the optical structures of the eye 146
by S.N. Khonina, V.V. Kotlyar, and D.V. Kirsh

Compact optical tweezer with the capability of dynamic control 154
by A. Korobtsov, S. Kotova, N. Losevsky, A. Mayorova, and S. Samagin

Backscattering spectroscopy for assessing skin tumor 164
by V.P. Zakharov, P.E. Timchenko, E.V. Timchenko, L.A. Zherdeva, S.V. Kozlov, and A.A. Moryatov

The combination of optical coherence tomography and Raman spectroscopy for tissue characterization 169
by K.D. Egodage, S. Dochow, T.W. Bocklitz, O. Chernavskaia, C. Matthäus, M. Schmitt, and J. Popp

© 2015 SSAU

Tissue Optics and Photonics: Light-Tissue Interaction

Valery V. Tuchin[1,2,3]
[1] Saratov State University, 83 Astrakhanskaya str., Saratov 410012, Russia
[2] Institute of Precision Mechanics and Control RAS, 24 Rabochaya str., Saratov 410028, Russia
[3] Samara State Aerospace University (SSAU), 34 Moskovskoye Shosse, Samara 443086, Russia

e-mail: tuchinvv@mail.ru

Abstract. This is the second section of the review-tutorial paper describing fundamentals of tissue optics and photonics. As the first section of the paper was mostly devoted to description of biological tissue structures and their specificity related to interactions with light [1], this section 3 describes light-tissue interactions themselves that are caused by tissue dispersion, scattering, and absorption properties, including light reflection and refraction, absorption, elastic, and quasi-elastic scattering. The major tissue absorbers and modes of elastic scattering, including Rayleigh and Mie scattering, will be presented. © 2015 Samara State Aerospace University (SSAU).

Keywords: tissue optics; multiple scattering; quasi-elastic scattering; Doppler effect; absorption; index of refraction; random phase screen; speckles; optical coherence tomography (OCT); diffusion wave spectroscopy; polarized light; optical clearing

Paper #2469 received 2015.05.30; accepted for publication 2015.06.29; published online 2015.06.30.

References

1. V. V. Tuchin, "Tissue Optics and Photonics: Biological Tissue Structures," J. of Biomedical Photonics & Eng. 1(1), 3-21 (2015).
2. L. V. Wang. and H.-I. Wu, Biomedical Optics: Principles and Imaging, Wiley-Intersience, Hoboken, NJ (2007).
3. R. Splinter, and B. A. Hooper, An Introduction to Biomedical Optics, CRC Press, Taylor & Francis Group, NY, London (2007).
4. T. Vo-Dinh (ed.), Biomedical Photonics Handbook, 2nd ed., CRC Press, Boca Raton (2014).
5. V. V. Tuchin, Tissue Optics: Light Scattering Methods and Instruments for Medical Diagnosis, 3rd ed., SPIE Press, Bellingham, WA (2015).
6. M. Born, and E. Wolf, Principles of Optics, 7th ed., Cambridge Univ. Press, Cambridge (1999).
7. G. S. Landsberg, Optics, 6th ed., Fizmatlit, Moscow (2006) [in Russian].
8. A. Akhmanov, S. Y. Nikitin, Physical Optics, Oxford University Press, Oxford (1997).
9. V. V. Tuchin, Lasers and Fiber Optics in Biomedical Science, 2nd ed., Fizmatlit, Moscow (2010) [in Russian].
10. V. V. Tuchin, "Light scattering study of tissues," Physics – Uspekhi 40(5), 495–515 (1997).
11. V. V. Tuchin (ed.), Handbook of Photonics for Biomedical Science, CRC Press, Taylor & Francis Group, London (2010).
12. A. Wax, and V. Backman (eds.), Biomedical Applications of Light Scattering, McGraw-Hill, NY (2010).
13. D. A. Boas, C. Pitris, and N. Ramanujam (eds.), Handbook of Biomedical Optics, CRC Press, Taylor & Francis Group, London (2011).
14. V. V. Tuchin, Dictionary of Biomedical Optics and Biophotonics, SPIE Press, Bellingham, WA (2012).
15. J. Popp, V. Tuchin, A. Chiou, and S. H. Heinemann (eds.), Handbook of Biophotonics: Basics and Techniques, vol.1, Wiley-VCH Verlag GmbH & Co. KGaA, Weinheim (2011).
16. J. Popp, V. V. Tuchin, A. Chiou, and S. H. Heinemann (eds.), Handbook of Biophotonics: Photonics for Health Care, vol. 2, WILEY-VCH Verlag GmbH & Co. KGaA, Weinheim (2011).
17. A. N. Bashkatov, E. A. Genina, and V. V. Tuchin, "Optical properties of skin, subcutaneous, and muscle tissues: a review," J. Innov. Opt. Health Sci. 4(1), 9–38 (2011).
18. S. L. Jacques, "Optical properties of biological tissues: A review," Phys. Med. Biol. 58(14), R37–R61 (2013).
19. R. K. Wang, and V. V. Tuchin, Advanced Biophotonics: Tissue Optical Sectioning, CRC Press, Taylor & Francis Group, London (2013).

20. S. L. Jacques, "Probing the nano-, micro-, and meso-scale structures of biological tissues using light scattering," International Conference on Laser Applications in Life Sciences (LALS), June 29 - July 2, Ulm, Germany (2014).
21. S. L. Jacques, "Quick analysis of optical spectra to quantify epidermal melanin and papillary dermal blood content of skin," J. Biophotonics 8(4), 309–316 (2015).
22. C. F. Bohren, and D.R. Huffman, Absorption and Scattering of Light by Small Particles, Wiley, NY (1983).
23. M. I. Mishchenko, L.D. Travis, and A.A. Lacis, Scattering, Absorption, and Emission of Light by Small Particles, Cambridge Univ. Press, Cambridge (2002).
24. R. G. Johnston, S. B. Singham, and G. C. Salzman, "Polarized light scattering" in Comments Mol. Cell. Biophys. 5(3), Gordon and Breach Sci. Publ. Inc., 171–192 (1988).
25. K. Frank, and M. Kessler (eds.), Quantitative Spectroscopy in Tissue, pmi Verlag, Frankfurt am Main (1992).
26. H. C. van de Hulst, Light Scattering by Small Particles, Wiley, New York (1957); reprint, Dover, NY (1981); Multiple Light Scattering. Tables, Formulas and Applications, Academic Press, NY (1980).
27. G. C. Beck, N. Akgun, A. Rück, and R. Steiner, "Design and characterization of a tissue phantom system for optical diagnostics," Lasers Med. Sci. 13, 160–171 (1998).
28. V. V. Tuchin (ed.), Handbook of Optical Biomedical Diagnostics, SPIE Press, Bellingham, Washington (2002).
29. E. P. Zege, A. P. Ivanov, and I. L. Katsev, Image Transfer through a Scattering Medium, Springer-Verlag, NY (1991).
30. A. Ishimaru, Wave Propagation and Scattering in Random Media, IEEE Press, NY (1997).
31. M. I. Mishchenko, L. D. Travis, and A. A. Lacis, Multiple Scattering of Light by Particles: Radiative Transfer and Coherent Backscattering, Cambridge University Press, NY (2006).
32. A. A. Kokhanovsky (ed.), Light Scattering Reviews 4: Single Light Scattering and Radiative Transfer, Springer, Heidelberg (2009).
33. A. A. Kokhanovsky (ed.), Light Scattering Reviews 5: Single Light Scattering and Radiative Transfer, Springer, Heidelberg (2010).
34. R. Graaff, J. G. Aarnoudse, J. R. Zijp, P. M. A. Sloot, F. F. M. de Mul, J. Greve, and M. H. Koelink, "Reduced light scattering properties for mixtures of spherical particles: a simple approximation derived from Mie calculations," Appl. Opt. 31, 1370–1376 (1992).
35. G. Müller, B. Chance, R. Alfano, et al. (eds.), Medical Optical Tomography: Functional Imaging and Monitoring, SPIE Inst. Adv. Opt. Techn. IS11, SPIE Press, Bellingham, WA (1993).
36. M. S. Patterson, "Noninvasive measurement of tissue optical properties: current status and future prospects" in Comments Mol. Cell. Biophys. 8, Gordon and Breach Sci. Publ. Inc., 387–417 (1995).
37. B. Chance, M. Cope, E. Gratton, N. Ramanujam, and B. Tromberg, "Phase measurement of light absorption and scatter in human tissue," Rev. Sci. Instrum. 69(10), 3457–3481 (1998).
38. O. Minet, G. Müller, and J. Beuthan (eds.), Selected Papers on Optical Tomography, Fundamentals and Applications in Medicine, MS147, SPIE Press, Bellingham, WA (1998).
39. J. C. Dainty (ed.), Laser Speckle and Related Phenomena, 2nd ed., Springer-Verlag, NY (1984).
40. J. W. Goodman, Statistical Optics, Wiley-Interscience Publication, NY, et al. (1985).
41. J. W. Goodman, Introduction to Fourier Optics, McGraw-Hill, NY (1996).
42. J. W. Goodman, Speckle Phenomena in Optics: Theory and Applications, Roberts & Co., Englewood, CO (2007).
43. P. Zakharov, and F. Scheffold, "Advances in dynamic light scattering techniques" in Light Scattering Reviews 4: Single Light Scattering and Radiative Transfer, A.A. Kokhanovsky (ed.), Springer, Heidelberg, 433–468 (2009).
44. A. P. Shepherd, and P.Å. Öberg (eds.), Laser Doppler Blood Flowmetry, Kluwer, Boston (1990).
45. B. J. Berne, and R. Pecora, Dynamic Light Scattering: with Applications to Chemistry, Biology, and Physics, Dover Publications, Inc., Mineola, NY (2000).
46. D. A. Boas and K. Dunn, "Laser speckle contrast imaging in biomedical optics," J. Biomed. Opt. 15(1), 011109 (2010).
47. V. V. Tuchin (ed.), Advanced Optical Cytometry: Methods and Disease Diagnoses, Wiley-VCH Verlag GmbH & Co. KGaA, Weinheim (2011).
48. V. V. Tuchin (ed.), Coherent-Domain Optical Methods: Biomedical Diagnostics, Environmental Monitoring and Material Science, 2nd ed., 2 vols., Berlin, Heidelberg, N.Y., Springer-Verlag (2013).
49. M. J. Leahy (ed.), Microcirculation Imaging, Wiley-VCH Verlag GmbH & Co. KGaA, Weinheim (2012).
50. S. M. Daly, and M. J. Leahy, "'Go with the flow:' A review of methods and advancements in blood flow imaging," J. Biophotonics, 6(3), 217–255 (2013).
51. N. Yokoi, Y. Shimatani, M. Kyoso, H. Funamizu, and Y. Aizu, "Imaging of blood flow and blood concentration change in a frame rate using laser speckle: Methods for image analysis," Opt. Laser Tech. 64, 352–362 (2014).

52. H. M. Varma, C. P. Valdes, A. K. Kristoffersen, J. P. Culver, and T. Durduran, "Speckle contrast optical tomography: A new method for deep tissue three-dimensional tomography of blood flow," Biomed. Opt. Express 5(4), 1275-1289 (2014).
53. P. Farzam, and T. Durduran, "Multidistance diffuse correlation spectroscopy for simultaneous estimation of blood flow index and optical properties," J. Biomed. Opt. 20(5), 055001 (2015).
54. D. A. Zimnyakov, J. D. Briers, and V. V. Tuchin, "Speckle technologies for monitoring and imaging of tissuelike phantoms," in Handbook of Optical Biomedical Diagnostics, V. V. Tuchin (ed.), SPIE Press, Bellingham, Washington, 987–1036 (2002).
55. I. V. Fedosov and V. V. Tuchin, "Laser Doppler and speckle techniques for bioflow measurements," in Coherent-Domain Optical Methods: Biomedical Diagnostics, Environmental Monitoring and Material Science, 2nd ed., V. V. Tuchin (ed.), Springer-Verlag Berlin, Heidelberg, NY, 487–564 (2013).
56. A. V. Priezzhev, V. V. Tuchin, and L. P. Shubochkin, Laser Diagnostics in Biology and Medicine, Nauka, Moscow (1989) [in Russian].
57. G. Popescu, "Quantitative phase imaging of nanoscale cell structure and dynamics," in Methods in Nano Cell Biology, B. P. Jena (ed.), Methods in Cell Biology 90, Academic Press, NY, 87–115 (2008).
58. G. Popescu, Quantitative Phase Imaging of Cells and Tissues, McGraw-Hill, NY (2011).
59. V. P. Ryabukho, "Diffraction of interference fields on random phase objects," in Coherent-Domain Optical Methods: Biomedical Diagnostics, Environmental and Material Science, V. V. Tuchin (ed.), Kluwer Academic Publishers, Boston, 235 –318 (2004).
60. A. Serov, and T. Lasser, "High-speed laser Doppler perfusion imaging using an integrating CMOS image sensor," Opt. Express 13(17), 6416–6428 (2005).
61. I. V. Meglinski, and V. V. Tuchin, "Diffusing wave spectroscopy: Application for blood flow diagnostics," in Coherent-Domain Optical Methods: Biomedical Diagnostics, Environmental Monitoring and Material Science, 2nd ed., V. V. Tuchin (ed.), Springer-Verlag, Berlin, Heidelberg, NY, 149–167 (2013).
62. W. A. Shurkliff, Polarized Light. Production and Use, Harvard Univ., Cambridge, Mass (1962).
63. W. A. Shurkliff, and S. S. Ballard, Polarized Light, Van Nostrand, Princeton (1964).
64. D. S. Kliger, J. W. Lewis, and C. E. Randall, Polarized Light in Optics and Spectroscopy, Academic, Boston (1990).
65. E. Collet, Polarized Light. Fundamentals and Applications, Dekker, NY (1993).
66. R. M. A. Azzam, and N. M. Bashara, Ellipsometry and Polarized Light, Elsevier Science, Amsterdam (1994).
67. A. Z. Dolginov, Y. N. Gnedin, and N.A. Silant'ev, Propagation and Polarization of Radiation in Cosmic Media, Gordon and Breach, Basel (1995).
68. C. Brosseau, Fundamentals of Polarized Light: A Statistical Optics Approach, Wiley, NY (1998).
69. M. I. Mishchenko, J. W. Hovenier, and L. D. Travis (eds.), Light Scattering by Nonspherical Particles, Academic Press, San Diego (2000).
70. A. A. Kokhanovsky, Polarization Optics of Random Media. Springer-Verlag, Berlin, Heidelberg, NY (2003).
71. V. V. Tuchin, L. V. Wang, and D. A. Zimnyakov, Optical Polarization in Biomedical Applications, Springer, NY (2006).
72. L. V. Wang, G. L. Coté, and S. L. Jacques (eds.), "Special Section on Tissue Polarimetry," J. Biomed. Opt. 7(3), 278–397 (2002).
73. S. L. Jacques, J. C. Ramella-Roman, and K. Lee, "Imaging skin pathology with polarized light," J. Biomed. Opt. 7(3), 329–340 (2002).
74. J. Ramella-Roman, S. Prahl, and S. Jacques, "Three Monte Carlo programs of polarized light transport into scattering media: part I," Opt. Express 13(12), 4420–4438 (2005).
75. J. Ramella-Roman, S. Prahl, and S. Jacques, "Three Monte Carlo programs of polarized light transport into scattering media: part II," Opt. Express 13(25), 10392–10405 (2005).
76. N. Ghosh, and I. A. Vitkin, "Concepts, challenges and applications of polarized light in biomedicine: A tutorial review," J. Biomed. Opt. 16(11), 110801 (2010).
77. B. Kunnen, C. Macdonald, A. Doronin, S. Jacques, M. Eccles, and I. Meglinski, "Application of circularly polarized light for non-invasive diagnosis of cancerous tissues and turbid tissue-like scattering media," J. Biophotonics 8(4), 317–323 (2015).
78. V. V. Tuchin,"Optical immersion as a new tool to control optical properties of tissues and blood," Laser Phys. 15(8), 1109–1136 (2005).
79. V. V. Tuchin, "Optical clearing of tissue and blood using immersion method," J. Phys. D: Appl. Phys. 38, 2497–2518 (2005).
80. V. V. Tuchin, Optical Clearing of Tissues and Blood, PM 154, SPIE Press, Bellingham, WA (2006).
81. V. V. Tuchin, "A clear vision for laser diagnostics," IEEE J. Select. Tops. Quant. Electr. 13(6), 1621–1628 (2007).
82. V. V. Tuchin (ed.), Handbook of Optical Sensing of Glucose in Biological Fluids and Tissues, CRC Press, Taylor & Francis Group, London (2009).

83. E. A. Genina, A. N. Bashkatov, and V. V. Tuchin, "Tissue optical immersion clearing," Expert Rev. Med. Devices 7(6), 825–842 (2010).
84. E. A. Genina, A. N. Bashkatov, K. V. Larin, and V. V. Tuchin, "Light–tissue interaction at optical clearing" in Laser Imaging and Manipulation in Cell Biology, F.S. Pavone (ed.), Wiley-VCH Verlag GmbH & Co. KGaA, Weinheim, 115–164 (2010).
85. K. V. Larin, M. G. Ghosn, A. N. Bashkatov, E. A. Genina, N. A. Trunina, and V. V. Tuchin, "Optical clearing for OCT image enhancement and in-depth monitoring of molecular diffusion," IEEE J. Select. Tops. Quant. Electr. 18 (3) 1244–1259 (2012).
86. D. Zhu, K. V. Larin, Q. Luo, and V. V. Tuchin, "Recent progress in tissue optical clearing," Laser Photonics Rev. 7(5), 732–757 (2013).
87. D. Zhu, Q. Luo, and V. V. Tuchin, "Tissue Optical Clearing," in Advanced Biophotonics: Tissue Optical Sectioning, R. K. Wang, and V. V. Tuchin (eds.), CRC Press, Taylor & Francis Group, Boca Raton, London, NY, 621–672 (2013).
88. R. K. Wang, and V.V. Tuchin, "Optical coherence tomography: light scattering and imaging enhancement," in Coherent-Domain Optical Methods: Biomedical Diagnostics, Environmental Monitoring and Material Science, 2nd ed., V. V. Tuchin (ed.), Springer-Verlag, Berlin, Heidelberg, NY, 665–742 (2013).
89. J. Wang, Y. Zhang, P. Li, Q. Luo, and D. Zhu, "Review: Tissue Optical Clearing Window for Blood Flow Monitoring (Invited Paper)," IEEE J. Select. Tops Quant. Electr. 20(2), 6801112 (2014).
90. O. Nadiarnykh, and P. J. Campagnola, "SHG and optical clearing," in Second Harmonic Generation Imaging, F.S. Pavone, and P.J. Campagnola (eds.), CRC Press, Taylor & Francis Group, Boca Raton, London, NY, 169−189 (2014).
91. E. A. Genina, A. N. Bashkatov, Y. P. Sinichkin, I. Y. Yanina, and V. V. Tuchin, "Optical clearing of biological tissues: prospects of application in medical diagnostics and phototherapy," J. of Biomedical Photonics & Eng. 1(1), 22−58 (2015).
92. X.-C. Zhang, and J. Xu, Introduction to THz Wave Photonics, Springer, NY (2010).
93. M. M. Nazarov, A. P. Shkurinov, V. V. Tuchin, and X.-C. Zhang, "Terahertz tissue spectroscopy and imaging" in Handbook of Photonics for Biomedical Science, V. V. Tuchin (ed.), CRC Press, Taylor & Francis Group, London, 591–617 (2010).

Contents

1 Introduction
2 Biological tissue structures
  2.1 General definitions and characteristics
  2.2 Soft tissues
  2.3 Hard tissues
  2.4 Tissue structural anisotropy
  2.5 Blood, lymph and other bioliquids
3 Light-tissue interaction: absorption, scattering and polarization
  3.1 Light reflection and refraction
  3.2 Light absorption and elastic scattering
    3.2.1 Absorption and tissue absorbers
    3.2.2 Scattering – basic definitions
    3.2.3 Rayleigh scattering
    3.2.4 Mie scattering
    3.2.5 Multiple scattering
  3.3 Scattering of the coherent light
    3.3.1 Random phase screen concept and speckle formation
    3.3.2 Speckle interferometry
    3.3.3 Low-coherent light interferometry – optical coherence tomography
  3.4 Dynamic light scattering
    3.4.1 Quasi-elastic light scattering (QELS) and Doppler effect
    3.4.2 Dynamic speckles
    3.4.3 Speckle pattern blurring effect – full-field velocity measurements
  3.5 Diffusion wave spectroscopy
  3.6 Interaction of the polarized light with tissues
    3.6.1 Definitions
    3.6.2 Single scattering and quasi-ordered tissues
    3.6.3 Multiple scattering
  3.7 Refractive index and controlling of light interaction with tissues

3 Light-tissue interaction: absorption, scattering and polarization

3.1 Light reflection and refraction

A biological tissue is a dielectric medium whose average refractive index is higher than that of air [1-5]. Thus at interaction with tissue surface the light radiation is able to undertake partial reflection at the tissue/air interface (Fresnel reflection), while the remaining part penetrates the tissue (see Fig. 3.1a) [6-8]. Light refraction is the change in direction of a ray of light when passing obliquely from one medium into another in which the light speed (refractive index) is different. Light refraction is characterized by the relative index of refraction, m, of these two media with n_1 and n_2 indices, $n_2 > n_1$. For different human tissues and tissue components, refractive index (RI) in the visible/NIR wavelength range varies from a value a little bit higher than for water due to influence of some organic

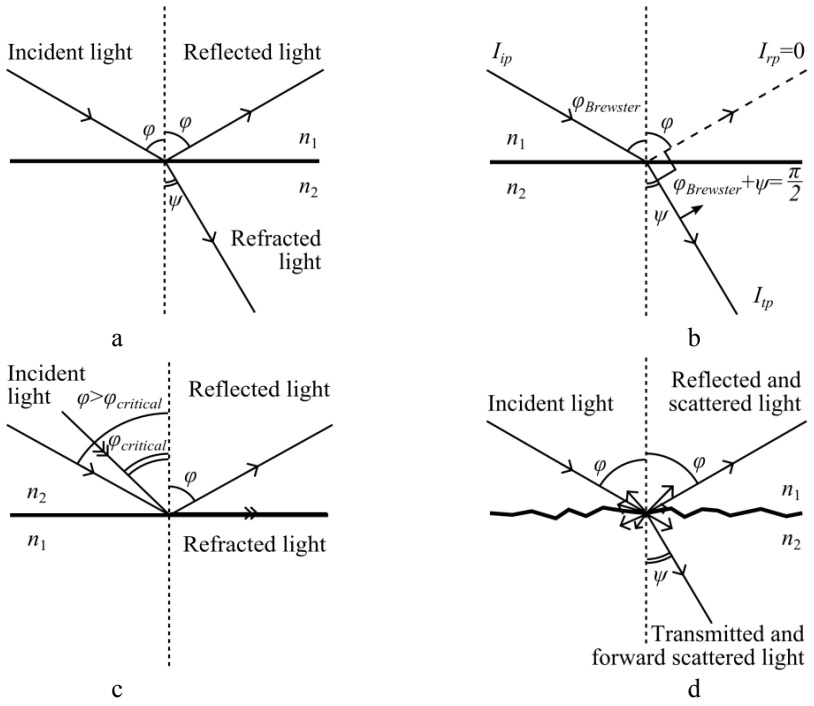


Fig. 3.1 Light interaction with a nonscattering tissue with mean index of refraction $n_2 \equiv n_{tissue}$, n_1 is the index of refraction of a surrounding medium; $n_{tissue} > n_1$: (a) illustrates light reflection by and transmission through the flat interface of a tissue surface and surrounding medium; (b) illustrates the Brewster angle $\varphi_{Brewster}$ – the angle of incidence at which light polarized in the incident light plane (p) is perfectly transmitted; for skin *stratum corneum* with $n_2 \cong 1.5$ and $n_1=1$, $\varphi_{Brewster} \cong 57^o$; (c) illustrates total internal reflection of light when it goes from a medium with a higher index of refraction (n_2) to a medium with the lower one (n_1) in the case of a flat interface between two nonscattering media; for skin *stratum corneum* with $n_2 \cong 1.5$ and $n_1=1$, $\varphi_{critical} \cong 45^o$; (d) illustrates light reflection, transmission and scattering by rough interface of a scattering tissue and surrounding media.

components, $n_2 \cong 1.35$ for interstitial fluid, to 1.62 for tooth enamel.

In Fig. 3.1b, p polarization denotes that the electric field is polarized parallel to the plane of incidence (the same plane as the incident, reflected and transmitted rays). As well as s polarization denotes that the electric field is polarized perpendicular the plane of incidence. To describe polarized light reflectance (R_p and R_s) by and transmittance (T_p and T_s) through a flat (not rough) interface of transparent (not scattering) tissue Fresnel formulas can be used [6-8]

$$R_p = \frac{\tan^2(\varphi - \psi)}{\tan^2(\varphi + \psi)}, \tag{3.1}$$

$$T_p = \frac{\sin 2\varphi \sin 2\psi}{\sin^2(\varphi + \psi)\cos^2(\varphi - \psi)}, \tag{3.2}$$

$$R_s = \frac{\sin^2(\varphi - \psi)}{\sin^2(\varphi + \psi)}, \tag{3.3}$$

$$T_s = \frac{\sin 2\varphi \sin 2\psi}{\sin^2(\varphi + \psi)}, \tag{3.4}$$

where R_p, R_s and T_p, T_s are reflectance and transmittance, respectively, or the ratios of the reflected (I_{rp}, I_{rs}) and transmitted (I_{tp}, I_{ts}) intensities to the incident intensity for each polarization state in the incident light plane (p) and the orthogonal plane (s), I_{ip} and I_{is}, respectively; φ is the incident angle (equal to reflection angle) and ψ is the angle of refraction; these angles are defined by the indices in accordance with the Snell's law

$$n_1 \sin\varphi = n_2 \sin\psi; \tag{3.5}$$

and can be expressed in terms of the relative index of refraction m

$$\frac{n_2}{n_1} = m. \tag{3.6}$$

For the specific light incident angles, the reflectivity and transmittance are described by the following formulas:

At the normal incidence to the surface ($\varphi = 0^o$),

$$R_p = R_s = R = \left(\frac{m-1}{m+1}\right)^2, \tag{3.7}$$

$$T_p = T_s = T = \frac{4m}{\left(m+1\right)^2}; \quad (3.8)$$

At the incidence angle that produces a rectangular angle between the reflected and refracted rays which is called the Brewster angle ($\varphi_{Brewster} + \psi = 90^o$), or

$$\varphi_{Brewster} = arctan\, m, \quad (3.9)$$

$R_p = 0$, $R_s \neq 0$, i.e., this is an angle of incidence at which light with a particular polarization *p* is perfectly transmitted, at other angles the reflected light is partially polarized (see Fig. 3.1b);

At the incidence of light from the medium with a higher RI (n_2) into the medium with the lower RI (n_1) (see Fig. 3.1c) a so called critical angle $\varphi_{critical}$ exists for which if incident angle $\varphi \geq \varphi_{critical}$ total internal reflection (no transmitted light) is created

$$\varphi_{critical} = arcsin\, m. \quad (3.10)$$

All these formulas are applicable only to homogeneous media with flat interface between. Thus they could be applied only locally for a limited number of tissues such as healthy eye cornea, lens and vitreous body (see Fig. 2.6) [1]. However, the major types of tissues are optically inhomogeneous (turbid) and absorptive multilayered media with rough interfaces. In that case light scattering from the interface and from bulk of a tissue will influence light reflection and transmission with the redistribution of light in the space (see Fig. 3.1d).

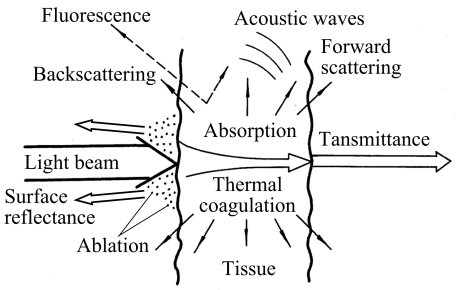


Fig. 3.2 Schematic representation of different modes of light interaction with tissues [9].

Actually, in tissues multiple scattering and absorption processes are responsible for light beam broadening and eventual decay as it travels through a tissue, whereas bulk scattering is a major cause of the dispersion of a large fraction of radiation in the backward direction (see Figs. 3.2 and 3.3) [9]. Therefore light propagation within a tissue depends on the scattering and absorption properties of its components: cells, cell organelles, and various fiber structures. The size, shape, and density of these structures, their refractive index, and the polarization state of the incident light predetermine the character of light propagation in tissues.

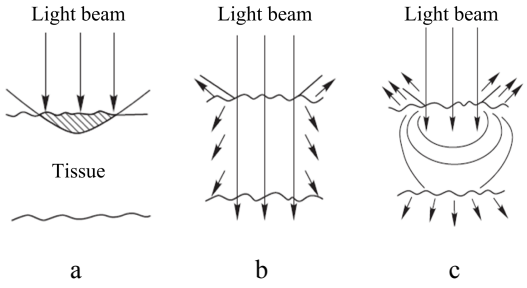


Fig. 3.3 Light beam absorption and scattering by a tissue: a — absorption prevails, is typical for UV or MIR/FIR radiation, no light propagates into tissue; b — absorption and scattering are approximately equal to each other, is typical for some range in the NIR, light beam propagates well with some amount of scattered radiation; c — scattering prevails, is typical for visible and NIR, a significant light beam broadening with diffusive irradiation of large tissue volume [9].

3.2 Light absorption and elastic scattering

3.2.1 Absorption and tissue absorbers

The process of light absorption is the transformation of light energy to some other form of energy, i.e. heat, sound, fluorescence as the light transverses tissue. Commonly an absorbing medium consists of absorption centers that are particles or molecules that absorb light. To characterize absorption of a medium an absorption coefficient μ_a is introduced as the reciprocal of the distance *d* over which light of intensity I_0 is attenuated to $I(d) = \frac{I_0}{e} \approx 0.37 I_0$, which follows from the exponential law for light propagation in a tissue layer of thickness *d* (Fig.3.4) [2-5]

$$I(d) = I_0\, exp(-\mu_a d), \quad (3.11)$$

where $I(d)$ is the intensity of transmitted light, W/cm^2; μ_a is typically expressed in cm^{-1}.

Behind this definition is a fundamental process of photon absorption that is characterized by an effective cross section, i.e., the ability of a molecule to absorb a photon of a particular wavelength. Although the units are given as an area, it does not refer to an actual size area, at least partially because the density or state of the target molecule will affect the probability of absorption. Quantitatively, the number dN of photons absorbed, between the points x and x + dx along the path of a light beam is the product of the number N of photons penetrating to depth x multiplied by the absorption cross section σ_{abs} (cm^2) and by the number of absorbing molecules per unit volume ρ_M (cm^{-3}) (Fig.3.4):

$$\frac{dN}{dx} = -\rho_M \sigma_{abs} N, \quad (3.12)$$

where

$$\mu_a = \rho_M \sigma_{abs}. \qquad (3.13)$$

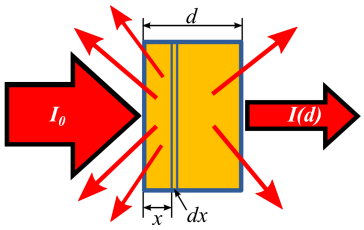


Fig. 3.4 Light beam attenuation due to absorption and scattering.

In spectroscopy a few terms are commonly used, such as absorbance that is the ratio of the absorbed light intensity to the incident intensity, thus, it is a dimensionless quantity, and absorption spectrum that is the spectrum formed by light that has passed through a medium in which light of certain wavelengths was absorbed.

The wavelength dependent optical depth τ_λ which is defined as,

$$\tau_\lambda = \ln\left(\frac{I_0}{I}\right) = \mu_a d = \varepsilon_\lambda c_a d\,, \qquad (3.14)$$

is also often used. Here ε_λ is the extinction coefficient at the wavelength λ in L/(mmol·cm), c_a is the concentration of absorbing substance in mmol/L, and d is in cm.

Absorption spectra can be also expressed in terms of the wavelength dependence of absorption coefficient. Such UV-visible-IR spectra for the major tissue absorbers (chromophores): water, lipids, oxy- and deoxyhemoglobin are presented in Fig. 3.5. The diagnostic/therapeutic spectral window, where tissue absorption is minimal and light penetrates deeper into a tissue, is found between 700 nm and 1100 nm, and two more narrow and less transparent windows are around 1300 nm and 1600 nm. Because water is the major component of any tissue, the absorption coefficient of water is often dominates in the total absorption coefficient of a tissue in a particular wavelength range, especially in the IR (see Fig. 3.5).

Absorption is only one way by which light can interact with the tissue to induce photothermal and photochemical effects followed up by a chain of biological effects [2-5, 10-21]. Absorption of the UV and visible/NIR light in tissue is due to electronic excitation of aromatic or conjugated unsaturated chromophores. A chromophore is a chemical that absorbs light with a characteristic spectral pattern. There are many kinds of chromophores in the tissue, but a few major chromophores predominantly determine the optical absorption within each tissue layer. As an example, spectral ranges of absorption of the main human skin chromophores are presented in Fig.3.6. Proteins found in the epidermis contain the aromatic amino acids tryptophan and tyrosine which have a characteristic absorption band near 270–280 nm; urocanic acid and the nucleic acids also contribute to this absorption band with a maximum near 260–270 nm. Epidermal melanin plays an important role in limiting the penetration depth of light in the skin: it effectively absorbs at the wavelengths from 300 to 1000 nm, but the strongest absorption occurs at shorter wavelengths, in the near UV spectral range.

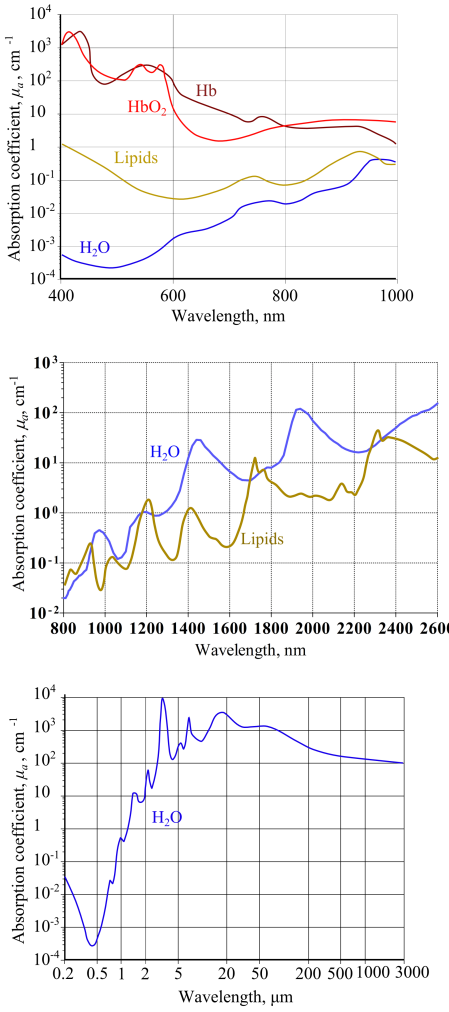


Fig. 3.5 Absorption spectra (expressed in terms of absorption coefficient, μ_a, cm^{-1}) of the main tissue chromophores: Visible-NIR range (water – H_2O, Lipids, oxyhemoglobin – HbO_2, deoxyhemoglobin – Hb) (a); NIR (water – H_2O, Lipids – in the form of human fat) (b); UV-visible-IR (water) (c) [2-5].

The same as for any soft tissue in the IR spectral range, the skin absorption is essentially determined by the absorption of water contained in the skin (see Fig. 3.5). The oxyhemoglobin, deoxyhemoglobin, bilirubin, carotenoids and porphyrins are the major chromophores of skin derma (see Fig. 3.6) [2-5, 10-21]. The oxyhemoglobin has its strongest absorption band at 415 nm (Soret band), and it has two secondary absorption

bands at 542 and 577 nm (Q-bands). The deoxyhemoglobin has a primary absorption band at 430 nm and it has a single secondary absorption band at 555 nm. Both hemoglobins exhibit the lowest absorption at wavelengths longer than 620 nm. The bilirubin has two relatively broad absorption bands near 330 and 460 nm.

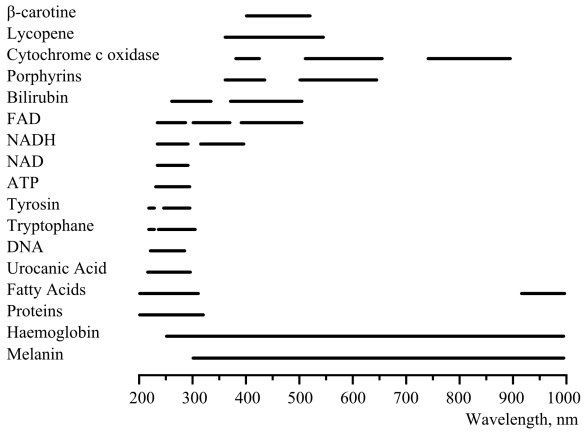


Fig. 3.6 Spectral ranges of absorption of the main human skin and other tissue chromophores; FAD – flavin dinucleotide, NADH – the reduced form of coenzyme nicotinamide adenine dinucleotide (NAD), ATP – adenosine triphosphate.

Porphyrin–based fundamental biological representatives in tissues include not only hemoglobin but also other heme (iron contained) proteins, such as myoglobin and cytochromes, and vitamin B-12 (cobalt contained), and several others. Heme proteins serve many roles, like O_2 storage and transport (haemoglobin and myoglobin), electron transport (cytochromes *b* and *c*), and O_2 activation and utilization (cytochrome c oxidase). As shown in Fig. 3.5a, the UV/visible absorption spectrum of the highly conjugated porphyrin macrocycle exhibits an intense feature (absorption coefficient ~$3\times10^3 cm^{-1}$) at about 400 nm (the "Soret" band), followed by several weaker absorptions (Q-bands) at higher wavelengths (from 450 to 700 nm for different heme proteins).

The enzyme cytochrome c oxidase (or cytochrome complex IV, or cytochrome-aa_3) is a large transmembrane protein complex located within the cell mitochondria. It catalyzes the final step of the respiratory chain in which oxygen is reduced to water. The enzyme contains two copper centers, denoted CuA and CuB. When the enzyme is oxidized, the CuA center is responsible for the distinctive broad absorption band around 820–830 nm. This band disappears when the enzyme is reduced, which allows one by measuring the amplitude of the band to track oxygen utilization directly to the site of ATP synthesis.

Myoglobin is found in muscle and its high affinity for oxygen means that it does not offload its oxygen until very low tissue oxygen pressures are reached. In muscle it serves as a reservoir to store and then slowly release the oxygen delivered by blood hemoglobin. The NIR absorption spectrum of myoglobin is essentially identical to that of hemoglobin, so that it is not possible to monitor it independently without resorting to a supplementary technique.

3.2.2 Scattering – basic definitions

Tissues are not only absorbing but also inhomogeneous media with different levels of organization that include cells, cell organelles and inclusions (see Figs. 2.2 [1] and 3.7), and different fiber and tubular/lamellar structures (see Figs. 2.5-2.11) [1]. In view of the great diversity and structural complexity of tissues, the development of an adequate optical model accounting for the scattering and absorption of light is often the most complex step of a study [2-5, 10-21]. Many tissues are composed of structures with a wide range of sizes (see Fig. 3.7), and can be represented as a system of discrete scattering particles. Such model has been used to describe the angular dependence of the intensity and polarization properties of scattered radiation. Blood is one of the biological examples of a disperse system that entirely corresponds to the model of discrete particles.

Biological media are often modeled as ensembles of homogeneous spherical particles with refractive index higher than surroundings (see Fig. 3.8), since many cells, cell organelles and biological macromolecules are close in shape to spheres or ellipsoids [2-5, 10-21]. A system of noninteracting spherical particles is the simplest tissue model. The Rayleigh and Mie theories or their combination are basic to calculate tissue scattering properties. In particular, Mie theory rigorously describes the diffraction (elastic scattering) of light by a spherical particle. The advances of this theory account the structures of the spherical particles, namely, the multilayered spheres and the spheres with radial nonhomogeneity, anisotropy, and optical activity.

For connective tissue which composed of fiber structures, a system of long cylinders is the most appropriate model to describe light scattering. Muscular tissue, skin dermis, *dura mater*, eye cornea and sclera belong to this type of tissue formed essentially by collagen fibrils. The solution of the problem of light scattering by a single homogeneous or multilayered cylinder is also well understood.

At transport (travel) in the inhomogeneous (turbid) medium with absorption a photon (light wave) changes its direction (wave vector) due to reflection, refraction, and diffraction on microscopic internal structures, and can be absorbed by an appropriate molecule on its way [2-5, 10-21]. Such structures which are smaller or comparable with the wavelength of the propagating light are called commonly scatterers and light scattering means change in direction of light propagation in a turbid medium. There are a number of parameters that describe scattering process. Scattering angle is related to photon scattered by a particle so that its trajectory is deflected by a deflection (scattering) angle θ in the scattering plane and by an azimuthal angle of scattering φ (0 to 2π) in the plane perpendicular to the scattered photon trajectory (Fig. 3.9). Scattering plane is a plane

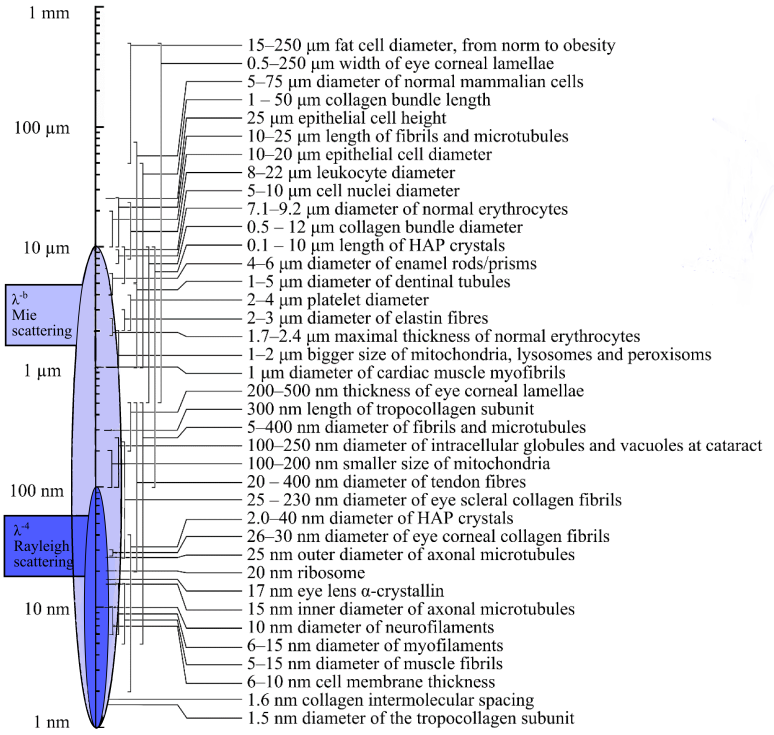


Fig. 3.7 Light scattering tissue and cell structures

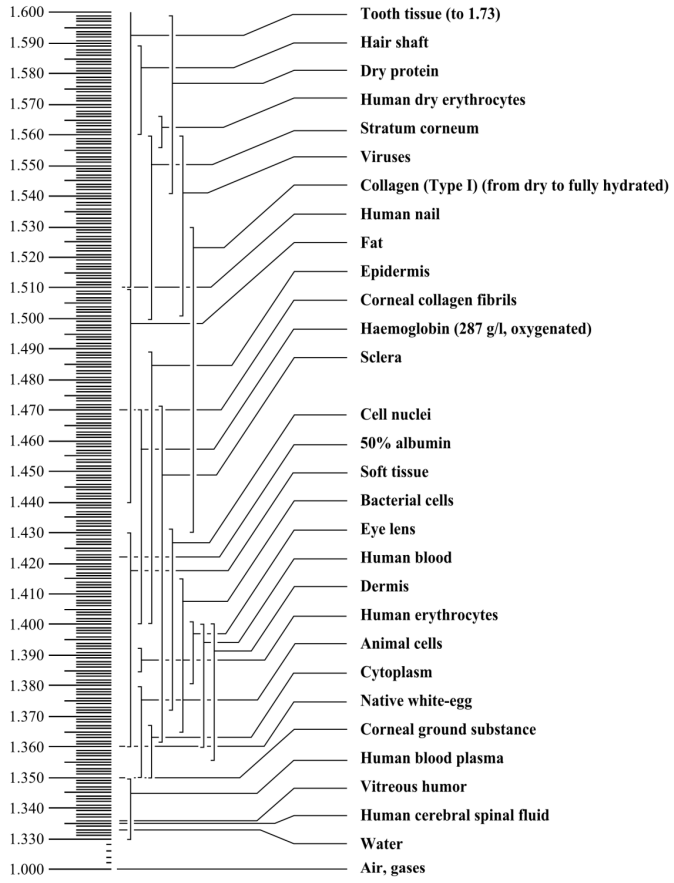


Fig. 3.8 Index of refraction of tissue and cell structures, the RI values depend on the wavelength which is sometimes in the range from UV to NIR, but mostly in the visible.

defined by positions of a light source, a scattering particle, and a detector.

To characterize scattering efficiency of a medium a scattering coefficient μ_s is introduced**,** in a nonabsorbing sample it is defined as the reciprocal of the distance d over which light of intensity $I(d=0)=I_0$ is attenuated (due to scattering) to $I(d)=\frac{I_0}{e}\approx 0.37 I_0$, which follows from the exponential law for light propagation in a tissue layer of thickness d (Fig.3.4)

$$I(d)=I_0\,exp(-\mu_s d), \tag{3.15}$$

where $I(d)$ is the intensity of transmitted light, W/cm^2; μ_s is typically expressed in cm^{-1}.

Behind this definition is also a fundamental process of photon scattering that is characterized by a photon scattering cross section, i.e., the ability of a particle to scatter a photon of a particular wavelength and polarization. Although the units are given as an area, it does not refer to an actual size area. Quantitatively, the number dN of photons scattered, between the points x and x + dx along the path of a light beam is the product of the number N of photons penetrating to depth x multiplied by the scattering cross section σ_{sca} (cm^2) and by the number of scattering particles per unit volume ρ_p (cm^{-3}) (Fig.3.4):

$$\frac{\mathrm{d}N}{\mathrm{d}x}=-\rho_p\sigma_{sca}N, \tag{3.16}$$

where

$$\mu_s=\rho_p\sigma_{sca}. \tag{3.17}$$

Equation (3.15) is valid if scattering is not strong and only the unscattered portion of transmitted light beam (so called ballistic photons) are detected. Such regime could be more or less realized for thin tissue layers when absorption is high enough to eliminate multiple scattering events. Therefore, a collimated (laser) beam is attenuated in a thin tissue layer of thickness d in accordance with the Bouguer–Beer–Lambert law

$$I(d)=(1-R_F)I_0\,exp(-\mu_t d), \tag{3.18}$$

where $I(d)$ is the intensity of transmitted light measured using a distant photodetector with a small aperture (on-line or collimated transmittance), W/cm^2; R_F is the coefficient of Fresnel reflection; at the normal beam incidence, $R_F=\frac{(m-1)^2}{(m+1)^2}$; m is the relative mean refractive index of tissue and surrounding medium of the incident half-space (see Eq. (3.7)); I_0 is the incident light intensity, W/cm^2;

$$\mu_t=\mu_a+\mu_s \tag{3.19}$$

is the interaction or total attenuation coefficient. The attenuation is a decrease in energy per unit area of a light beam which occurs as the distance from the source increases and is caused by absorption and scattering.

Often such characteristic of turbid materials and tissues as albedo for single scattering is useful for prediction of light propagation in a tissue. Albedo is the ratio of the scattering to extinction coefficient,

$$\Lambda=\frac{\mu_s}{\mu_t}. \tag{3.20}$$

It ranges from zero for a completely absorbing medium to unity for a completely scattering medium.

Besides scattering coefficient and albedo, scattering process is also characterized by a so called scattering phase function – the function that describes the scattering properties of the medium and is in fact the probability density function for a photon travelling in some direction to be scattered in some new direction $p(\theta, \varphi)$. Figure 3.9 illustrates geometry of the scattering of light by a particle, where the incident light beam ($\vec{s}_0$) is parallel to the z-axis and θ and φ are the scattering angles in the scattering plane and in the plane perpendicular to the scattering plane, respectively [22]. Scattering phase function characterizes an elementary scattering act. If scattering is symmetric relative to the direction of the incident wave, then the phase function depends only on the scattering angle θ (angle between two directions, new ($\vec{s}_1$) and former one ($\vec{s}_0$)), $p(\theta)$.

Scattering anisotropy factor, g, is a major parameter of $p(\theta)$ and is a measure of the amount of forward direction retained after a single scattering event [2-5, 10-23]. If a photon is scattered by a particle so that its trajectory is deflected by a scattering angle θ, then the component of the new trajectory which is aligned in the forward direction is presented as cosθ. There is an average scattering angle and the mean value of cosθ is defined as the anisotropy factor

$$g\equiv\langle cos\theta\rangle=\int_0^{\pi}p(\theta)cos\theta\cdot 2\pi sin\theta\,\mathrm{d}\theta. \tag{3.21}$$

The value of g varies in the range from –1 to 1: g = 0 corresponds to isotropic (Rayleigh) scattering, g = 1 to total forward scattering (Mie scattering by large particles), and –1 to total backward scattering. The assumption of random distribution of the scattering particles in a medium (i.e. the absence of a spatial correlation of tissue structures) leads to normalization

$$\int_0^{\pi} p(\theta) 2\pi \sin\theta \, d\theta = 1. \qquad (3.22)$$

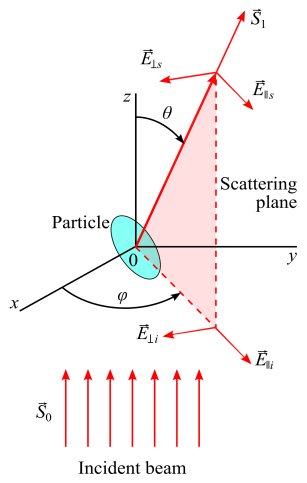


Fig. 3.9 Geometry of the scattering of light by a particle located at the origin 0. The polarized incident light beam ($\vec{s}_0$) is parallel to the *z*-axis [22]. Two orthogonal linear polarization components of the incident light field are presented as vectors $\vec{E}_{\parallel i}$ and $\vec{E}_{\perp i}$ in parallel and perpendicular to the scattering plane, respectively. θ and φ are the scattering angles in the scattering plane and in the plane perpendicular to the scattering plane, respectively. A detector is located at distance *r* from the origin along the vector $\vec{s}_1$, where two orthogonal polarization components $\vec{E}_{\parallel s}$ and $\vec{E}_{\perp s}$ of scattered light are coming.

3.2.3 Rayleigh scattering

If a particle is small with respect to the wavelength of the incident light, its scattering can be described as if it is a single dipole, the so called Rayleigh theory is applicable under the condition that $m(2\pi a/\lambda) << 1$, where *m* is the relative refractive index of the scatterers, $(2\pi a/\lambda)$ is the size parameter, *a* is the radius of the particle, and λ is the wavelength of the incident light in a medium [6-8, 22, 23]. For this theory, the scattered irradiance is inversely proportional to λ^4 and increases as a^6, the angular distribution of the scattered light is isotropic.

The angular dependence of the scattered intensity by an ensemble of *N* randomly distributed particles with mean distance between particles bigger than the wavelength λ, unpolarized incident light of intensity I_0, and distant detector position *r* is described by Rayleigh formula [6-8]

$$I(r,\theta) = (2\pi)^4 \frac{a^6}{\lambda^4 r^2} \left(\frac{m^2 - 1}{m^2 + 2} \right)^2 N \frac{1 + \cos^2\theta}{2} I_0, \qquad (3.23)$$

where $m = \frac{n_s}{n_0}$ is the relative index of refraction of scatterers and ground material, *N* is the number of particles in the scattering volume *V*, i.e., $N = \rho_p V$.

In general, light is polarized and presented as two orthogonal linear polarization components of the incident light field in parallel ($\vec{E}_{\parallel i}$) and perpendicular ($\vec{E}_{\perp i}$) to the scattering plane (see Fig. 3.9). Within the detector plane located at a distance *r* from the origin along the vector $\vec{s}_1$, two orthogonal polarization components $\vec{E}_{\parallel s}$ and $\vec{E}_{\perp s}$ of the scattered light create a specific polarization state depending on amplitudes and phase shift between components.

Figure 3.10 illustrates isotropy of Rayleigh scattering for unpolarized incident light and polarization insensitive detection (curve 3) and polarization ability of the scattering particles for the particular direction of detection (90° and 270°) where only light polarized perpendicular to the scattering plane is scattered (compare curves 1 and 2)). An ideal isotropy (circle-shaped phase function) of the scattering is achieved if incident light is linear polarized perpendicular to the scattering plane (curve 1).

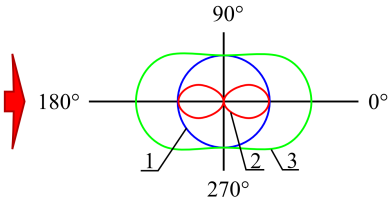


Fig. 3.10 Rayleigh scattering: light distribution in the scattering plane for two orthogonal linear polarization states and unpolarized incident light. 1 – Electric vector perpendicular to the scattering plane; 2 – electric vector parallel to the scattering plane; 3 – unpolarized light

For the NIR light and typical biological scatterers with *m* = 1.05–1.10, the maximum particle radius is about 12–14 nm for the Rayleigh theory to remain valid.

The Rayleigh–Gans or Rayleigh–Debye theory addresses the problem of calculating the scattering by a special class of arbitrary shaped particles, it requires $|m-1| << 1$ and $\frac{2\pi a'}{\lambda}|m-1| << 1$, where a' is the largest dimension of the particle [22-24]. These conditions mean that the electric field inside the particle must be close to that of the incident field and the particle can be viewed as a collection of independent dipoles that are all exposed to the same incident field. A biological cell might be modeled as a sphere of cytoplasm with a higher refractive index (n_c = 1.370) relative to that of the surrounding interstitial medium (n_i = 1.350), then *m* = 1.015 and for the NIR light this theory will be valid for the particle dimension up to a' = 850–950 nm. This approximation has been applied extensively to

calculations of light scattering from suspensions of bacteria [24]. It can be applicable for describing of light scattering from cell components (mitochondria, lysosomes, peroxisomes, etc) in tissues due to their small dimensions and refraction.

3.2.4 Mie scattering

Mie or Lorenz-Mie scattering theory relates to scattering by comparatively large spherical particles, which are of the order of the wavelength, and based on an exact solution of Maxwell's electromagnetic field equations for a homogeneous sphere [2-25]. Typically tissues contain both types of scatterers small and large (for instance, cell components and collagen fibers of connective tissues, see Fig.3.7). Mie theory operates with the following relevant particle parameters: radius a and complex refractive indices of its material $n_s(\lambda_0)$ and dielectric host (ground material) $n_0(\lambda_0)$

$$n_{s,0}(\lambda_0) = n'_{s,0}(\lambda_0) + in''_{s,0}(\lambda_0), \tag{3.24}$$

where λ_0 is the wavelength in a vacuum. The imaginary part of the complex refractive index of material is responsible for light losses due to absorption. Mie theory yields the scattering ($Q_{sca} = \frac{\sigma_{sca}}{\pi a^2}$) and absorption ($Q_{abs} = \frac{\sigma_{abs}}{\pi a^2}$) efficiencies and the phase function from which the absorption and scattering cross sections (σ_{sca} and σ_{abs}) and the scattering anisotropy factor g are calculated:

$$\sigma_{sca}^{Mie} = \frac{\lambda_0^2}{2\pi n_0^2}\sum_{n=1}^{\infty}(2n+1)\left(|a_n|^2 + |b_n|^2\right), \tag{3.25}$$

$$\sigma_{abs}^{Mie} = \\ = \frac{\lambda_0^2}{2\pi n_0^2}\sum_{n=1}^{\infty}(2n+1)\left[Re(a_n + b_n) - \left(|a_n|^2 + |b_n|^2\right)\right] \tag{3.26}$$

$$p^{Mie}(\theta) = \frac{\lambda_0^2}{2\pi n_0^2 \sigma_{sca}^{Mie}}\left(|S_1|^2 + |S_2|^2\right), \tag{3.27}$$

where a_n and b_n are Mie coefficients, which are functions of the relative complex refractive index of particles (m) and parameter $\alpha = \frac{2\pi a n_0}{\lambda_0}$; an asterisk indicates that the complex conjugate is to be taken;

$$a_n = \frac{\psi_n(\alpha)\psi'_n(m\alpha) - m\psi_n(m\alpha)\psi'_n(\alpha)}{\zeta(\alpha)\psi'_n(m\alpha) - m\psi_n(m\alpha)\zeta'_n(\alpha)}, \\ b_n = \frac{m\psi'(m\alpha)\psi_n(\alpha) - \psi_n(m\alpha)\psi'_n(\alpha)}{m\psi'_n(m\alpha)\zeta_n(\alpha) - \psi_n(m\alpha)\zeta'_n(\alpha)}, \tag{3.28}$$

ψ_n and ζ_n are the Riccati–Bessel functions; S_1 and S_2 are functions of the polar scattering angle and can be obtained from the Mie theory as

$$S_1(\theta) = \sum_{n=1}^{\infty}\frac{2n+1}{n(n+1)}\left\{a_n\pi_n(cos\theta) + b_n\tau_n(cos\theta)\right\}, \\ S_2(\theta) = \sum_{n=1}^{\infty}\frac{2n+1}{n(n+1)}\left\{b_n\pi_n(cos\theta) + a_n\tau_n(cos\theta)\right\}, \tag{3.29}$$

the parameters π_n and τ_n represent

$$\pi_n(cos\theta) = \frac{1}{sin\theta}P_n^1(cos\theta), \\ \tau_n(cos\theta) = \frac{d}{d\theta}P_n^1(cos\theta), \tag{3.30}$$

where $P_n^1(cos\theta)$ is the associated Legendre polynomial; the following recursive relationships are used to calculate π_n and τ_n:

$$\pi_n = \frac{2n-1}{n-1}\pi_{n-1}cos\theta - \frac{n}{n-1}\pi_{n-2}, \\ \tau_n = n\pi_n cos\theta - (n+1)\pi_{n-1}, \tag{3.31}$$

and the initial values are:

$$\begin{cases}\pi_1 = 1, \pi_2 = cos\theta, \\ \tau_1 = cos\theta, \tau_2 = 3cos2\theta.\end{cases} \tag{3.32}$$

Accounting for definition expressed by Eq. (3.21) scattering anisotropy factor can be calculated from Eq. (3.27)

$$g^{Mie} = \frac{\lambda_0^2}{\pi n_0^2 \sigma_{sca}^{Mie}}\left\{\begin{array}{l}\sum_{n=1}^{\infty}\frac{2n+1}{n(n+1)}Re\left(a_n b_n^*\right) + \\ +\sum_{n=1}^{\infty}\frac{n(n+2)}{n+1}Re\left(a_n a_{n+1}^* + b_n b_{n+1}^*\right)\end{array}\right\}. \tag{3.33}$$

Similarly to the Rayleigh formula (3.23), the angular dependence of the scattered light intensity by an ensemble of N randomly distributed Mie particles with mean distance between particles bigger than the wavelength λ, for unpolarized incident light of intensity I_0 and distant detector position r, is described by

$$I(\theta) = p^{Mie}(\theta)\cdot N \cdot I_0 . \tag{3.34}$$

The introduction of the specific scattering and absorption coefficients extrapolated to a volume fraction $f = 1$ is useful for describing scattering and absorption properties of an ensemble of Mie scattering particles. In that case and when the particles are sufficiently distant to prevent dependent scattering, the scattering

coefficient is proportional to the dimensionless volume fraction of scatterers *f*. From Eq. (3.17) it follows:

$$\mu_s = \rho_p \sigma_{sca} = (f/V)\sigma_{sca} = f\bar{\sigma}_{sca}, \qquad (3.35)$$

where the specific scattering coefficient $\bar{\sigma}_{sca} = \sigma_{sca}/V$ is expressed in cm^{-1}, V is the unit volume.

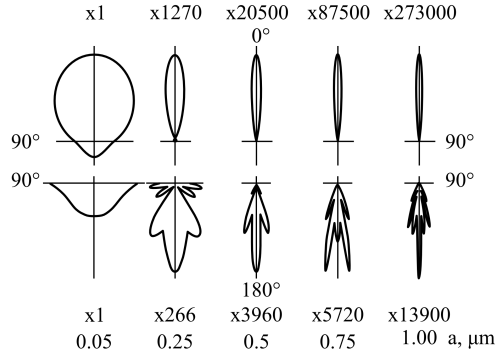


Fig. 3.11 The polar diagrams of the calculated angular-dependent intensity distributions (Mie phase functions) for 5 single isotropic spheres with the diameter in the range of those which are typical for cell organelles, from 0.05 to 1.00 μm [25].

Mie theory predicts that scattering introduced by spherical micrometer-sized particles is strongest if the particle radius and wavelength are of the same order of magnitude (Figs. 3.11 and 3.12). The scattering coefficient increases strongly with the elevation of the relative index of refraction. In contrast, for the matched refractive indices of scatterers and background material, the scattering coefficient goes to zero, which means that only absorption is responsible now for the light beam extinction [see Eq. (3.18)]. However, because of very low absorption of many tissues in the NIR range, refractive index matching conditions due to perfusion of endogenous or exogenous immersion agents may have a significant influence on tissue optical properties. It is also of great importance that scattering anisotropy factor aspires to 1 (extremely high scattering directness).

In Fig. 3.12, the wavelength dependencies of scattering parameters are also shown. If particle diameter $2a$ and relative index m are fixed, the wavelength dependencies are caused by variation of the ratio of particle diameter and wavelength only. The spectral variation of the relative index m has been neglected in these calculations, but may be relevant in practice.

For example, epithelial cell nucleus can be considered as a spherical Mie scatter with refractive index, n_{nc}, which is higher than that of the surrounding cytoplasm, n_{cp}, i.e., $m = n_{nc}/n_{cp}$. Normal nuclei have a characteristic diameter $2a$ = 4–7 μm. In contrast, dysplastic nuclei can be as large as 20 μm, occupying almost the entire cell volume. In the visible and NIR range, where the wavelength $\lambda << 2a$, Mie theory can be well approximated by the Van de Hulst approximation or also called anomalous diffraction approximation, which is applicable for optically soft particles [$(m - 1) << 1$] [26]. Thus, the elastic scattering cross section of the cell nuclei can be described as

$$\sigma_{sca}(\lambda, a) = 2\pi a^2 \left(1 - \frac{2\sin\delta}{\delta} + \left(\frac{2\sin\delta}{\delta}\right)^2\right), \qquad (3.36)$$

where $\delta = \frac{4\pi a(m-1)}{\lambda_0}$, λ_0 is the wavelength of the light in free space. The cross section varies periodically with inverse wavelength and gives rise to a periodic component in the tissue optical reflectance. Since the frequency of this variation (in inverse wavelength space) is proportional to particle size, the nuclear size distribution can be obtained from the Fourier transform of the periodic component.

Mie theory is strictly applicable only to particles of particular regular shapes, but results are still useful if the shape is irregular. The oscillatory structure of the scattering coefficient and anisotropy factor as a function of particle size, which is observed with spherical particles (see Figs. 3.12a,b), will be averaged out in the case of irregular shape.

Actual biological tissue models are more complex than a monodispersive system of distant spherical particles or even randomly shaped ones. Sometimes, a mixture of large particles contributing high scattering anisotropy and small particles with increased scattering towards shorter wavelengths may be a good approximation to describe tissue scattering properties.

Besides theoretical Mie phase function [see Eq. (3.27)], several semi-empirical approximations for the scattering phase function have been used in tissue photonics [2-5, 18, 28]. One of the most often exploited is the Henyey-Greenstein (HG) phase function

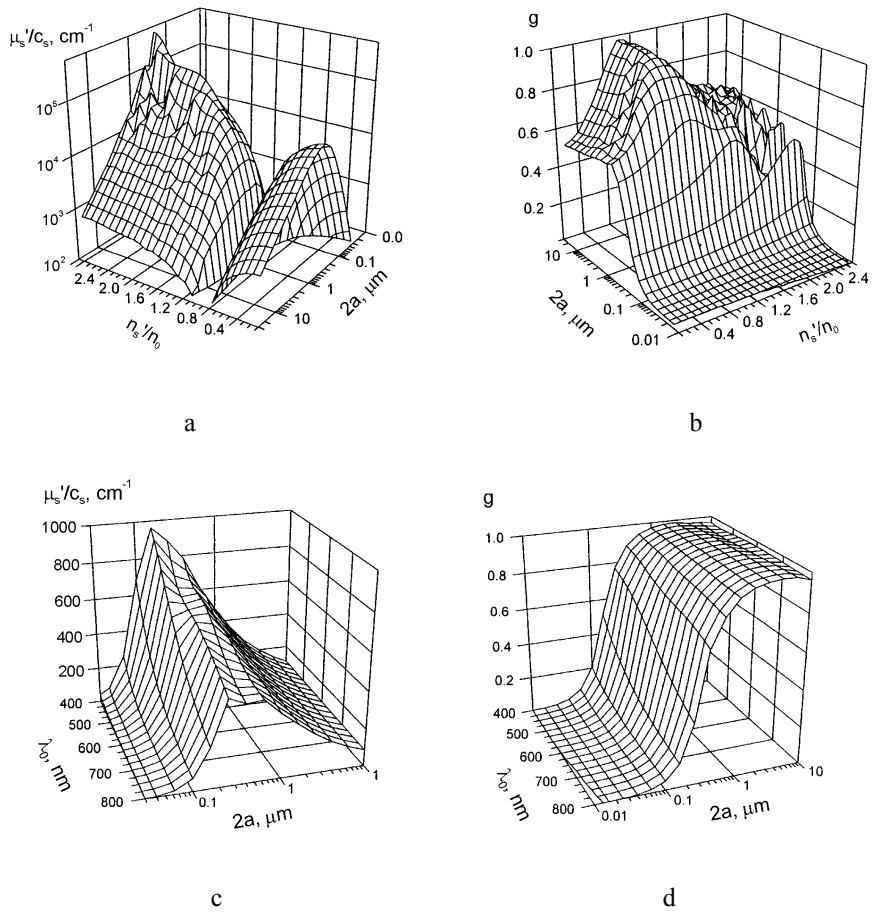
$$p^{HG}(\theta) = \frac{1}{4\pi} \cdot \frac{1 - g^2}{(1 + g^2 - 2g\cos\theta)^{3/2}}. \qquad (3.37)$$

The HG phase function has one parameter g that may be represented as the infinite series of Legendre polynomials $P_n^1(\cos\theta)$,

$$p^{HG}(\theta) = \frac{1}{4\pi} \sum_{n=0}^{\infty} (2n+1) f_n P_n^1(\cos\theta), \qquad (3.38)$$

where $f_n = g^n$ is the n^{th} order moment of the phase function.

Figure 3.13 illustrates behavior of the Henyey-Greenstein scattering phase function calculated for g values characteristic for hard (0.6–0.9) and soft (0.8–0.95) tissues, as well as for highly anisotropic scattering systems such as blood (0.995).



Fig, 3.12 Mie theory: the scattering properties [normalized reduced scattering coefficient $\mu_s'/C_s = (\mu_s/C_s)(1-g)$ (a) and scattering anisotropy factor g(b)] of an ensemble of noninteracting nonabsorbing spherical particles calculated at 633 nm for the broad ranges of diameter ($2a$) and relative index of refraction ($m=n_s'/n_0$) which are characteristic to tissue and cellular structure components; wavelength-diameter dependences of $\mu_s'(\lambda_0, 2a)/C_s$ (c) and $g(\lambda_0, 2a)$ (d) at relative index of refraction m = 1.07, typical for normal soft tissues; C_s is the volume fraction of the particles [5, 27].

3.2.5 Multiple scattering

Parameters introduced are related to light tissue interaction on the level of a single scattering that occurs when a wave undertakes no more than one collision with particles of the medium in which it propagates. For example, this is a case for healthy transparent front human eye tissues, such as cornea, eye lens and vitreous body (see Fig. 2.6) [1], or for a tissue slice which is sufficiently thin that single scattering approximation accurately estimates the reflection and transmission of the slab. In contrast, in many real situations, especially in *in vivo* studies of skin, breast, brain and etc., a multiple scattering – a scattering process, in which on average each photon undertakes many scattering events, is more likely [2-5, 9-38].

To evaluate what kind of scattering regime is realized a so called mean free path length (MFP) may be introduced. MFP is the mean distance between two successive interactions with scattering or absorption which a photon travelling in a scattering-absorption medium experiencing,

$$\mathrm{MFP} = l_{ph} = 1/\mu_t. \qquad (3.39)$$

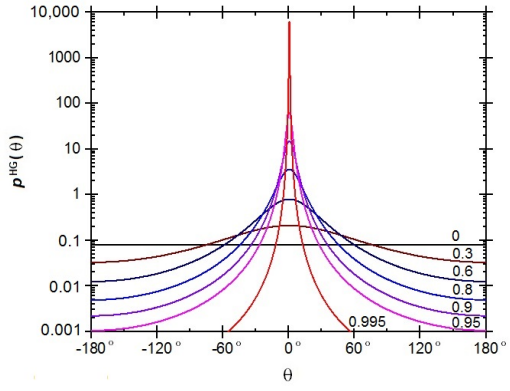


Fig. 3.13 The Henyey-Greenstein (HG) scattering phase function often used in tissue photonics; it is calculated for typical g values characteristic for hard (0.6-0.9) and soft (0.8-0.95) tissues and blood (0.995).

Thus, one can differentiate optically thin (transparent) or optically thick sample is under investigation. "Optical thickness" is the depth of a material or medium in which the intensity of light of a given wavelength is reduced by a factor of 1/e because of absorption and/or scattering [see Eq. (3.18)]. A sample of high physical thickness and/or high turbidity that correspond to a few "optical thicknesses" is optically thick, as well as a sample with a low thickness and/or low turbidity that correspond to one or less than one "optical thickness" is optically thin.

The radiation transfer theory (RTT) is the basic theory allowing one to calculate light distributions in the multiple scattering media with absorption, such as tissues. The heart of this theory is the radiation transfer equation (RTE) – the Boltzmann or linear transport equation, which is a balance equation describing the flow of particles (e.g., photons) in a given volume element that takes into account their velocity *c*, location *r*, and changes due to collisions (i.e., scattering and absorption). The basic parameter for this theory is the reduced scattering coefficient that is incorporating the scattering coefficient μ_s and the scattering anisotropy factor *g* as the following expression

$$\mu'_s = \mu_s(1-g), \tag{3.40}$$

or at usage of dimensionless volume fraction of scatterers *f* and the specific scattering coefficients $\bar{\sigma}_{sca}$ [see Eq. (3.35)] as

$$\mu'_s = f\bar{\sigma}_{sca}\left[1-g(\lambda_0,2a)\right]. \tag{3.41}$$

The transport mean free path (TMFP) of a photon (cm) is defined as

$$l_{tr} = \frac{1}{\mu_a+\mu'_s}, \tag{3.42}$$

where $\mu_a+\mu'_s=\mu_{tr}$ is the photon transport coefficient. The TMFP in a medium with anisotropic single scattering significantly exceeds the MFP, $l_{tr}>>l_{ph}$. The l_{tr} is the distance over which the photon loses its initial direction.

In tissues, at visible and NIR light propagation, reduced scattering coefficient μ_s' mostly defines light transport, because absorption much lower than scattering, $\mu_s' >> \mu_a$,

$$l_{tr} \cong \frac{1}{\mu'_s}. \tag{3.43}$$

The reduced scattering coefficient μ_s' describes the diffusion of photons in a random walk of step size of $\frac{1}{\mu'_s}$ [cm], where each step involves isotropic scattering. Schematically scattering processes are presented in Fig. 3.14 [20]. This is equivalent to description of photon movement using many small steps $\frac{1}{\mu_s}$ that each involve only a partial (anisotropic) deflection angle if there are many scattering events before an absorption event, i.e., $\mu_s' >> \mu_a$ (diffusion regime). Parameter μ_s' is useful in the diffusion regime. Figure 3.14 shows the equivalence of taking 10 smaller steps of MFP $\cong\frac{1}{\mu_s}$ with anisotropic deflection angles and one big step with a TMFP $\cong\frac{1}{\mu'_s}$. Diffusion regime is well described analytically in the framework of diffusion approximation of the radiation transfer equation – diffusion theory.

A power law for dependence of the reduced scattering coefficient on the wavelength is typical for many tissues, $\mu'_s(\lambda)=\mu'_s(\lambda_{ref})(\lambda/\lambda_{ref})^{-b}$. In Refs. [18, 20, 21], $\lambda_{ref}=500nm$. For different tissues and tissue conditions (normal or pathological, coagulated or dehydrated, etc.) parameter *b* is ranging from 0.5 to 1.6 for the visible-NIR light scattering (600–2000 nm).

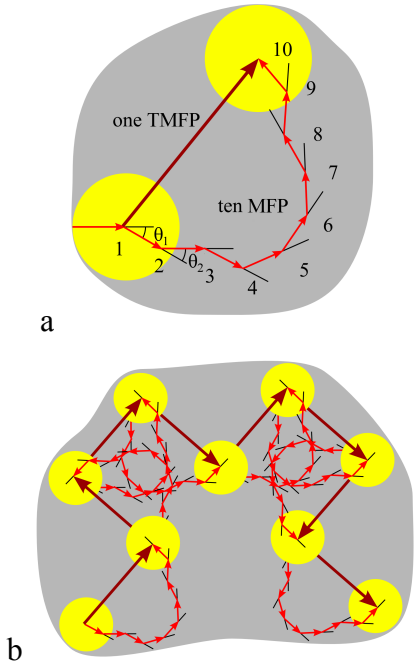


Fig. 3.14 Multiple scattering: mean free path (MFP) and transport MFP (TMFP) definitions; MFP ≅ $1/\mu_s$ ($\mu_s >> \mu_a$), TMFP≅ $1/\mu_s'$ ($\mu_s' >> \mu_a$), and $\langle\cos\theta\rangle$ = 0.90, i.e., $\langle\theta\rangle \approx \theta_1 \approx \theta_2 \approx \ldots \approx \theta_{10} \approx 26°$ and $\mu_s' = \mu_s(1-g) = 0.10\mu_s$ (a); illustration of photon random walk of TMFP-step size; scattering particles are shown as yellowish disks, small arrows show direction of photon migration between consecutive elementary interaction acts with

scattering; big arrows show direction of effective photon migration as a result of multiple scattering; for more anisotropic phase function (bigger *g*-factor) more elementary scattering steps needed to transfer photon distribution to isotropic one (b); http://omlc.ogi.edu/classroom/ece532/class3/musp.html.

For example, for tissue model of noninteracting Mie scatterers of equal diameter $2a$, for typical parameters of soft tissues ($g > 0.9$; $5 < 2\pi a/\lambda < 50$; $1 < m < 1.1$) the reduced scattering coefficient is described by a simple expression [34]

$$\mu'_s = 3.28\pi a^2 \rho_p \left(\frac{2\pi a}{\lambda}\right)^{0.37} \times (m-1)^{2.09}. \qquad (3.44)$$

Attenuation of a wide (expanded) laser beam of intensity I_0 in a thick tissue at depths $z > l_d = \frac{1}{\mu_{eff}}$, where diffusion regime takes place, is described as [5]

$$I(z) \approx I_0 b_s \exp(-\mu_{eff} z), \qquad (3.45)$$

where $\mu_{eff} = \sqrt{3\mu_a(\mu'_s + \mu_a)}$, which follows from the diffusion theory; b_s accounts for additional irradiation of the upper layers of a tissue due to backscattering (photon redistribution or recycling effect). Respectively, the depth of light penetration into a tissue is

$$l_e = l_d[\ln b_s + 1]. \qquad (3.46)$$

Typically, for soft tissues b_s =1–5 for beam diameter of 1–20 mm. Thus, when wide laser beams are used for irradiation highly scattering tissues with low absorption, CW light energy is accumulated in tissue due to high multiplicity of random long-path photon migrations. A highly scattering medium works as an optical cavity with random reflectors (scatterers) providing the capacity of light energy. The light power density within the superficial tissue layers may substantially (up to fivefold) exceed the incident power density and cause the over dosage during photodynamic therapy or overheating at interstitial laser thermotherapy. On the other hand, photon recycling effect can be used for more effective irradiation of under surface lesions at relatively small incident power densities.

To describe pulsed light propagation, which is often used in tissue spectroscopy and imaging, in a tissue the time-dependent radiation transfer theory should be used [2-5, 35-38]. This theory is based on the time-dependent linear transport equation, which is a balance equation describing the time-dependent flow of particles (e.g., photons) in a given volume element that takes into account their velocity c, location $\bar{r}$, and changes due to collisions (i.e., scattering and absorption).

The time-resolved methods that use pulsed or intensity modulated laser beams for irradiating of tissues under study can separate different components of scattering photons from a sample in forward (transillumination) or backscattering operating modes. One of these groups of photons is a so called ballistic (coherent) photon group which is consists of unscattered and strictly straightforward scattered photons. The other group is composed of quasi-ballistic (snake or zigzag) photons which are photons that migrate within a scattering medium along trajectories that are close but not the same as for ballistic photons. To the third group the so called diffusion photons belong. This is typically the largest group of photons that migrated for longer time in a tissue along multi-step random trajectories. Each of these groups carries information about optical (morphological) properties of a tissue. Ballistic photons are good for getting precise tissue images similar to x-ray computer tomography however in many tissues because of strong scattering this group of photon is typically negligibly small. The snake photons, having undergone only a few scattering events, all of which are in the forward or near-forward direction, retain the image bearing characteristics to some extent, however their amount is rather big in comparison with the ballistic photons, thus they are detectable and provide good spatial resolution. In contrast, due to high intensity of diffusion component there is much more practical to use diffusion photons to estimate optical properties of tissues however a spatial resolution could not be very high.

Figure 3.15 illustrates short pulse propagation in tissues, where an ultrashort laser pulse incident on tissue surface spreads in bulk into three main groups of photons – first arriving to detector (ballistic), more intensive group of snake photons, and a large group of diffuse late arriving photons with a broad distribution. Figure 3.15b demonstrates how decays the amplitude of intensity modulated light at frequency $\omega=2\pi\nu$ propagating through a scattering tissue and how shifts its modulation phase, $\Delta\Phi$. For a weakly absorbing scattering medium, when $\mu_a << \frac{\omega}{c}$ and $<< \mu'_s$, an alternating component of the scattered light is a outgoing spherical intensity (or photon density) wave with the center at the point $\bar{r} = 0$ which oscillates at a modulation frequency ω with the modulation depth [5]

$$m_U(\bar{r},\omega) = m_I \cdot \exp\left(\bar{r}\sqrt{\frac{\mu_a}{D}}\right) \cdot \exp\left(-\bar{r}\sqrt{\frac{\omega}{2cD}}\right), \qquad (3.47)$$

and undergoes a phase shift relative to the phase value at point $\bar{r} = 0$ equal to

$$\Delta\Phi(\bar{r},\omega) \cong \bar{r}\sqrt{\frac{\omega}{2cD}}, \qquad (3.48)$$

where $m_I = \dfrac{\delta I}{I_0}$ is the modulation depth of the incident light with mean intensity I_0 and alternating amplitude δI;

$$D = \frac{1}{3\left(\mu_s' + \mu_a\right)} \cong \frac{1}{3\mu_s'} \tag{3.49}$$

is the photon diffusion coefficient, c^{-1}. Accounting for Eq. (3.49) expressions (3.47) and (3.48) could be further simplified

$$m_U\left(\bar{r},\omega\right) = \\ = m_I \cdot \exp\left(\bar{r}\sqrt{3\mu_a\mu_s'}\right) \cdot \exp\left(-\bar{r}\sqrt{\frac{3\omega\mu_s'}{2c}}\right), \tag{3.50}$$

$$\Delta\Phi\left(\bar{r},\omega\right) \cong \bar{r}\sqrt{\frac{3\omega\mu_s'}{2c}}\ . \tag{3.51}$$

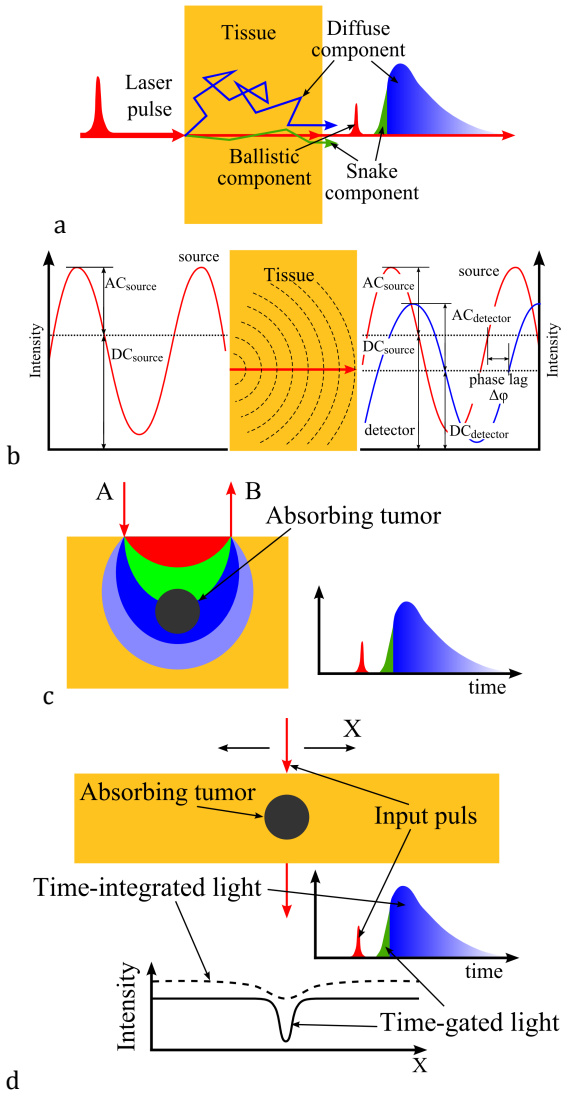


Fig. 3.15 Short pulse and intensity modulated light propagation in tissues: (a) an ultrashort laser pulse spreads into three main groups of photons – ballistic (first arriving to detector), snake, and diffuse (broad distribution of late arriving photons); (b) illustration of intensity modulation amplitude decay and phase shift due to scattering; (c) illustration of two typical geometries for optical imaging of absorbing inhomogeneity (tumor) in tissues, A – probing beam (typically delivered by a fiber), B – detected radiation (typically collected by a detector fiber), left – transillumination mode, right – backscattering mode; (d) illustration of absorbing inhomogeneity (tumor) image contrast enhancement due to time-gating by selecting early arriving (snake) photons only, X is the light beam scanning axis [35].

To generate and support a photon density wave a light scattering medium is needed. However, high scattering turns a photon density wave to decay with distance (see Eq. (3.50)). Measuring $m_U\left(\bar{r},\omega\right)$ and/or $\Delta\Phi\left(\bar{r},\omega\right)$ allows one to determine separately the reduced scattering coefficient μ_s' and the absorption coefficient μ_a, and evaluate the spatial distributions of these parameters needed for imaging of tissue pathologies. For biomedical applications, in particular, optical mammography or brain imaging, typical modulation frequencies are lying in the range $\omega/2\pi$ = 50–1000 MHz [2-5, 35-38].

Two typical geometries (transillumination and backscattering) for a time-resolved optical imaging of absorbing inhomogeneity (tumor) in tissues are shown (see Fig. 3.15c). Figure 3.15d illustrates image contrast (spatial resolution) enhancement due to time-gating by selecting early arriving (snake) photons at pulse excitation.

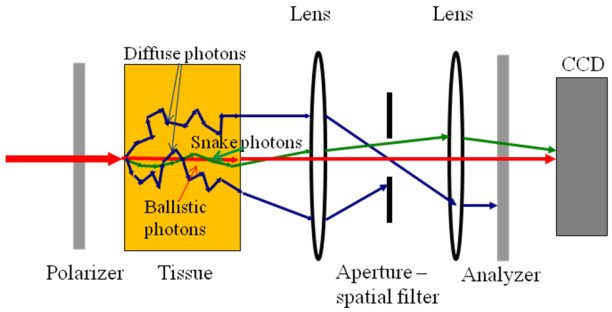


Fig. 3.16 Schematic representation of spatial filtering using an aperture in the detector space and polarization gating with a linear polarizer in the light incidence space and in-line polarized analyzer in the detector space; diffuse photons are not detected due to their high deflection angles (spatial filtering) or due to loosing initial polarization state because of long travelling paths.

To improve spatial resolution of diffusion methods various approaches for selective detection of informative photons were suggested, such as spatially-

resolved, angular-resolve, and polarization-sensitive gating. Spatial filtering and polarization gating approaches are shown schematically in Fig. 3.16. It is well seen that diffuse photons are not detectable due to their high deflection angles (spatial filtering) or due to loosing initial polarization state because of long travelling paths within tissue. Thus more contrast image could be produced by detection pure ballistic and least-scattering (snake) photons which have minimal deflection and alternation of polarization state.

The most complete information about tissue optical properties could be obtained when spectrum of the scattered light is measured in the wavelength range of interest. This spectrum may be differential, measured or calculated for a certain scattering angle, or integrated within an angle (field of view) of the measuring spectrometer. In general, it includes transmitted and backscattered (back reflected) light within a narrow field of view, such as measured in geometry of collimated transmittance or specular reflectance, or totally forward or backward scattered light measured using integrating sphere technique. Figure 3.17 illustrates typical spectral measurement geometries used for *in vitro* and *in vivo* studies [2-5, 17, 18]. *In vitro* measurements include angular spectral dependences $I(\theta, \lambda)$ using goniometric detection with the narrow slit in front of a detector, and angular integrated spectra by integrating sphere. Angular measurements $[I(\theta, \lambda)]$ are used for evaluation of phase scattering function $p(\theta, \lambda)$ [see Eqs. (3.27) and (3.37)] for the particular wavelength. Sometimes backward $[I_b(\theta,\lambda)]$ and forward $[I_f(\theta,\lambda))$ scattering intensities, or collimated transmitted $[I_c(\lambda)]$ and specular (Fresnel) reflected $[I_F(\lambda)]$ intensities are measured to characterize tissue sample optical properties. The collimated transmittance and specular (Fresnel) reflectance spectra are introduced as

$$T_c(\lambda) = \frac{I_c(\lambda)}{I_0(\lambda)}, \tag{3.52}$$

$$R_F(\lambda) = \frac{I_F(\lambda)}{I_0(\lambda)}. \tag{3.53}$$

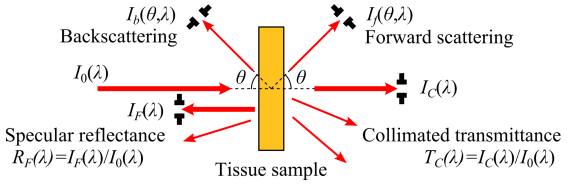
The total transmittance $[T_t(\lambda)]$, and diffuse reflectance $[R_d(\lambda)]$ spectra measured with the help of integrating spheres are introduced as

$$T_t(\lambda) = \frac{I_t(\lambda)}{I_0(\lambda)} = T_c(\lambda) + T_d(\lambda), \tag{3.54}$$

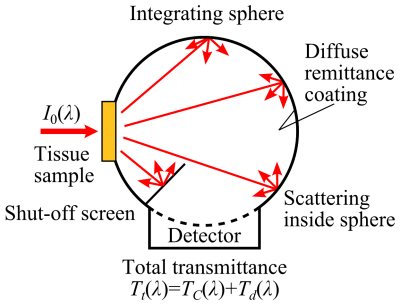
$$I_t(\lambda) = I_c(\lambda) + \int_{-\frac{\pi}{2}}^{\frac{\pi}{2}} I_f(\theta,\lambda)\,d\theta; \tag{3.55}$$

$$R_d(\lambda) = \frac{I_b(\lambda)}{I_0(\lambda)}, \tag{3.56}$$

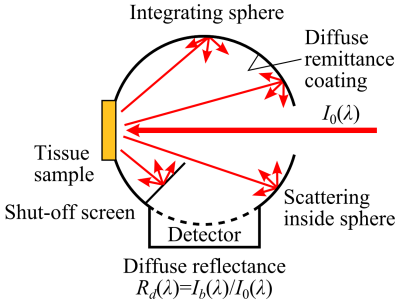
$$I_b(\lambda) = \int_{\frac{\pi}{2}}^{-\frac{\pi}{2}} I_b(\theta,\lambda)\,d\theta. \tag{3.57}$$



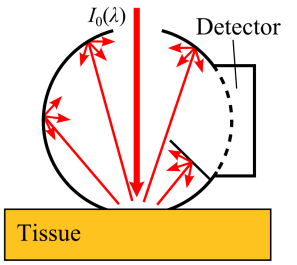
a



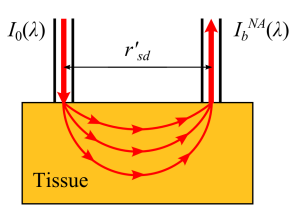
b



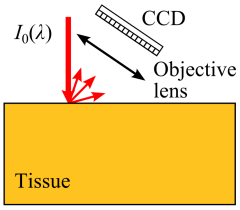
c



d



e



f

Fig. 3.17 Typical geometries used for *in vitro* and *in vivo* spectral measurements: *in vitro* goniometric detection with the narrow slit in front of a detector $I(\theta, \lambda)$ (phase scattering function $p(\theta, \lambda)$ measurements) and fixed angle detection (collimated transmittance $T_c(\lambda)$ ($\theta = 0$) and specular reflectance $R_F(\lambda)$ ($\theta = 2\pi$)(a); *in vitro* angular integrated detection using an integrating sphere: the total transmittance $T_t(\lambda)$ (b) and diffuse reflectance $R_d(\lambda)$ (c); *in vivo* integrating sphere detection (d), spatially-resolved fiber (e) or CCD (f); the integrating surface of the sphere is coated with non-fluorescing material ($BaSO_4$, or MgO, or Spectrolan®), which have nearly 100% diffuse remittance over the entire optical and NIR spectrum of interest; shut-off screen prevents direct irradiation of the detector; the intensity of light entered into a sphere is measured as the signal of the detector multiplied by the ratio of areas of the entire sphere and detector surfaces; the accuracy of such measurements evidently depends on this ratio.

In vivo studies could be done in different ways, but the most typical geometries are the spatially-resolved backreflectance using two fibers with numerical aperture *NA* – one as a light source [$I_0(\lambda)$] and another as a detector [$I_b^{NA}(\lambda)$] with variable source-detector separation r_{sd} (Fig. 3.17d), or using CCD (CMOS) camera with objective lens (Fig. 3.17e). Integrating sphere measurements of diffuse reflectance are also often provided (Fig. 3.17d).

The modeling of light propagation in a tissue by taking into account the experimental geometry, light source and detector characteristics, known optical properties of a sample, and predicted measurement and associated accuracies is often need for planning of strategy of light treatment or diagnosis. Such modeling and predictions are classified as a solution of the *forward scattering problem*. In contrast, the *inverse scattering problem* solution is the attempt to take a set of measurements and error estimates, and only a limited set of parameters describing the sample and experimental specificity, and to derive the remaining parameters. Usually the geometry is known, intensities or their parameters are measured, and the optical properties or sizes and refractive indices of tissue scatterers need to be derived. If these properties are considered to be spatially varying, then the resultant solutions can be presented as a 2D or 3D function of space, i.e., as an image.

3.3 Scattering of the coherent light – speckles

3.3.1 Random phase screen concept and speckle formation

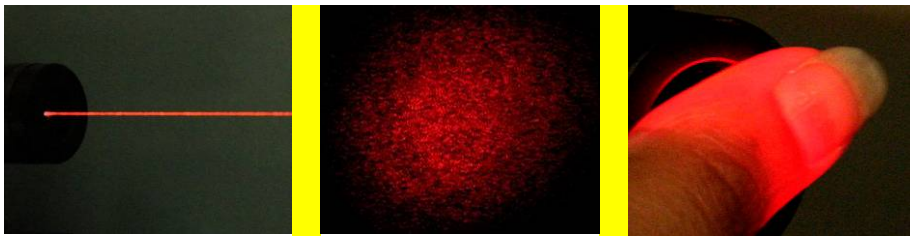
When coherent (laser) light is reflected from a rough surface or passes through a bulk scattering medium, speckle patterns are produced as a result of interference of a large number of elementary waves (wavelets) with random phases that arise due to light interaction with random scatterers [5, 9, 39-61]. Figure 3.18 illustrates this for a He-Ne laser beam reflection by a rough surface, where complex interference of the scattered coherent wavelets appears as an interference pattern with the spatially resolved intensity spots. In contrast, at laser beam transportation through a bulk tissue (human finger) due to multiple scattering beam is transformed to diffuse radiation, speckle size became comparable with the wavelength and could not be seen by a naked eye. This situation is often considered as a total loosing of light coherence. However at multiple scattering coherent properties of light also could be detected and used for tissue functional diagnostics. A single-mode fiber having a core diameter comparable with the wavelength allows for detection a single or a small group of neighboring speckles in the pattern. Speckle temporal dynamics gives information about intensity fluctuations connected with Brownian motion of biological molecules or flow of the blood particles. This is the basis for diffusion wave spectroscopy (DWS) or diffusion wave imaging (DWI) [5, 52, 53, 61].

Generally, there are two types of speckles: subjective speckles, which are produced in the image space of an optical system (including an eye), and objective speckles, which are formed in a free space and are usually observed on a screen (CCD) placed at a certain distance from an object. Since the majority of tissues are optically non-uniform, their irradiation with a coherent light always gives rise to the appearance of speckle patterns, which either distort the results of measurements and, therefore, should be eliminated by statistical averaging, or provide a new information about the structure and the motion of a tissue and its constituents [5, 48]. The average size of a speckle in the far–field zone is estimated as

$$d_{av} \approx \frac{\lambda}{\varphi}, \qquad (3.58)$$

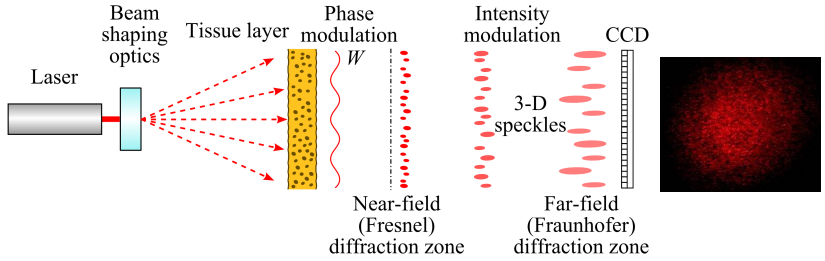
where λ is the wavelength and φ is the angle of observation.

Figure 3.19 schematically illustrates the principles of the formation and propagation of speckles, shows transmittance and reflectance modes of their observation as a spatial (x) or temporal (t) intensity modulation in the detector's plane (CCD). The incident coherent light at interaction with a random (scattering) medium is

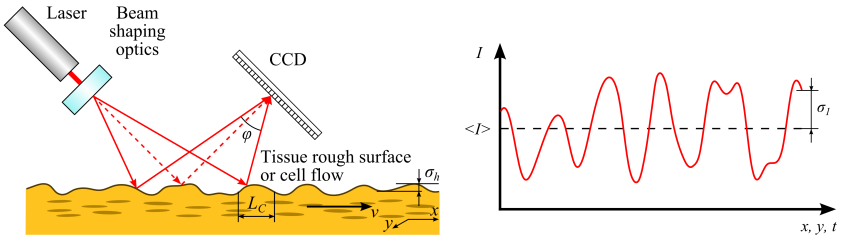


a b c

Fig. 3.18 Coherent light interaction with inhomogeneous media: (a) Helium-Neon laser (λ=632.8 nm) beam as it travelling in a free space (open air), no interaction, therefore no additional divergence, beam diameter is of ~ 1 mm; (b) the speckle structure (pattern) formed at laser beam reflection from a rough surface – illustrates coherent properties of light in the form of complex interference of the scattered coherent wavelets; (c) at laser beam transportation through a bulk tissue (human finger) due to multiple scattering it is transformed to diffuse radiation, speckle size became comparable with the wavelength and could not be seen by a naked eye. Sometimes it is saying that coherent light has lost its coherence. However in many experiments coherent properties of incident light could be seen and used even at multiple scattering. For example, at detection with the help of a single-mode fiber a single or small group of neighboring speckles can be selected, dynamics of which give information about intensity fluctuations connected with Brownian motion of biological molecules or flow of blood particles. This is the basis of diffusion wave spectroscopy (DWS). These photos are done by Joel Mobley.



a



b c

Fig. 3.19 Formation and propagation of speckles: observation of speckles in transmittance mode (a); observation of speckles in reflectance mode (b), and spatial (x, y) or temporal (t) intensity modulation in the detector's plane (CCD) (c).

firstly phase modulated with the appearance of the wavelets (W) due to diffraction phenomenon, this modulation is further transformed to intensity modulation as light propagates through near-field (Fresnel) zone to far-field (Fraunhofer) zone of diffraction, where typically speckles are detected. Spatial intensity modulation of the scattered light from a stationary object is registered as alterations of signals detected by the different pixels or group of pixels of a CCD. Temporal intensity modulation is registered at laser beam scanning upon a stationary tissue rough surface or when motion of cells (or other scattering particles) exists. These fluctuations are characterized by the mean value of the intensity $\langle I \rangle$ and the standard deviation σ_I (see Fig. 3.19c). The object itself is characterized by the standard deviation σ_h of the altitudes (depths) of inhomogeneities and the correlation length L_c of these inhomogeneities (random relief).

Since many tissues and cells are phase objects, for which only refractive index variations are important on the background of negligible absorption, the propagation of coherent beams in tissues can be described on the basis of a random phase screen (RPS)

model. The amplitude transmission coefficient of an RPS is given by [5, 9, 40-42, 48, 56-59]

$$t_s(x,y) = t_0 \exp\{-i\Phi(x,y)\}, \qquad (3.59)$$

where t_0 is the spatially independent amplitude transmission; $\Phi(x, y)$ is the random phase shift introduced by the RPS at the (x, y) point. Such spatial phase fluctuations may be due to variations in the refractive index $n(x, y)$ or the RPS thickness $h(x, y)$ from point to point. For thin transmitting and reflecting RPSs, we have

$$\Phi_t(x,y) = \left(\frac{2\pi}{\lambda}\right)[n(x,y)-1]h(x,y), \qquad (3.60)$$

$$\Phi_r(x,y) = \frac{4\pi}{\lambda}\cdot h(x,y), \qquad (3.61)$$

respectively. Phase fluctuations of the scattered field are characterized by the standard deviation σ_ϕ and the correlation length L_ϕ. Generally, there are two types of RPSs: weakly scattering RPSs ($\sigma_\phi^2 \ll 1$) and deep RPSs ($\sigma_\phi^2 \gg 1$).

Ideal conditions for formation of speckles, when completely developed speckles arise, can be formulated as the following. Coherent light irradiates a diffusive surface (or a transparency) characterized by Gaussian variations of the optical path $\Delta l(x, y) = \Delta[n(x, y)h(x, y)]$, where $n(x, y)$ is the profile of the index of refraction and $h(x, y)$ is the profile of height (thickness), with standard deviation of the optical path variations, $\sigma_l \gg \lambda$. Both the coherence length of light and sizes of the scattering area considerably exceed the differences in optical paths due to the surface relief, and many scattering centers contribute to the resulting speckle pattern.

Statistical properties of speckles can be divided into statistics of the first and second orders. Statistics of the first order describes the properties of speckle fields at each point. Such a description usually employs the intensity probability density distribution function $p(I)$ and the contrast

$$V_I = \frac{\sigma_I}{\langle I\rangle}, \qquad (3.62)$$

$$\sigma_I^2 = \langle I^2\rangle - \langle I\rangle^2, \qquad (3.63)$$

where $\langle I\rangle$ and σ_I^2 are the mean intensity and the variance of the intensity fluctuations, respectively. In certain cases, statistical moments of higher orders are employed.

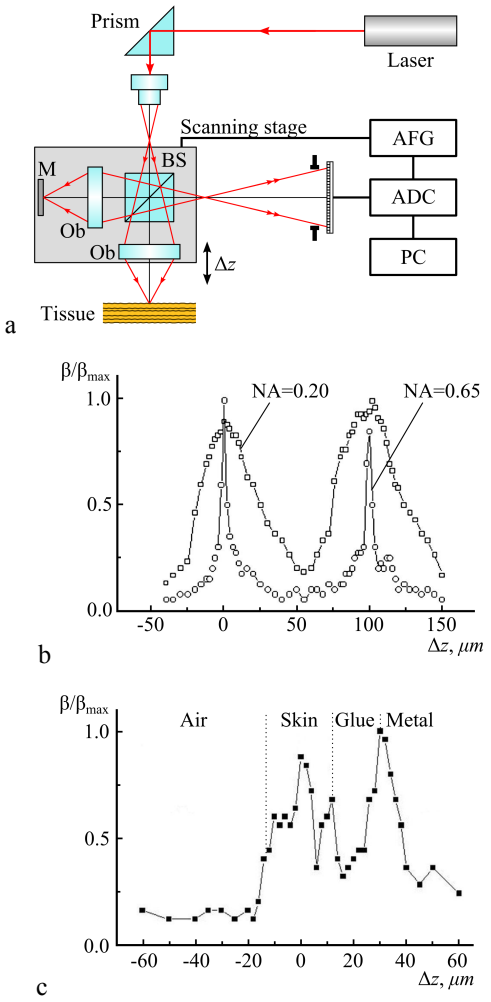


Fig. 3.20 Laser speckle interferometer with the matched wave fronts (a): Laser – He-Ne laser (633 nm), Ob – objectives, BS – beam splitter, M – reference mirror, PD – photodetector, AFG – audio-frequency generator, ADC – analog-to-digital converter, PC – personal computer; the normalized interferometer signal as a function of depth for a test-object – 150 μm plane-parallel glass plate ($n \cong 1.5$) (b); in-depth profiling of the metal-glue-stripped human skin epidermal layer (c) [5, 59].

For ideal conditions, when the complex amplitude of scattered light has a Gaussian statistics, the contrast is $V_I = 1$ (developed speckles), and the intensity probability distribution is represented by a negative exponential function:

$$p(I) = \frac{1}{\langle I\rangle}\exp\left\{-\frac{I}{\langle I\rangle}\right\}. \qquad (3.64)$$

Thus, the most probable intensity value in the corresponding speckle pattern is equal to zero, i.e., destructive interference occurs with the highest probability.

Partially developed speckle fields are characterized by a contrast $V_I < 1$. The contrast may be lower due to a

uniform coherent or incoherent background added to the speckle field. For the phase objects with the variance of the phase fluctuations $\sigma_\phi^2 >> 1$ and a small number of scatterers within a focused laser beam contributing to the field at a certain point in the observation plane, the contrast of the speckle pattern is greater than unity. The statistics of the speckle field in this case is non-Gaussian and nonuniform (i.e., the statistic parameters depend on the observation angle). The specific features of the diffraction of focused laser beams from moving phase screens underlie speckle methods of structural diagnostics and monitoring of motion parameters of tissues and flows of blood and lymph.

Statistics of the second order shows how fast the intensity changes from point to point in the speckle pattern, i.e., characterizes the size and the distribution of speckle sizes in the pattern. Statistics of the second order is usually described in terms of the autocorrelation function of intensity fluctuations,

$$G_2(\Delta\xi) = \langle I(\xi) \cdot I(\xi + \Delta\xi) \rangle \tag{3.65}$$

and its Fourier transform, representing the power spectrum of a random process; $\xi \equiv x$ or t is the spatial or temporal variable; $\Delta\xi$ is the change in variable. Angular brackets $\langle\rangle$ in Eq. (3.65) stand for the averaging over an ensemble or the time.

3.3.2 Speckle interferometry

Often regular and random interference interact between each other when interferometric or holography systems are used for study of scattering tissues. Figure 3.20 presents a dual-beam (two-mirror) speckle interferometer, where focused beams are used and as an objective mirror a tissue sample serves [5, 59]. When reflected light forming a developed speckle pattern retains linear polarization, intensity distribution at the output of such interferometer can be written as

$$\begin{aligned} I(r,t) &= I_r(r) + I_s(r) + 2\left[I_r(r) I_s(r)\right]^{1/2} \times \\ &\times \left|\gamma_{11}(\Delta t)\right| cos\left\{\Delta\Phi_I(r) + \Delta\Psi_I(r) + \Delta\Phi_I(r)\right\}, \end{aligned} \tag{3.66}$$

where I_r (r) and I_s (r) are intensity distributions of the reference and signal fields, respectively; r is the transverse spatial coordinate; $\gamma_{11}(\Delta t)$ is the degree of temporal coherence of light; $\Delta\Psi_I(r)$ is the deterministic phase difference of the interfering waves; $\Delta\Phi_I(r) = \left[\Phi_{Ir}(r) - \Phi_{Is}(r)\right]$ is the random phase difference; and $\Delta\Phi_I(t)$ is the time-dependent phase difference related to the motion of an object. In particular, for the longitudinal sinusoidal oscillations of one of the interferometer mirrors (reference mirror M or object itself) with the amplitude l_0 and angular frequency Ω_υ

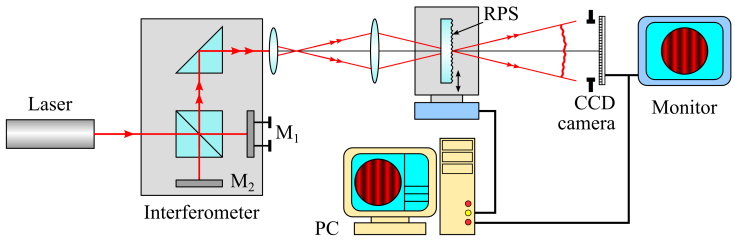
$$\Delta\Phi_I(t) = \frac{4\pi}{\lambda} l_0 \, sin(\Omega_\upsilon t). \tag{3.67}$$

In the absence of speckle modulation, the deterministic phase difference $\Delta\Psi_I(r)$ governs the formation of regular interference fringes as in conventional interferometry. The output signal of a speckle interferometer is maximal for the phase-matched interfering fields, when $\Delta\Psi_I(r) = \text{const}$ within the aperture of the detector, and for interference of focused laser beams, when speckles with maximal sizes are generated. For the large aperture of a photodetector, when speckles are not resolved, the output signal of the interferometer

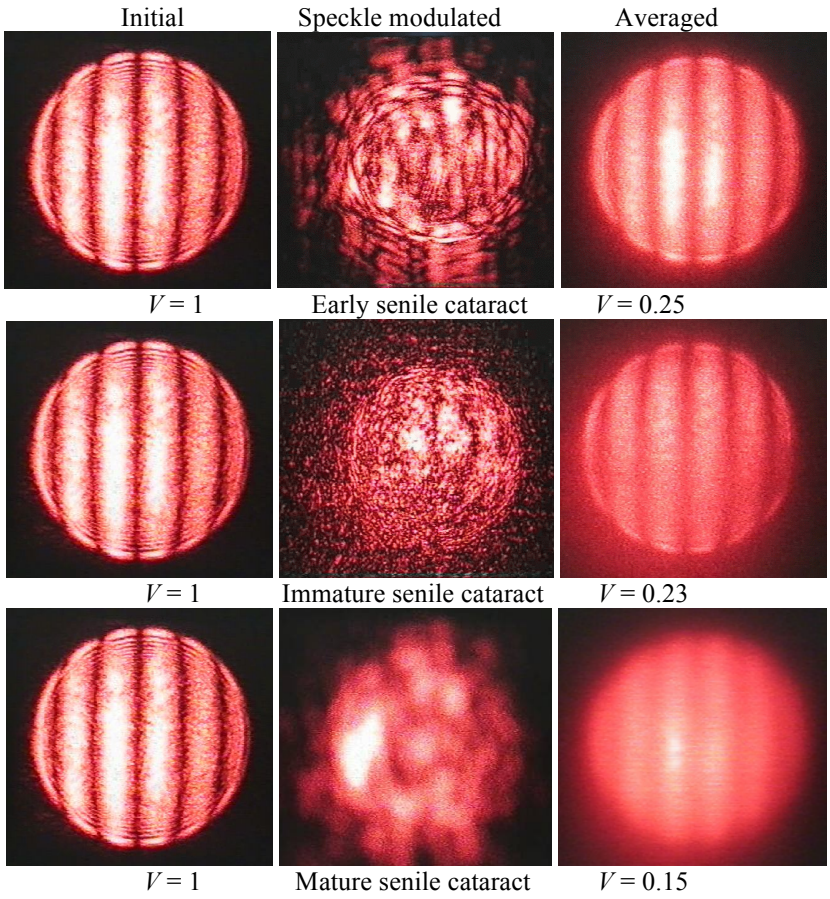
$$\beta(\Delta z) = \frac{sin\left(\dfrac{\pi(\mathrm{NA})^2 n\Delta z}{\lambda_0}\right)}{\dfrac{\pi(\mathrm{NA})^2 n\Delta z}{\lambda_0}}, \tag{3.68}$$

where NA is the numerical aperture of the objective, λ_0 is the wavelength in free space; n is the index of refraction of a sample (tissue), Δz is the in-depth displacement. It follows that the in-depth spatial resolution ($\beta \rightarrow 0$) of the interferometer is $\Delta z_{min} = \dfrac{\lambda_0}{n(\mathrm{NA})^2}$, thus for the objectives with NA close to unity, resolution is close to the wavelength. The normalized interferometer's signal as a function of depth for a test–object – 150 μm plane–parallel glass plate with index of refraction $n \cong 1.5$ presented in Fig. 3.20b demonstrates an increase of spatial in-depth resolution at using of objectives with the bigger numerical aperture. Two – anterior and posterior – interfaces of the plate are well resolved. Similar in depth scanning of the *in vivo* taken glue-stripped human skin *stratum corneum* sample, which is attached to a metal plate by a glue layer, also shows rather good spatial resolution of the structure of thin tissue layers (Fig. 3.20c). Important to note, that independent measurement of specimen thickness allows one to evaluate mean index of refraction of sample material.

The regularly spatially modulated laser beams are often used for surface profiling, laser anemometry of biological fluids, and cytometry [56, 59]. Typically these methods take advantage of a small spacing of interference fringes Λ_I,



a



b

Fig. 3.21 Interaction of the spatially-modulated laser beam with cataractous eye lenses: experimental setup with external interferometer with the focused beams on the specimen modeled as a random phase screen (RPS) (a); observed interferograms (b): without a specimen (initial, the visibility is equal to unity, $V = 1$) (left column), with a stationary specimen (cataractous eye lens for different severity of the disease, from early to mature senile cataract)(middle column), and with a movable specimen (averaged) – observation of the average intensity fringes with contrast from $V = 0.25$ to 0.15 (right column) [5, 59].

$$\Lambda_I = \frac{\lambda}{2\theta_I}, \qquad (3.69)$$

which is comparable to the sizes of inhomogeneities of the object under study. Here θ_I is the angle between the wave vectors of the interfering fields. If the separation between the interference fringes is small, $\Lambda_I < d_{av}$ [the average size of speckles in the observation plane, see Eq. (3.58)], and the diameter of the beam waist $2w_0 > L_\phi$ [the correlation length of phase fluctuations, see Eq. (3.61)], the regular interference fringes oriented in a random manner from speckle to speckle are observed within the limits of a single speckle. The contrast of fringes depends in this case only on the relation between the intensities of the interfering fields and does not depend on the statistical properties of an object structure, that gives an opportunity to measure regular phase shifts in the object in spite of its random nature.

The use of modulated beams with a large spacing between interference fringes, which exceed the sizes of inhomogeneities, $\Lambda_I > d_{av}$, results in the appearance of another correlation effects in the scattered field. If the

beam diameter $2w_0$ and the separation between the fringes Λ_f are sufficiently large, the fringes modulate the speckle field, and the evolution of the contrast of average-intensity fringes along the beam propagation (along z-axis) is determined by the statistical parameters of the object:

$$\bar{V}_I(z) = |r_c(z)| V_I, \tag{3.70}$$

where V_I is the contrast in the initial laser beam and $|r_c(z)|$ is the modulus of the transverse correlation coefficient of the complex amplitude of the scattered field. Contrast of the interferential fringes is measured for the incident light as

$$V_I = \frac{I_{max} - I_{min}}{I_{max} + I_{min}}, \tag{3.71}$$

and for light propagating after the object at interferential pattern averaging by transverse scanning, $\bar{V}_I(z)$ is measured using the similar formula for each z position.

When a spatially modulated light beam is focused using a diffraction-limited optical system with an aperture $D > \Lambda_f$, two spatially separated light spots are produced in the area of focusing. The optical scheme for such system is presented in Fig. 3.21a. Since two different areas of an object are irradiated, the interaction of these light spots with a scattering medium gives rise to two completely nonidentical (noncorrelated) speckle fields in the diffraction field. If $\Lambda_f > d_{av}$ and $2w_0 > L_\phi$, no fringes occur in the scattered field (see Fig. 3.21b). However, when an object moves (scanned) in the transverse direction, a set of average-intensity interference fringes arises (see Fig. 3.21b, right column). The contrast of this pattern is determined by the statistical properties of the specimen structure expressed as the standard deviation σ_ϕ and the correlation length L_ϕ of phase fluctuations of the interacting field.

3.4 Dynamic light scattering

3.4.1. Quasi-elastic light scattering (QELS) and Doppler effect

Scattering of light by movable particles is called dynamic light scattering in contrast to scattering of light by none movable or static particles, which is called static or elastic scattering as it occurs without energy transfer [5, 9, 43-56, 60]. Instead, at scattering by a movable particle small but measurable light energy change occurs, thus dynamic light scattering is often called as a quasi-elastic light scattering (QELS). The basic phenomenon for QELS is Doppler effect that determines the frequency shift of the scattered light by a well-known expression valid for non-relativistic velocities (Fig. 3.22)

$$\Delta\nu_D = (\nu_s - \nu_0) = \\ = \nu_0 \frac{\upsilon}{c}(cos\theta_i - cos\theta_s) = (\vec{k}_s - \vec{k}_0)\bar{\upsilon}, \tag{3.72}$$

were ν_s is the frequency of the scattered wave, ν_0 is the frequency of the incident wave, υ is the velocity of the scatterer (particle), c is the light speed, θ_i is the angle between wave vector of the incident light $\vec{k}_0$ and direction of particle motion $\vec{\upsilon}$, and θ_s is the angle between directions of particle motion $\vec{\upsilon}$ and detection of the scattered radiation $\vec{k}_s$.

The Doppler shift is proportional to velocity of the light scattering particle. Therefore, measurement of the Doppler shift for known geometry of the experiment (angles θ_i and θ_s) allows one to determine velocity of a particle or ensemble of the co-directional particles. This is the principle of the Doppler velocimetry. However for living systems different velocities and directions are more characteristic. Thus, a number of Doppler frequencies are measured, i.e., Doppler spectrum, which in principle allows one to reconstruct particle velocity and direction distributions. Such measurement is recognized as Doppler spectroscopy or QELS spectroscopy, or photon-correlation spectroscopy. The last term underlines a fundamental relationship between spectrum and autocorrelation function of intensity fluctuations caused by Doppler signals from many scatterers.

The Doppler shift induced by blood flow and any other flows in the body is too small to be detected directly by a spectrometer. For example, for typical blood flow velocity of 1 cm/s, the Doppler shift is less than 10 kHz. However, application of lasers and optical mixing (heterodyning or self-beating) technique using a photodetector give a possibility to provide easily such measurements. The current of a photodetector is proportional to light intensity. Thus, with allowance for self-beating of the electric components of the scattered field, the temporal intensity autocorrelation function (AF) $G_2(\tau)$ can be measured. For the Gaussian random optical fields, when the scattering field phase and amplitude variations are statistically independent of each other, $G_2(\tau)$ is related to the first-order AF by the Siegert formula:

$$g_2(\tau) = \frac{G_2(\tau)}{\langle I \rangle^2} = A\left\{1 + \beta_{sb} |g_1(\tau)|^2\right\}. \tag{3.73}$$

Here, $G_2(\tau)$ is defined by Eq. (3.65); $\langle I \rangle$ is the ensemble-averaged intensity; τ is the delay time; $A = \langle i^2 \rangle$ is the mean of the square of the photocurrent, or the

base line of the AF; β_{sb} is the parameter of self-beating efficiency, typically $\beta_{sb} \approx 1$; and

$$g_1(\tau) = \frac{\langle E(t)E^*(t+\tau)\rangle}{\langle |E(\tau)|^2 \rangle} \qquad (3.74)$$

is the normalized temporal AF of the optical field, $E(t)$ is the electrical field for the time t and $E^*(t+\tau)$ is the complex conjugate of electrical field for $(t + \tau)$.

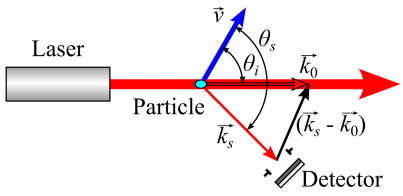


Fig. 3.22 Laser light scattering by a moving particle: θ_i is the angle between wave vector of the incident light $\vec{k}_0$ and direction of particle motion $\vec{\upsilon}$, θ_s is the angle between directions of particle motion $\vec{\upsilon}$ and detection of the scattered radiation $\vec{k}_s$ [55].

For a monodisperse system of Brownian particles

$$g_1(\tau) = exp(-\Gamma_T \tau), \qquad (3.75)$$

where

$$\Gamma_T = q^2 D_T \qquad (3.76)$$

is the relaxation parameter,

$$q = |\vec{k}_s - \vec{k}_0| = \frac{4\pi}{\lambda} sin\frac{\theta}{2} \qquad (3.77)$$

is the module of the scattering wave vector, $\theta = \theta_s - \theta_i$ (Fig. 3.22);
and

$$D_T = \frac{k_B T}{6\pi\eta_m r_h} \qquad (3.78)$$

is the coefficient of translation diffusion, k_B is the Boltzmann constant, T is the absolute temperature, η_m is the absolute viscosity of the medium, and r_h is the hydrodynamic radius of a particle.

One of the aims of QELS spectroscopy is the reconstruction of size distribution of scattering particles (biological molecules, cell organelles, cells, etc.) which is the valuable information for early diagnostics and noninvasive monitoring of some diseases. However, QELS algorithms work well only for a single scattering regime.

3.4.2. Dynamic speckles

When random moving (dynamic) object is irradiated by a coherent light a dynamic speckle-pattern is formed [5, 9, 43-56, 60, 61]. This means that phase and intensity of scattered light have a pure stochastic nature. Laser speckle-correlation technique is based on the space-time correlation properties of dynamic speckle field. It allows one to measure the scattering object velocity.

If the scatterers are in random motion, e.g., in Brownian motion, optical speckles obey to the Gaussian statistics and the spatial-temporal correlation function of the complex amplitude of the scattered light can be factorized and presented as a product of spatial and temporal correlation functions. On the other hand, tissue is more appropriate to be modeled as a moving deep random phase screen (RPS) for which the spatial and temporal intensity fluctuations are not statistically independent from each other, thus a spatial-temporal correlation function is introduced to describe dynamic speckles.

For a diffuse object moving in-plane with velocity $\vec{\upsilon}$ (Fig. 3.23) and contained a large number of randomly distributed scattering centers within irradiating laser beam with assuming that phase fluctuations of the scattered field obey to the Gaussian statistics and the phase variation is large $\sigma_\phi^2 >> 1$, the normalized spatial-temporal correlation function of stationary process may be written as

$$g_2(\vec{r},\tau) = \frac{\langle I_1 I_2 \rangle}{\langle I_1 \rangle \langle I_2 \rangle} = 1 + |g_1(\vec{r},\tau)|^2, \qquad (3.79)$$

where

$$g_1(\vec{r},\tau) = \frac{\langle E_1 E_2^* \rangle}{\sqrt{\langle E_1 E_1^* \rangle \langle E_2 E_2^* \rangle}} \qquad (3.80)$$

is the spatial-temporal correlation function of the complex amplitude of the scattered field; $\vec{r} = \vec{X}_1 - \vec{X}_2$, $\tau = t_1 - t_2$.

For the specific case of Gaussian laser beam illumination [see Eq. (1.5)] [1] with the beam axis normal to the object plane and beam waist apart at a distance z from the object plane (see Fig. 3.23), the beam spot radius w_b and radius of wavefront curvature ρ_b in the object plane are determined by the following expressions [55]:

$$w_b = w_0\left[1+\left(\frac{z}{a_b}\right)^2\right]^{1/2}, \rho_b = z\left[1-\left(\frac{a_b}{z}\right)^2\right], \quad (3.81)$$

where $a_b = \pi w_0^2/\lambda$, and the normalized spatial-temporal correlation function of intensity of scattered light in observation plane, which is apart at the distance l from the object plane, is denoted as

$$g_2(\vec{r},\tau)-1 = \\ = exp\left(-\frac{|\vec{\upsilon}|^2}{w_b^2}\tau^2\right)exp\left(-\frac{1}{r_s^2}\left|\vec{r}-\left(1+\frac{l}{\rho_b}\right)\vec{\upsilon}\tau\right|^2\right), \quad (3.82)$$

where,

$$r_s = \frac{2l}{k_0 w_b} \quad (3.83)$$

is the mean speckle size in the observation plane. As can be seen from Eq. (3.82), speckles translate in the observation plane with velocity differ from the velocity of the object (RPS) $\vec{\upsilon}$

$$\vec{\upsilon}_s = \frac{\vec{r}}{\tau} = \left(1+\frac{l}{\rho_b}\right)\vec{\upsilon}. \quad (3.84)$$

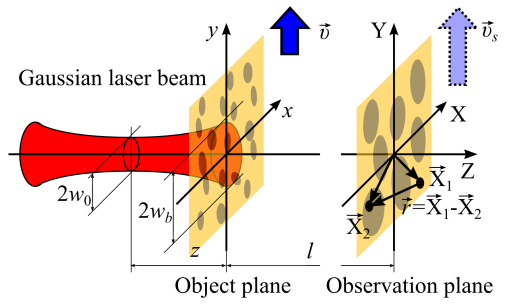


Fig. 3.23 Scattering of the Gaussian laser beam by a random phase screen moving with a velocity $\vec{\upsilon}$ in perpendicular direction to the beam axis [55].

The motion of dynamic speckles may arise in two different modes, namely, speckles moving without changing the structure, called *"speckle translation"* and the speckle changing only the structure in time without translation, called *"speckle boiling"*. The "*speckle boiling*" mode is characteristic for the random distribution of particle velocities. For the regular velocity of the RPS, speckles also move in a regular manner, thus *"speckle translation"* mode is realized. For flows of liquids, the combination of these two modes is typical.

In pure translational mode the time, which is required to change the realization of scatterers under the illuminating beam, is equal to

$$\tau_T = \frac{w_b}{|\vec{\upsilon}|}. \quad (3.85)$$

Taking into account Eq. (3.84) the translation distance can be estimated as:

$$r_T = \left(1+\frac{l}{\rho_b}\right)w_b. \quad (3.86)$$

The described dependence of speckle dynamics on velocity of the object is the basis of the speckle-correlation technique of velocity measurement. The main idea of this technique is to measure speckle translation velocity in the observation plane and then recalculate the object velocity using Eq. (3.84). One of the simplest way to measure the velocity of speckle translation is to record the intensity fluctuation at two spatially separated points in the observation plane. If distance between observation points is less than r_T two similar records delayed by the time τ_d will be obtained. Value τ_d exactly corresponds to the time, which is required for speckle motion from one point to another. It could be easily measured using cross-correlation technique.

3.4.3 Speckle pattern blurring effect – full-field velocity measurements

The spatial distribution of contrast of a dynamic speckle pattern at its time-integration can be employed as a detecting parameter to provide a full-field velocity measuring technique [5, 46-55]. If the integration time is comparable with the period of the intensity fluctuations caused by dynamic light scattering, the effect of coherent light interaction with a RPS will be a blurring of the recorded speckle pattern – a reduction in the speckle contrast. It is clear that a very short exposure time would "freeze" the speckle and result in a high-contrast speckle pattern, whereas a long exposure time would allow the speckles to average out, leading to a low contrast.

The use of such *time-integrated speckle* led in the early 1980s to a technique for blood flow imaging that simultaneously achieves full-field operation and robust data collection and processing. Originally called "single-exposure speckle photography", it has been developed into a fully-digital, real-time technique for the mapping of capillary blood flow of skin and other tissues and called "laser speckle contrast analysis" (LASCA).

LASCA uses only a laser with diverging optics, a CCD camera, a frame-grabber and a PC. Specially developed software computes the local contrast and converts it to a false-color map of contrast (and hence of velocity). The contrast is quantified by the ratio of the

standard variation of the intensity fluctuations to the mean intensity, $\frac{\sigma_I}{\langle I \rangle}$ [see Eq. (3.62)]. The image is a time-integrated exposure, but for capillary blood flow the exposure is short enough to render the technique effectively real-time. Figure 3.24 illustrates the simplicity of the LASCA basic setup. Light from the laser is diverged by simple optics to illuminate the area under investigation. The CCD camera images the illuminated area, the frame-grabber captures an image and the software immediately processes it to produce a false-color contrast map indicating velocity variations which is displayed by PC monitor. This is typically accomplished in less than one second, making the technique effectively real-time. The number of pixels over which the speckle contrast is computed is of great importance because for a few pixels used the statistics will be questionable, and for too many – the spatial resolution will be lost. In practice, a square of 7×7 or 5×5 pixels is usually a satisfactory compromise.

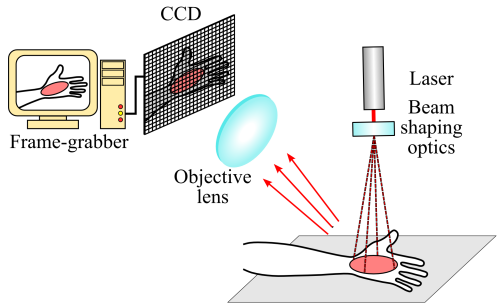


Fig. 3.24 Full-field imaging of dynamic speckles [60].

By making certain assumptions, the following mathematical relationship between the speckle contrast and the temporal statistics of the fluctuating speckles can be found:

$$\sigma_I^2(T) = \frac{1}{T}\int_0^T \tilde{G}_2(\tau)\mathrm{d}\tau \qquad (3.87)$$

where σ_I^2 is the *spatial* variance of the intensity in the speckle pattern; T is the integration time and $\tilde{G}_2(\tau)$ is the autocovariance of the *temporal* intensity fluctuations of a single speckle; $\tilde{G}_2(\tau)$ is defined as [see Eq. (3.65)]

$$\tilde{G}_2(\Delta\xi) = \left[I(\xi) - \langle I \rangle\right] \cdot \left[\left\langle I(\xi + \Delta\xi) - \langle I \rangle \right\rangle\right]. \qquad (3.88)$$

This fundamental equation defines the relationship between LASCA and those techniques that measure the intensity fluctuations directly. LASCA measures the quantity on the left side of Eq. (3.87); photon correlation spectroscopy, laser Doppler, and time-varying speckle techniques measure the quantity on the right side. In addition, LASCA uses *image speckles,* whereas most of the temporal techniques use *far-field speckles*. However, this does not detract from the fundamental equivalence of the two approaches expressed in Eq. (3.87).

All the techniques allow for the determination of the correlation time of intensity fluctuations τ_c. The photon correlation technique measures this parameter directly. In the case of LASCA, some further assumptions must be made in order to link the measurement of speckle contrast with τ_c. For example, for the case of a Lorentzian velocity distribution, this relation has a view:

$$\frac{\sigma_I}{\langle I \rangle} = \left[\frac{\tau_c}{2T}\left\{1 - exp\left(-\frac{2T}{\tau_c}\right)\right\}\right]^{1/2}. \qquad (3.89)$$

LASCA, as all the *temporal* measurement techniques, suffers on the problem of relating the correlation time τ_c to the velocity distribution of the scatterers. The relation depends on the multiple scattering, the size and the shape of the scattering particles, non–Newtonian flow, non-Gaussian statistics resulting from a low number of scatterers in the measuring volume, spin of the scatterers, etc. Because of the uncertainties caused by these factors, it is common in all these techniques to rely mainly on calibration rather than on absolute measurements.

3.4.4 Diffusion wave spectroscopy

A fundamental difference of diffusion wave spectroscopy (DWS) compared to the QELS spectroscopy is that this approach is applicable in the case of dense media with multiple scattering, which is very important for tissues [5, 52, 53, 61]. It is assumed thereby that due to multiple scattering the each photon that has reached given observation point of the detector experiences a great number of scattering events N (Fig. 3.25). The successive scattering acts taking place at the time instant t at the scattering particles located in points $\vec{r}_1(t), \vec{r}_2(t), \ldots \vec{r}_i(t) \ldots \vec{r}_N(t)$ of the medium with wave vectors $\vec{k}_1, \vec{k}_2, \ldots \vec{k}_i \ldots \vec{k}_N$, result in formation of the field $\vec{E}(t)$, whose total phase change $\Delta\phi(t)$ is determined as:

$$\Delta\phi(t) = \sum_{i=0}^{N} \vec{k}_i(t)\left[\vec{r}_{i+1}(t) - \vec{r}_i(t)\right]. \qquad (3.90)$$

$\Delta\phi(t)$ is dependent on the total path length L of each photon migrated from the source $\vec{r}_0$ to the detector $\vec{r}_{N+1}$ points (Fig. 3.25):

$$L = \sum_{i=0}^{N}\left|\vec{r}_{i+1}(t) - \vec{r}_i(t)\right| = \sum_{i=0}^{N}\left(\frac{\vec{k}_i}{|\vec{k}_i|}\right)\left[\vec{r}_{i+1}(t) - \vec{r}_i(t)\right]. \qquad (3.91)$$

The total mean photon path length L is related to the number of scattering acts N by the relation $L = Nl_s$, where $l_s = (\mu_s)^{-1}$.

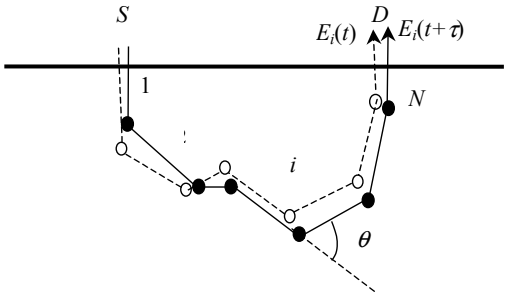


Fig. 3.25 Schematic diagram of the coherent radiation propagation through a randomly inhomogeneous semi-infinite medium with a multiple scattering; light passes from the radiation source (S) towards the detector (D); the location of scattering particles at the time instant τ is indicated by (o) and at the time instant $(t+\tau)$ – by (•); 1, 2, …, i, …, N are the first-, second-, i-th-, and N-th-step of scattering; θ is the scattering angle.

In contrast to the case of single scattering, the autocorrelation function (AF) of the field $g_1(\tau)$ [see Eq. (3.74)] is sensitive to the motion of a particle on the length scale on the order of $\lambda\sqrt{l_{tr}/L}$, which is generally much less than λ, because $L >> l_{tr}$ [see Eqs. (3.42) and (3.43)]. Thus, DWS AFs decay much faster than AFs employed in QELS.

Experimental implementation of DWS is very simple. A measuring system should provide irradiation of an object under study by a CW laser beam and measurement of intensity fluctuations of the scattered radiation within a single speckle with the use of a single-mode receiving fiber, photomultiplier, photon-counting system, and a fast digital correlator working in a nanosecond range. The possibilities of the DWS technique for medical applications have been demonstrated for the blood flow monitoring in the human forearm and brain. The AF slope is the indicative parameter for determination of the blood flow velocity. The normalized AF of field fluctuations can be represented in terms of two components related to the Brownian and directed motion of scatterers (erythrocytes):

$$g_1(\tau) \approx exp\left\{-2\left[\frac{\tau}{\tau_B}+\left(\frac{\tau}{\tau_S}\right)^2\right]\frac{L}{l_{tr}}\right\}, \qquad (3.92)$$

where $\tau_B^{-1} \equiv \Gamma_T = q^2 D_T$ [see Eq. (3.76)], $\tau_S^{-1} \cong 0.18 G_V q l_{tr}$ characterizes the directed flow, and G_V is the gradient of the flow rate. It allows one to express the slope of the AF in terms of the diffusion coefficient D_T (characterizes blood microcirculation) and the gradient of the directed velocity of blood G_V.

When spatially-resolved single speckle detection is provided, the technique is transformed to diffusion wave imaging (DWI) mode.

3.5 Interaction of the polarized light with tissues

3.5.1 Definitions

Light of arbitrary polarization can be represented by four numbers known as the Stokes parameters, I, Q, U, and V: I – refers to the intensity of the light; the parameters Q, U, and V represent the extent of horizontal liner, 45º linear, and circular polarization, respectively [5, 9, 56, 62-71]. In terms of the electric field components the Stokes parameters are given by

$$\begin{aligned} I &= \left\langle E_\parallel E_\parallel^* + E_\perp E_\perp^* \right\rangle, \\ Q &= \left\langle E_\parallel E_\parallel^* - E_\perp E_\perp^* \right\rangle, \\ U &= \left\langle E_\parallel E_\perp^* + E_\perp E_\parallel^* \right\rangle, \\ V &= \left\langle i\left(E_\parallel E_\perp^* - E_\perp E_\parallel^*\right) \right\rangle, \end{aligned} \qquad (3.93)$$

and the irradiance or intensity of light by

$$I^2 \geq Q^2 + U^2 + V^2 . \qquad (3.94)$$

For an elementary monochromatic plane or spherical electromagnetic wave, Eq. (3.94) is the equality. For a partially polarized quasi-monochromatic light which can be presented as a mixture of elementary waves, the Stokes parameters are sums of the respective Stokes parameters of these elementary waves, because of fundamental property of additivity. In this case Eq. (3.94) is the inequality.

The Stokes vector $\vec{S}$ of a light beam is constructed basing on six flux measurements obtained with different polarization analyzers in front of the detector:

$$\vec{S} = \begin{pmatrix} I \\ Q \\ U \\ V \end{pmatrix} = \begin{pmatrix} I_H + I_V \\ I_H - I_V \\ I_{+45^\circ} - I_{-45^\circ} \\ I_R - I_L \end{pmatrix}, \qquad (3.95)$$

where I_H, I_V, $I_{+45°}$, $I_{-45°}$, I_R, and I_L are the light intensities measured with a horizontal linear polarizer, a vertical linear polarizer, a +45° linear polarizer, a –45° linear polarizer, a right circular analyzer, and a left circular analyzer in front of the detector, respectively. Because of the relationship $I_H + I_V = I_{+45°} + I_{-45°} = I_R + I_L = I$, where I is the intensity of the light beam measured without any analyzer in front of the detector, a Stokes vector can be determined by four independent measurements.

The degree of linear (L) and circular (C) polarization of the scattered light is defined as

$$P_L = \frac{I_{\parallel} - I_{\perp}}{I_{\parallel} + I_{\perp}} = \frac{\sqrt{Q_s^2 + U_s^2}}{I_s}, \tag{3.96}$$

and

$$P_C = \frac{\sqrt{V_s^2}}{I_s}. \tag{3.97}$$

The polarization state of the scattered light in the far zone is described by the Stokes vector connected with the Stokes vector of the incident light

$$\vec{S}_s = \mathbf{M} \times \vec{S}_i, \tag{3.98}$$

where $\boldsymbol{M}$ is the normalized 4×4 scattering matrix (intensity or Mueller matrix)

$$\mathbf{M} = \begin{bmatrix} M_{11} & M_{12} & M_{13} & M_{14} \\ M_{21} & M_{22} & M_{23} & M_{24} \\ M_{31} & M_{32} & M_{33} & M_{34} \\ M_{41} & M_{42} & M_{43} & M_{44} \end{bmatrix}, \tag{3.99}$$

and $\vec{S}_i$ is the Stokes vector of the incident light.

The light scattering matrix (LSM) elements depend on the scattering angle θ, the wavelength, and geometrical and optical parameters of the scatterers. There are only seven independent elements (of sixteen) for the scattering matrix of a single particle with fixed orientation and nine relations, which connect the others together. For scattering by a collection of randomly oriented scatterers, there are 10 independent parameters.

The element M_{11} is what is measured when the incident light is unpolarized. The angular dependence of $M_{11}(\theta)$ is the phase function of the scattered light for the single scattering mode [see Eqs. (3.27), (3.37), and (3.38)]. The M_{11} is much less sensitive to chirality and long-range structure than some of the other matrix elements. The M_{12} element refers to a degree of linear polarization of the scattered light. A good measure of scatterer nonsphericity is the M_{22} element which displays the ratio of depolarized light to the total scattered light. The unique characteristic for different biological systems is the M_{34} element which displays the transformation of 45º obliquely linear polarized incident light to circularly polarized scattered light, because many tissues or tissues constitutes are birefringent and work as a phase plate (retarder). The difference between the M_{33} and M_{44} elements is also a good measure of scatterer nonsphericity.

In addition to definitions of degree of polarization [Eqs. (3.96) and (3.97)], the diattenuation (linear dichroism) is introduced as

$$D_A = \frac{P_1^2 - P_2^2}{P_1^2 + P_2^2} = \frac{\sqrt{M_{12}^2 + M_{13}^2 + M_{14}^2}}{M_{11}}, \tag{3.100}$$

where P_1 and P_2 are the coefficients characterizing the amplitude transmission for the two orthogonal linear polarization states.

To describe polarization-sensitive interaction of light with tissues, different optical models are applicable. For the small particle systems, scattering can be described using Rayleigh theory (see subsection 3.2.3, Eq. (3.23) and Fig. 3.10). For a special class of arbitrary shaped particle systems, where $|m-1| << 1$ and $\frac{2\pi a'}{\lambda}|m-1| << 1$, a' is the largest dimension of the particle, the Rayleigh-Gans or Rayleigh-Debye theory can be used for calculating the scattering properties. For tissues in the NIR a' could be up to 850–950 nm. For describing of near the forward direction scattering caused by large particles (of order of 10 μm) the Fraunhofer diffraction approximation is useful. According to this theory, the scattered light has the same polarization as that of the incident light and the scatter pattern is independent of the refractive index of the object. For the small scattering angles, Fraunhofer diffraction approximation can represent accurately the change in irradiance as a function of particle size. That is why this approach is applicable in the laser flow cytometry. The structure of the biological cell such as cell membrane, nuclear texture, and granules in the cytoplasm can be represented by variations in optical density.

Mie or Lorenz–Mie scattering theory is an exact solution of Maxwell's electromagnetic field equations for a homogeneous sphere (see subsection 3.2.4). In the general case, light scattered by a particle becomes elliptically polarized. For spherically symmetric particles of an optically inactive material the Mueller scattering matrix is given by

$$\mathbf{M}(\theta) = \begin{bmatrix} M_{11}(\theta) & M_{12}(\theta) & 0 & 0 \\ M_{12}(\theta) & M_{22}(\theta) & 0 & 0 \\ 0 & 0 & M_{33}(\theta) & M_{34}(\theta) \\ 0 & 0 & -M_{34}(\theta) & M_{44}(\theta) \end{bmatrix}. \tag{3.101}$$

Mie theory has been extended to arbitrary coated spheres and to arbitrary cylinders. In the Mie theory the electromagnetic fields of the incident, internal and scattered waves are each expanded in a series. A linear transformation can be made between the fields in each

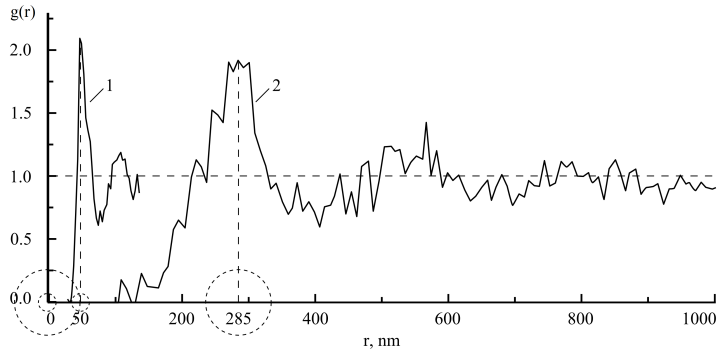


Fig. 3.26 Experimental radial distribution function $g(r)$ for rabbit cornea (1) and human sclera (2); $g(r)$ is proportional to the probability of particle displacement r at a certain distance from an arbitrarily fixed particle (see collagen cylinder faces for rabbit cornea of diameter ~28 nm and for human sclera of diameter ~100 nm for $r = 0$; the nearest the most probable particle position $r \approx 50$ nm for rabbit cornea and $r \approx 285$ nm for human sclera) [5].

of the regions. This approach can also be used for nonspherical objects such as spheroids. The linear transformation is called the transition matrix (T-matrix). T-matrix for spherical particles is diagonal.

3.5.2 Single scattering and quasi-ordered tissues

Many tissues are featured as densely packed disperse systems. Evidently, the interaction of the polarized light with such particle systems may have a number of important peculiarities caused by a specificity of constructive and destructive interference of the scattered waves. For example, eye tissues, such as cornea and lens, in spite of particle structure and refractive index mismatch which causes light scattering by an individual particle, are highly transparent tissues the origin of which is based on their ordered structure (see subsections 2.2 and 2.4, Fig. 2.7) [1]. Light scattering in such systems can be analyzed using the radial distribution function $g(r)$, which statistically describes the spatial arrangement of particles in the system (Fig. 3.26) [5]. For a fibrillar particle system the function $g(r)$ is the ratio of the local number density of the fibril centers at a distance r from a reference fibril at $r = 0$ to the bulk number density of fibril centers. It expresses the relative probability of finding two fibril centers separated by a distance r; thus, $g(r)$ must vanish for values of $r \le 2a$ (a is the radius of a fibril, because fibrils cannot approach each other closer than touching). The radial distribution function of scattering centers $g(r)$ for a certain tissue may be calculated on the basis of tissue electron micrographs (see Figs. 2.7 [1] and 3.26).

Figure 3.26 depicts a typical result for one of the rabbit cornea regions. The function $g(r) = 0$ for $r \le 25$ nm, which is consistent with a fibril radius of 14±2 nm, can be calculated from the electron micrograph similar to that shown for the human cornea in Fig. 2.7b [1]. The first peak in the distribution gives the most probable separation distance, which is approximately 50 nm. The value of $g(r)$ is essentially unity for $r \ge 170$ nm, indicating that the fibril positions are correlated over no more than a few of their nearest neighbors. Therefore, a short-range order exists in the system.

Similar calculations for several regions of the human eye sclera are also shown in Fig. 3.26. Electron micrographs, such as presented in Fig. 2.7d [1], were processed by averaging for 100 fibril centers. The obtained results present evidence of the presence of a short-range order in the sclera, although the degree of order is less pronounced than in the cornea. The function $g(r) = 0$ for $r \le 100$ nm, which is consistent with the mean fibril diameter of ≈100 nm derived from the electron micrograph. The first peak in the distribution gives the most probable separation distance, which is approximately 285 nm. The value of $g(r)$ is essentially unity for $r \ge 750$ nm, indicating a short-range order in the system.

For an isotropic system of N identical interacting long cylinders the scattered intensity in a single scattering approximation is defined as [5, 9]

$$\langle I \rangle = |E_0|^2 N S_2(\theta), \tag{3.102}$$

where E_0 is the scattering amplitude of an isolated (noninteracting) particle,

$$S_2(\theta) = \left\{1 + 8\pi a^2 \rho_c \int_0^R \left[g(r) - 1\right] J_0\left(\frac{2\pi a}{\lambda} r \sin\frac{\theta}{2}\right) \mathrm{d}r\right\} \tag{3.103}$$

is the structure factor; a is the radius of a cylinder face; ρ_c is the mean density of cylinder faces; J_0 is the zero order Bessel function; R is the distance for that $g(r) \to 1$; θ is the scattering angle. For an isotropic system of identical spherical particles in a single scattering approximation

$$\langle I \rangle = |E_0|^2 N S_3(\theta), \tag{3.104}$$

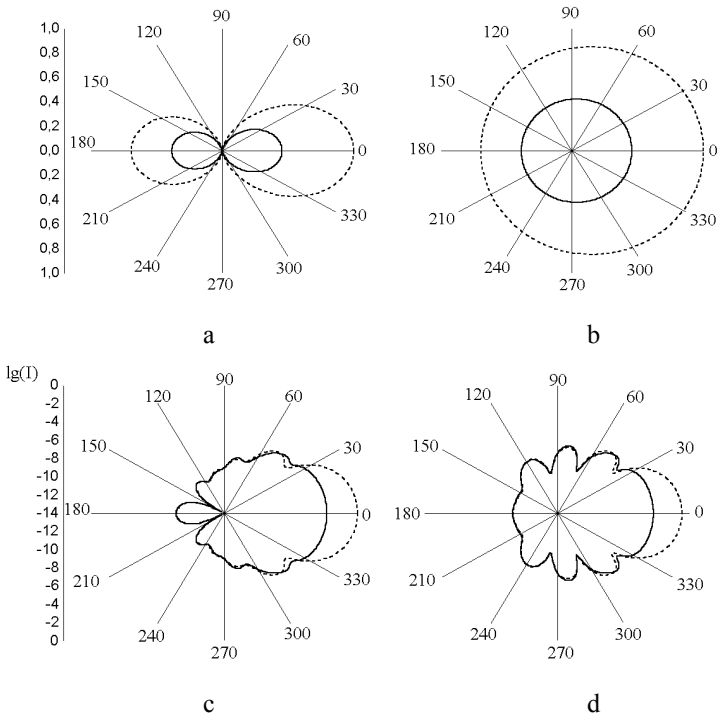


Fig. 3.27 The calculated angular dependences of the scattered intensity for systems of small spherical particles (a = 20 nm) [(a) and (b)] with volume fraction, f = 0.1, and large spherical particles (a = 500 nm) [(c) and (d)] with volume fraction, f = 0.4; the incident wave is linearly polarized parallel [(a) and (c)] with or perpendicular [(b) and (d)] to the scattering plane (see Fig. 3.9); dotted line – independent particles; wavelength, 633 nm; relative refraction index, m=1.105 (calculated by I.L. Maksimova) [5].

$$S_3(\theta)=\left\{1+4\pi\rho_3\int_0^R r^2\left[g(r)-1\right]\frac{\sin qr}{qr}\mathrm{d}r\right\}, \quad (3.105)$$

where $q=\frac{4\pi}{\lambda}sin\frac{\theta}{2}$, ρ_3 is the mean density of particles, and R is the distance for which $g(r)\to 1$. Quantity $S_3(\theta)$ is the 3D structure factor. This factor describes the alteration of the angular dependence of the scattered intensity that appears with a higher particle concentration.

This model can be used to describe polarized light interaction with anisotropic media showing a single scattering. Many tissues composed from optically soft particles (refractive index mismatch of scatterers and surrounding medium is small) and thin enough, such as cornea, eye lens, mucosa, epithelial layers, can be approximated as single scattering systems. The interference between elementary scattered fields, which is accounted for by structure functions $S_2(\theta)$ and $S_3(\theta)$, transforms scattering angular dependences of Mueller matrix elements and corresponding optical properties.

Figure 3.27 illustrates the angular dependences of the scattered intensity for systems of small spherical particles (a = 20 nm) with volume fraction, f = 0.1, and large spherical particles (a = 500 nm) with volume fraction, f = 0.4. The incident wave is linearly polarized parallel with or perpendicular to the scattering plane (see Fig. 3.9). The dotted lines show angular light distributions for the independent (randomly distributed) particles and solid lines – for the ordered particles, for which interference of the scattered fields play a significant role. The overall scattering is suppressed, for the small particle system such suppression is quite isotropic for both polarization states, and for the large particle system the forward directed scattering is mostly suppressed also for both polarization states. As a result both particle systems became more transparent for the incident light. Important to note that for big particle system results for the scattered intensity are presented in the logarithmic scale.

3.5.3 Multiple scattering

Polarized light interactions at light propagation through multiply scattering tissues are fully described by the vector radiative transfer equation (VRTE). For macroscopically isotropic and symmetric plane-parallel scattering media, VRTE can be substantially simplified as follows [5, 29]:

$$\frac{\mathrm{d}\vec{S}(\vec{r},\vartheta,\varphi)}{\mathrm{d}\tau(\vec{r})}=-\vec{S}(\vec{r},\vartheta,\varphi)+\frac{\Lambda(\vec{r})}{4\pi}\times \\ \times\int_{-1}^{+1}\mathrm{d}(cos\,\vartheta')\int_0^{2\pi}\mathrm{d}\varphi'\vec{\mathbf{Z}}(\vec{r},\vartheta,\vartheta',\varphi-\varphi')\vec{S}(\vec{r},\vartheta',\varphi'), \quad (3.106)$$

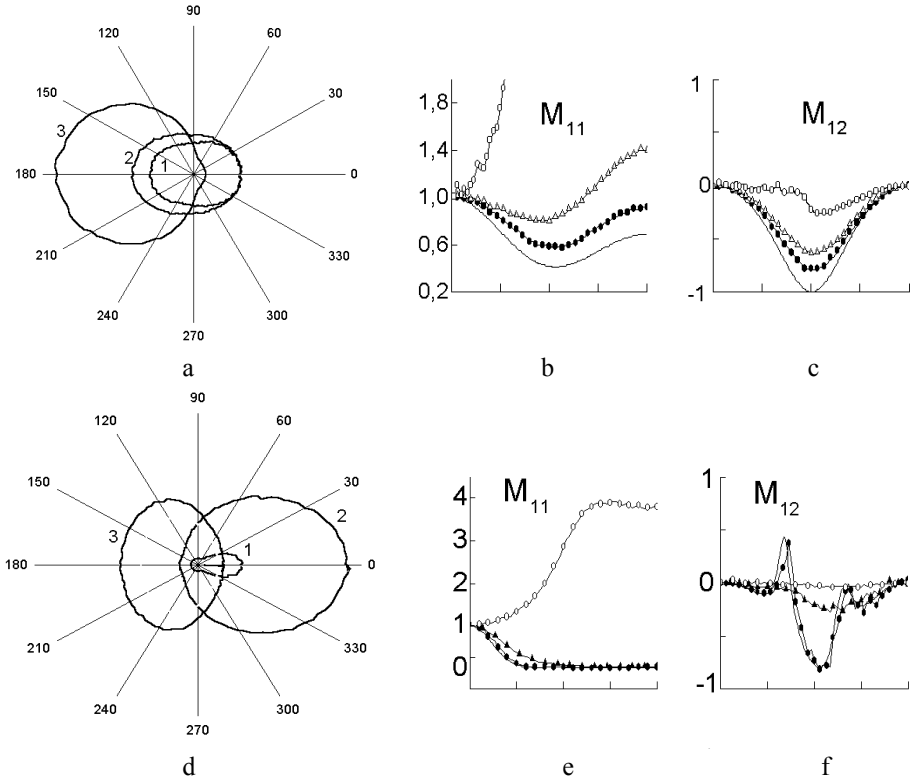


Fig. 3.28 The Monte Carlo simulation of the angular scattering and polarization properties for systems of small spherical particles (a = 50 nm) [(a)-(c)] and large spherical particles (a = 300 nm) [(d)-(f)]; M_{11} – refers to the total scattering intensity and M_{12} – refers to a degree of linear polarization of the scattered light; λ=633 nm, m = 1.2, f = 0.01; single scattering (—); multiple scattering: for the small particles diameter of the spherical system filled up by the particles – 1 mm (•), 2 mm (Δ), and 20 mm (o); and for the large particles diameter of the system – 0.002 mm (•), 0.2 mm (Δ), and 2 mm (o) (calculated by I.L. Maksimova) [5].

where $\vec{S}$ is the Stokes vector [see Eq. (3.95)]; $\vec{r}$ is the position vector; ϑ, φ are the angles characterizing incident direction, respectively, the polar (zenith) and the azimuth angles; $d\tau(\vec{r}) = \rho_p(\vec{r})\langle\sigma_{ext}(\vec{r})\rangle ds$ is the optical path length element, ρ_p is the local particle number density, $\langle\sigma_{ext}\rangle$ is the local ensemble-averaged extinction cross section [$\sigma_{ext} = \sigma_{abs} + \sigma_{sca}$; see Eqs. (3.13) and (3.17)], ds is the path length element measured along the unit vector of the direction of light propagation; Λ is the single scattering albedo [see Eq. (3.20)]; ϑ′ , φ′ are the angels characterizing scattering direction, respectively the polar (zenith) and the azimuth angels; $\vec{\mathbf{Z}}$ is the normalized phase matrix $\vec{\mathbf{Z}}(\vec{r},\vartheta,\vartheta',\varphi-\varphi') = \mathbf{R}(\Phi)\mathbf{M}(\theta)\mathbf{R}(\Psi)$, where $\mathbf{M}(\theta)$ is the single scattering Mueller matrix [see Eq. (3.99)]; θ is the scattering angle, and $\mathbf{R}(\phi)$ is the Stokes rotation matrix for angle ϕ:

$$\mathbf{R}(\phi) = \begin{bmatrix} 1 & 0 & 0 & 0 \\ 0 & \cos 2\phi & -\sin 2\phi & 0 \\ 0 & \sin 2\phi & \cos 2\phi & 0 \\ 0 & 0 & 0 & 1 \end{bmatrix}. \qquad (3.107)$$

Every Stokes vector and Mueller matrix are associated with a specific reference plane and coordinates. The first term on the right-hand side of VRTE [Eq. (3.106)] describes the change in the specific intensity vector over the distance ds caused by extinction and dichroism (deattenuation), the second term describes the contribution of light illuminating a small volume element centered at $\vec{r}$ from all incident directions and scattered into the chosen direction.

For real systems, the form of VRTE tends to be rather complex and often intractable. Therefore, a wide range of analytical and numerical techniques have been developed to solve the VRTE. Because of important property of the normalized phase matrix, Eq. (3.107), being dependent on the difference of the azimuthal angles of the scattering and incident directions rather than on their specific values, an efficient analytical treatment of the azimuthal dependence of the multiply scattered light, using a Fourier decomposition of the VRTE, is possible. The following techniques and their combinations can be used to solve VRTE: transfer matrix method, the singular eigenfunction method, the perturbation method, the small-angle approximation, the adding-doubling method, the matrix operator method, the invariant embedding method, and the Monte Carlo method.

When the medium is illuminated by unpolarized light and/or only the intensity of multiply scattered light needs to be computed, the VRTE can be replaced by its approximate scalar counterpart. In that case, in Eq. (3.106), the Stokes vector is replaced by its first element (i.e., radiance) [see Eq. (3.95)] and the normalized phase matrix by its (1,1) element [i.e., the phase function, $p(\vec{s},\vec{s}')$ which for scattering symmetric relative to the direction of the incident wave is described by Eqs. (3.21), (3.27), (3.37) or (3.38)].

The results of Monte Carlo simulations for polarized light propagation within the multiple scattering media with parameters close to that of tissues are shown in Fig. 3.28 [5]. These calculations well demonstrate that polarization properties of tissues could be dramatically transformed for the multiple scattering conditions. For systems of small spherical particles, the scattering matrix element M_{11}, which refers to the total scattering intensity, shows a significant scattered light redistribution from the mode of isotropic scattering characteristic to single scattering to more intensive scattering mostly in the backward direction as the multiplicity of scattering going up with the increase of diameter of the spherical system filled up by the particles from 1 to 20 mm. The polarization ability of the system originated by Rayleigh (single dipole) scattering (see Fig. 3.27a,b) and expressed in terms of the element M_{12}, which refers to a degree of linear polarization of the scattered light, goes down at scattering multiplicity increase. The 100%-polarization efficiency at the scattering angle $\theta = 90°$ at single scattering mode is reduced significantly, to ~20%. For a large particle system, its transfer from the single to the multiple scattering mode by changing diameter of the system from 0.002 to 2 mm change angular dependences of the elements M_{11} and M_{12} more dramatically than for small particles. As multiplicity of scattering increase a strong forward scattering transfers to a strong backward scattering with the shape more or less similar to the scattering by small particles, however the polarization ability at $\theta = 90°$ decreased from ~80% to a few percents only.

The Mueller matrix for the backscattering geometry was obtained by solving a radiative transfer equation with appropriate boundary conditions. Analysis of this matrix structure showed that its form coincides with the single scattering matrix for optically active spherical scatteres. Thus, different tissues or tissues in pathological or normal functional states should display different responses to the probing with linearly and circularly polarized light. This effect can be employed both in optical medical tomography and for determining optical and spectroscopic parameters of tissues.

The depolarization length in tissues should be close to the mean transport path length l_{tr} of a photon [see Eq. (3.43)], because this length characterizes the distance within which the direction of light propagation and, consequently, the polarization plane of linearly polarized light become totally random after many sequential scattering events (see Fig.3.14).

Since the length l_{tr} is determined by the parameter g characterizing the anisotropy of scattering, the depolarization length should also substantially depend on this parameter. Whole blood is characterized by a considerable depolarization length (around 4 mm) at λ = 633 nm, which is indicative of the dependence on the parameter g, whose value for blood exceeds the values of this parameter for tissues of many other types and can be estimated as 0.982–0.999.

In contrast to depolarization, the attenuation of collimated light is determined by the total attenuation coefficient μ_t [see Eq. (3.18)]. For many tissues, μ_t is much greater than $(\mu_a + \mu_s')$. Therefore, in certain situations, it is impossible to detect pure ballistic photons (photons that do not experience scattering), but forward scattered photons retain their initial polarization and can be used for imaging purpose [5, 9, 10, 71-77]. There was experimentally demonstrated that laser radiation retains linear polarization on the level of $P_L \leq 0.1$ within $2.5l_{tr}$. Specifically, for skin irradiated in the red and NIR ranges, $\mu_a \cong 0.4$ cm^{-1}, $\mu_s' \cong 20$ cm^{-1}, and $l_{tr} \cong 0.48$ mm. Consequently, light propagating in skin can retain linear polarization within the length of about 1.2 mm. Such an optical path in a tissue corresponds to a delay time on the order of 5.3 ps, which provides an opportunity to produce polarization images of macro-inhomogeneities in a tissue with a spatial resolution equivalent to the spatial resolution that can be achieved with the selection of photons by means of more sophisticated time-resolved techniques. In addition, polarization imaging makes it possible to eliminate specular reflection from the surface of a tissue which allows one to apply this technique for the imaging of microvessels in facile skin. Polarization images can see skin subsurface textural changes and allows one to erase melanin from image.

The polarization imaging is a prospective direction in tissue optics [5, 9, 10, 71-77]. The registration of two-dimensional polarization patterns for the backscattering of a polarized incident narrow laser beam is the basis for this technique. The major informative images can be received using the backscattering Mueller matrix approach. To determine each of the 16 experimental matrix elements, a total of 16 images should be taken at various combinations of input and output polarization states. Spatially-resolved reflectance and optical coherence tomography (OCT) imaging techniques are well combined with polarization method.

3.6 Refractive index and controlling of light interaction with tissues

Index of refraction of tissue compounds is of great importance for light tissue interaction [5, 9]. Most of tissues have refractive indices for visible light in the range of 1.335–1.620 (e.g. 1.55 for the stratum corneum, 1.620 for the enamel, and 1.386 at the lens surface). In the simplest model, the mean refractive index $\overline{n}$ of a tissue can be presented as the weighted

sum of refractive indices of the scattering center material n_s and the ground matter n_0:

$$\bar{n} = f_s n_s + (1 - f_s) n_0, \qquad (3.108)$$

where f_s is the volume fraction of the scatterers.

The ratio $n_s/n_0 \equiv m$ determines the scattering coefficient. For example, in a simple monodisperse model of scattering dielectric spheres reduced scattering coefficient μ_s' is defined by Eq. (3.44). It follows from Eq. (3.44) that even a 5% change in the refractive index of the ground matter ($n_0 = 1.35 \rightarrow 1.42$), when that of the scattering centers is $n_s = 1.47$, will cause a 7-fold decrease of μ_s'. Therefore, matching of refractive index of the scatterers and ground material allows for considerable reduction of tissue scattering. This phenomenon is very useful for improvement of facilities of optical tomography and for getting more precise spectroscopic information from the depth of a tissue [5, 9, 78-91].

Optical parameters of a tissue, in particular refractive index, are known to depend on water content. In the visible and NIR wavelength range the following formula can be used to evaluate water index of refraction as a major tissue component (λ in nm) [5]:

$$n_{H_2O} = 1.3199 + \frac{6878}{\lambda^2} - \frac{1.132\times10^9}{\lambda^4} + \frac{1.11\times10^{14}}{\lambda^6}. \qquad (3.109)$$

For different constituents of a biological cell indices of refraction in the NIR can be evaluated as: extracellular fluid – $\bar{n}$ = 1.35 – 1.36, cytoplasm – 1.360 – 1.375, cell membrane – 1.46, nucleus – 1.38 – 1.41, mitochondria and other organelles – 1.38 – 1.41, melanin granules – 1.6 – 1.7. Scattering arises from mismatch in refractive index of the components that make up the cell. For tissues when cells are surrounded by other cells or tissue structures of similar index certain organelles become the important scatterers. For instance, the nucleus is significant scatterer because it is often the largest organelle in the cell and its size increases relative to the rest of the cell throughout neoplastic progression. Mitochondria (500–1500 nm in diameter), lysosomes (500 nm), and peroxisomes (500 nm) are very important scatterers whose size relative to the wavelength of light suggests that they must give a significant include in the backscattering. Melanin granule, traditionally thought of as an absorber, must be considered an important scatterer because of its size and high refractive index. Structures consisting of membrane layers such as the endoplasmic reticulum or Golgi apparatus may prove significant because they contain index fluctuations of high spatial frequency and amplitude. Besides cell components, tissue fibrous structures, such as collagen and elastin fibers, must be considered as important scatterers.

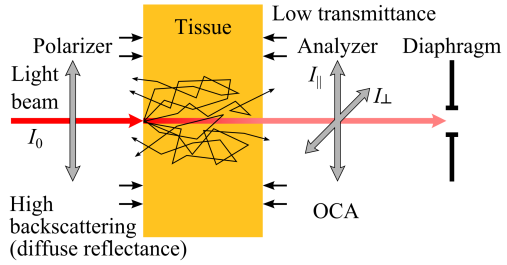
Index of refraction of a number of tissues at 633 nm is in the range from the lowest 1.368 for liver to the largest 1.455 for fatty tissue with other tissues between, such as 1.380 for lungs, 1.400 for blood and spleen, 1.410 for muscular tissue, and 1.418 for kidney. There is a tendency to refraction decrease with the wavelength from 390 to 700 nm, in particular, for bovine muscle – from 1.42 to 1.39.

In terahertz range, 0.5 – 2.5 THz, mean index of refraction of water, the main component of soft tissues, is equal to: $n_W \cong 2.2$ [92, 93]. For the soft tissues which are well supplied by water, such as muscle and skin (dermis), $n \cong 2.1$, for more dry epidermis $n \cong 2.0$; for a soft tissue with a less water content, such as adipose, $n \cong 1.65$. For nail which is a hard tissue with comparably low water content and lack of the mineral component, $n \cong 1.8$. For all other hard tissues with the lower content of water index of refraction is higher than for water due to inclusion of mineral tissue component, for tooth dentin $n \cong 2.4$, for bone $n \cong 2.5$, and for tooth enamel $n \cong 3.1$.

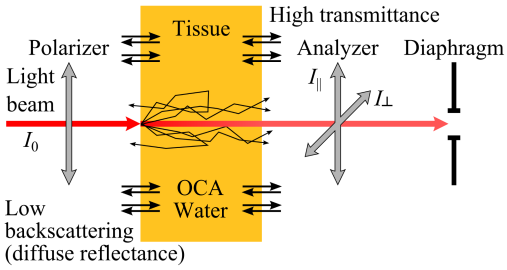
The scattering coefficient (μ_s) and scattering anisotropy factor (g) of a tissue are dependent on refractive index mismatch – relative index of refraction m [see Eqs. (3.25), (3.33), and (3.44)]. The index mismatch exists between cellular tissue components, such as cell membrane, cytoplasm, cell nucleus and other organelles, melanin granules, and the extracellular fluid. For fibrous (connective) tissue, index mismatch of interstitial medium and long strands of scleroprotein (collagen–, elastin–, or reticulin–forming fibers) is important. The scattering particles themselves (organelles, protein fibrils, membranes and protein globules) exhibit a higher density of proteins and lipids in comparison with the ground substance and, thus, a greater index of refraction (n_s = 1.39–1.47). The refractive index of the interstitial liquid, as well as human blood plasma, is approximately 1.33–1.35, depending on the wavelength. The main scatterers in blood are red blood cells (RBCs). A hemoglobin (Hb) concentration of 32 g/dl represents a typical Hb concentration within a human RBC, and the refractive index of the solution is approximately 1.42. For human whole blood, depending on the wavelength, the index is approximately 1.36–1.40.

The optical immersion technique is based on the impregnation of a tissue by a biocompatible chemical agent, which may have hyperosmotic properties [5, 9, 78-91, 93]. The OCAs frequently used are monosaccharides, such as glucose, dextrose, fructose; polysaccharides made of many glucose molecules – dextrans; sugar alcohols (polyols) – glycerol, mannitol and sorbitol; alcohol – 1,3-butanediol; propylene glycol, polypropylene glycol, polyethylene glycol, 1,4-butanediol and their combinations, such as combined lipophilic polypropylene glycol-based polymers and hydrophilic polyethylene glycol-based polymers; x-ray contrasting agents (verografin, trazograph, hypaque, omnipaque), etc.

There are a several main mechanisms of light scattering reduction induced by an OCA: 1) dehydration of tissue constituents; 2) partial replacement of the interstitial fluid by the immersion substance; 3) structural modification (packing); and 4) dissociation of collagen. The first and the third mechanisms are characteristic for hyperosmotic agents. For fibrous tissue similar to sclera, *dura mater*, dermis, the second mechanism could be prevalent for many of tested chemical agents for which molecule size is much less than the mean cross-section of interfibrillar space. Both the first and the second processes mostly cause matching of the refractive indices of the tissue scatterers (cell constituents, collagen and elastin fibers) and the cytoplasm and/or interstitial fluid. The refractive index matching is manifested in the reduction of the scattering coefficient ($\mu_s \to 0$) and increase of single scattering directness ($g \to 1$) (see Fig. 3.12). For fibrous tissues such as skin dermis, eye sclera, *dura mater*, tendon, decrease of reduced scattering coefficient $\mu'_s = (1-g)\mu_s$ can be significant.



a



b

Fig. 3.29 Schematic representation of diffusion of the immersion optical clearing agent (OCA) into and water out of tissue specimen with light increased transmittance (at collinear Polarizer and Analyzer) and decreased scattering due to optical immersion clearing; (a) is the initial specimen state before optical clearing, (b) is the final stage when it became transparent; input light beam is linear polarized by a Polarizer, the output beam is detected being processed by linear polarization Analyzer for two orthogonal polarization states – one in parallel with the polarization of the incident beam $I_{||}$ and another in perpendicular state $I_\perp$; Diaphragm in the far field of 1-1.5 mm in diameter serves for averaging of speckle structures for coherent light illumination or for detection of collimated light transmittance.

Structural modification is manifested as tissue shrinkage, it causes the near-order spatial correlation of scatterers (see Fig. 3.26) and, as a result, the increased constructive interference of the elementary scattered fields in the forward direction and destructive interference in the perpendicular direction of the incident light that may significantly increase tissue transmittance even at residual refractive index mismatch.

For some tissues and for the specific pH of applied OCA, tissue swelling may take place that could be considered as a competitive process in providing tissue optical clearing. The optical clearing process in collagen-based tissues may involve a change in the supramolecular structure. Collagen reversible solubility in sugars and sugar alcohols may take place. Agent-induced destabilization of collagen structures may lead to an additional reduction of optical scattering in tissue owing to less size of the main scatterers.

The osmotic pressure is a driving force in the generation of fluid flows and controlling intensities of these flows, providing a several mechanisms of optical clearing; however, rather strong osmotic pressure may destroy tissue structure. This is a major physicochemical mechanism of OCA toxicity.

For propagation of polarized light in fibrous tissue, it was shown that at a reduction of scattering, the degree of transmitted linearly polarized light significantly improves. Schematically such experiment is shown in Fig. 3.29. As far as the tissue is immersed, the number of scattering events decreases and the residual polarization degree of transmitted linearly polarized light increases. As a result, the kinetics of the average transmittance and degree of polarization of the tissue are correlated. Compare kinetics of clearing curves for linearly polarized component of transmitted intensity $I_{||}$ and the total transmitted intensity I_T in Fig. 3.30. OCA-induced optical clearing leads to an increase in the length of depolarization of a number of tissues. Figure 3.30 also demonstrates the reversibility of tissue clearing by successive OCA and physiological solution application.

As the spatially coherent laser beam was used in this experiment speckle pattern transformation accompanied optical clearing effects (see inserted far-field speckle patters in Fig. 3.30) [5]. Transmitted intensities I_T, $I_{||}$, and $I_\perp$ were measured as mean speckle intensities averaged over the scanning trace (1.5 mm) in the paraxial region. It is well seen that the speckle patterns are transferred from small-size and more or less homogeneously distributed speckles, characteristic for multiple scattering, to big-size inhomogeneously distributed speckles with a big portion of ballistic photons in the central part of the pattern, which is due to low-scattering regime.

As other two examples of *in vitro* studies of optical clearing in the visible range, cerebral membrane (*dura mater*) and skin dermis could be presented. In the course of clearing during 20 min, the reduced scattering

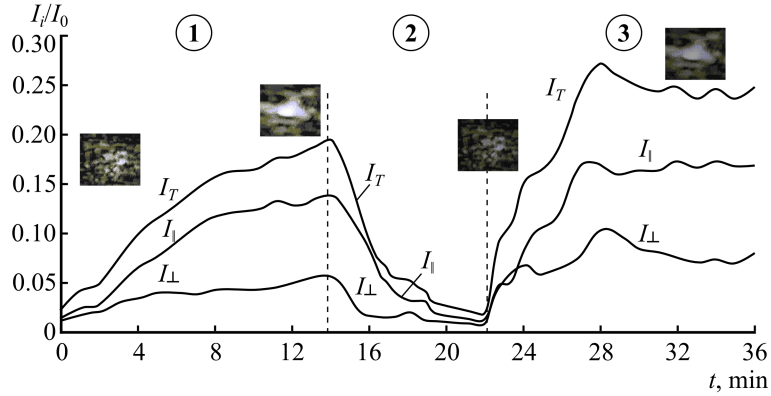


Fig. 3.30 The time-dependent transmittances (I_i/I_0) of the human sclera specimen (d = 0.4 mm) measured with a diaphragm at λ = 633 nm for linear polarization of the incident laser beam I_0; $I_i = I_{||}$, $I_\perp$ are two orthogonal polarization components of the transmitted light; $I_{||}$ in parallel to the polarization of the incident beam and $I_\perp$ – in perpendicular; $I_T = I_{||} + I_\perp$; the subsequent measurements for the specimen kept at first in 60%-trazograph OCA solution, zone (1); in physiological solution (0.9% NaCl), zone (2), and again in the OCA solution, zone (3); inserts show speckle patterns in the transmitted field before and after optical clearing without polarization filtration [5].

coefficient μ'_s of *dura mater* decreases up to 40% (aqueous mannitol solution, 0.16 g/ml, n = 1.357). Application of anhydrous glycerol (n = 1.47) during 20 min to skin dermis decreases μ'_s of skin up to 75%. Differences in the degree of tissue clearing can be explained by differences in refractive indices of the used OCAs, their osmolarity and initial state of tissue turbidity. The swelling of *dura mater* samples was observed, whereas skin shrinkage during the clearing.

Not only soft but also hard tissues could be effectively cleared, which opens the way for the development of the least-invasive techniques for laser diagnostics and therapy of brain and other tissues hidden under bone, cartilage or tendons. For example, optical immersion clearing of the cranial bone under action of anhydrous glycerol allows for decreasing μ'_s of superficial tissue layers in an hour by approximately 25% for the wavelength range 1400–2000 nm. In this case, the main role in the clearing process plays the diffusion of OCA into the interstitial space, owing to the bone-specific structure having a rather high porosity.

The multiple scattering is a detrimental factor that limits optical coherence tomography (OCT) imaging performances: imaging resolution, depth and localization. To improve the imaging capabilities, the multiple scattering of tissue and blood must be reduced. The immersion technique at application of biocompatible agents is a prospective technique for OCT, because very easily the depth of OCT images and their contrast can be essentially improved at immersion. The OCT measures reflectance, $R(z)$, from the tissue versus axial ranging distance, or depth, z. The relationship between $R(z)$ and μ_t can be approximately by [88]

$$R(z) = I_0 \alpha(z) exp(-\mu_t z), \tag{3.110}$$

where I_0 is the optical power launched into the tissue sample and $\alpha(z)$ is the reflectivity of the sample at the depth z; $\alpha(z)$ is linked to the local refractive index and the backscattering property of the sample. If $\alpha(z)$ is a constant, μ_t can be obtained theoretically from the reflectance measurements at two different depths, z_1 and z_2:

$$\mu_t = \frac{1}{(\Delta z)} ln\left[\frac{R(z_1)}{R(z_2)}\right], \tag{3.111}$$

where $\Delta z = |z_1 - z_2|$.

Optical clearing (enhancement of transmittance) ΔT_{OCT} by an agent application can be estimated using the following expression

$$\Delta T_{OCT} = \frac{R_a - R_s}{R_s} \times 100\%, \tag{3.112}$$

where R_a is the reflectance from the backward surface of the sample impregnated by an agent, and R_s is that with a control sample.

Blood immerses or goes through practically all tissues. It is a highly scattering biological liquid with a strong anisotropy of scattering. Therefore, blood optical clearing is of great importance [5, 78-80, 88]. The refractive-index mismatch between erythrocyte cytoplasm and blood plasma, as well as specific size and structure, cause the scattering properties of blood. The refractive index of erythrocyte cytoplasm is defined mostly by hemoglobin concentration. The volume and

shape of a single erythrocyte are defined by blood plasma osmolarity. Blood scattering also depends on aggregation or disaggregation capability of RBCs. Upon introduction of OCAs into blood, the refractive index of the blood plasma increases and becomes comparable with that of RBCs. For example, in whole blood diluted to twice of its volume by saline with the addition of 6.5% glycerol, the total attenuation coefficient $\mu_t = \mu_a + \mu_s$ was reduced from 42 to 20 cm^{-1}, and the optical penetration at 820 nm was correspondingly increased to 117% in terms of ΔT_{OCT}. For the other agents tested (glucose, dextrans, propylene glycol and trazograph), the enhancement of penetration ΔT_{OCT} = 20–150%.

There is also the possibility of applying as an immersion agent, a small amount of hemoglobin, which could be released owing to local hemolysis of RBCs within the vessel area close to endoscopic optical probe. A 30–40% reduction of the scattering coefficient of blood in the spectral range from 400 to 1000 nm, with an increase in the local RBC hemolysis up to 20% is expected. The optical clearing of blood is defined not only by refractive-index matching phenomenon, but also by changes in the size of RBCs and in their aggregation ability when chemicals are added.

It is known that at *in vivo* application of the designed optical immersion technology, additional factors such as metabolic reaction of living tissue on clearing agent application, the specificity of tissue functioning and its physiological temperature can significantly change kinetic characteristics and the magnitude of the clearing effect. In a living tissue, the relative refractive index is a function of tissue physiological or pathological state. Depending on the specificity of the tissue state, the refractive index of the scatterers and/or the background may be changed (increased or decreased), and therefore light scattering may correspondingly increase or decrease. For example, the μ_s' calculated at a wavelength of 700 nm on the basis of *in vivo* spectral reflectance measurements for rabbit eye sclera (Fig. 3.31) [5] and *in vitro* spectral transmittance measurements for human sclera at administration of 40%-glucose solution showed the clearing degree for *in vivo* study of 1.7 fold – that is, less than for *in vitro* (~2.7 fold). Less efficiency for *in vivo* conditions may be explained by glucose washing out from the area of administration and physiological reaction of the living tissue.

In the terahertz range, where scattering is negligible and transport of radiation in tissues mostly depends on tissue absorption properties, in particular by tissue water absorption which absorption coefficient is rather high, $\mu_a \cong 100 - 300 cm^{-1}$. For normal muscle tissue absorption coefficient is also high, $\mu_a \cong 120 - 160 cm^{-1}$, however when tissue is dehydrated by application of a hyperosmotic agent absorption decreases up to 30–40% and tissue becomes more transparent [93].

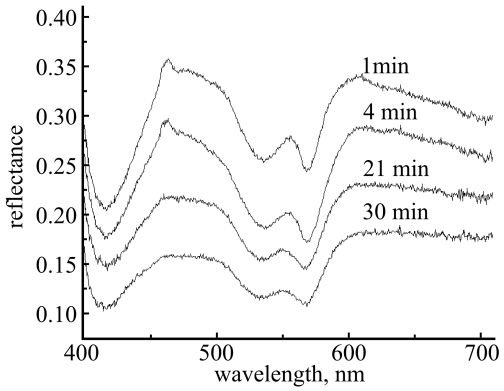


Fig. 3.31 Reflectance spectra for the rabbit eye sclera measured concurrently with administration of 40% -glucose solution in 1, 4, 21, and 30 min after a few drops of the solution into the eye [5].

Topical application of OCAs to skin is less efficient because of protective properties of the stratum corneum (SC), thus different chemical and physical enhancers of skin permeability are used [5, 9, 78-91]. The typical chemical enhancers are: ethanol, propylene glycol, dimethylsulfoxide (DMSO), linoleic and oleic acids, azone and thiazone. To reduce the barrier function of skin epidermis, physical methods such as tape stripping, microdermabrasion, low intensive and high intensive laser irradiation of skin surface, iontophoresis, ultrasound and photomechanical (shock) waves, needle-free injection, photothermal and mechanical micro-perforation, or laser fractional micro-damaging were proposed.

Acknowledgments

I am thankful to Valery Zakharov for his idea to write such a paper, to all my colleagues from SSU and IPMC RAS for fruitful collaboration, and to Alexander Kalyanov for help in preparation of illustrations. This work was supported by Russian Presidential grant NSh703.2014.2, the Government of the Russian Federation grant 14.Z50.31.0004, and the Ministry of Education and Science of the Russian Federation.

Dendritic crystallogram images classification

Rustam A. Paringer[1,2]*, Alexander V. Kupriyanov[1,2], Nataly Y. Ilyasova[1,2]
[1] Samara State Aerospace University, 34 Moskovskoe shosse, Samara, 443086, Russian Federation
[2] Image Processing Systems Institute of the Russian Academy of Sciences, 151 Molodogvardejskaya st., Samara, 443001, Russian Federation

e-mail: RusParinger@gmail.com

Abstract. A computer classification system of dendritic crystallogram images is presented in this paper. To improve the quality of classification we use an algorithm for the informative features formation, using methods of discriminant analysis. The method for receiving an informativeness estimation was used. As basic features are seven geometric characteristic was calculated. The research confirming the efficiency of the formed features for classification of dendritic crystallogramms images was conducted by means of classification by support vector machine. Of these, was selected most informative basic five features and one new feature was formed. The error classification decreased from 0.081 to 0.061. The algorithm possesses a sufficient level of universality and may be applied to increase the informativeness of any feature set. © 2015 Samara State Aerospace University (SSAU).

Keywords: Discriminant analysis, support vector machine, feature informativeness

Paper #2470 received 2015.05.30; revised manuscript received 2015.06.18; accepted for publication 2015.06.20; published online 2015.06.30.

References

1. R. A. Paringer, and A. V. Kupriyanov, "Methods For Estimating Geometric Parameters of The Dendrite's Crystallogramms," Proceedings of 8th Open German-Russian Workshop "Pattern Recognition and Image Understanding", 226-229 (2011).
2. R. A. Paringer, "Separation and Analysis of Dendrites on Images of Diagnostic Crystallograms of Biological Liquids," Biomedsistems-2012, 105-108 (2012).
3. N. Y. Ilyasova, A. V. Kupriyanov, and R. A. Paringer, "Formation features for improving the quality of medical diagnosis based on the discriminant analysis methods," Computer Optics 38(4), 851-856 (2014).
4. R. A. Paringer, and A. V. Kupriyanov, "The Method for Effective Clustering the Dendrite Crystallogram Images," Electronic on-site Proceedings of 9th Open German-Russian Workshop on Pattern Recognition and Image Understanding (OGRW 2014) (2014).
5. R. A. Paringer, and A. V. Kupriyanov, "Research Methods for Classification of the Crystallogramms Images," Proceedings of the 12th international conference "PRIP'2014", 231-234 (2014).
6. K. Fukunaga, Introduction to the Image Discrimination Statistical Theory, Nauka, Moscow (1979) [in Russian].

1 Introduction

The analysis of medical crystallogram images is an important part of medical diagnostics. Medical crystallograms are the structures formed at crystallization of salts as a result of drying the biological liquids (tears, blood, saliva, etc.). Computerization of the crystallogram image processing will enable to improve the quality of diagnostics and will reduce its time expenditures. The use of different devices and techniques of crystallograms imaging shall result to the fact that the structures density in crystallogram images may essentially differ. Therefore, in order to improve the overall quality of diagnostics it is offered first to estimate the scale of the crystallogram image shooting. The features that evaluate geometric characteristics of dendritic crystallograms have been developed [1, 2]. To evaluate the efficiency of the developed features, for a classification problem of the

presented class of on-scale images, a respective algorithm has been developed, based on the discriminant analysis algorithm [3]. The developed algorithm also enables to create spaces of new features ensuring the best possible separation in the definite classification problem [4, 5]. To evaluate the partibility of classes the discriminant analysis criteria are used [6]. Thus, for a well-defined set of features and the strictly defined image classes, a new space has been formed in which the image classes being of interest were divided in the best way. The effectiveness of the used features may be also evaluated by using the proposed approach.

2 Methodology

Features. Let us consider a dendrite model shown in Fig. 1. A, B, C, D – the "tops" of dendritic processes, E, F, G – the "roots" of dendritic processes, EF, FG – distances between processes, AE, BE, CF, DG – dendrites processes.

The algorithm consists of the following sequence of actions: thresholding, median filtering, skeletonization, identification of key elements and construction of a "map of dendrites."

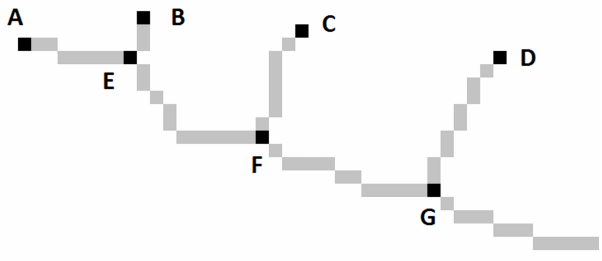


Fig. 1 Dendrite model.

The key elements include the "tops" and the "roots" of dendritic processes. The previously developed set of features [1, 2] has been added with four new features. The following features are calculated while processing:

- Density of the original image C_{ps}: is calculated after the median filtering as a ratio of the number of pixels in an object to the total number of pixels in the image.
- Thickness of dendrites C_t: is calculated as the number of iterations of the skeletonization algorithm.
- The other features shall be calculated according the "map of dendrites."
- The average distance between processes C_l: is the ratio of the sum of all distances between processes to the total number of processes. For Fig. 1 – $C_l = \frac{EF+FG}{4}$.
- The density of skeletonized dendrites C_{pd}: the ratio of the sum of lengths of all processes and all distances between processes to the total number of pixels in the image.
- The growth rate C_g: the ratio of the sum of lengths of all processes to the sum of distances between processes. For Fig. 1 – $C_g = \frac{\mathrm{AE+BE+CF+DG}}{\mathrm{EF+FG}}$.
- The average angle C_a: the ratio of the sum of angles of all processes to the total number of processes. For Fig. 1 – a process angle CF equals to an angle CFE in a triangle CFE.
- The symmetry factor C_s: $\mathrm{C_s}$: the ratio of the number of the "tops" of dendritic processes to the number of the "roots" of dendritic processes. For Fig. 1 – $C_s = \frac{4}{3}$.

Algorithm of forming new features. Suppose we are given the sampling of n items divided into g classes and containing the proper p features. In discriminant analysis the measure of the sampling effectiveness are the partibility criteria which are calculated by the following formulas:

$$J_1 = tr(\boldsymbol{T^{-1}B}),$$

where $\boldsymbol{T} = \boldsymbol{B} + \boldsymbol{W}$, $\boldsymbol{B}$ – is the among-groups scattering matrix, the elements of which are calculated by the formula:

$$b_{ij} = \sum_{k=1}^{g} n_k(\bar{x}_{ik} - \bar{x}_i)\left(\bar{x}_{jk} - \bar{x}_j\right), i, j = \overline{1,p},$$

$\boldsymbol{W}$ – is the intragroup scattering matrix, the elements of which are calculated by the formula:

$$w_{ij} = \sum_{k=1}^{g} \sum_{m=1}^{n_k} (x_{ikm} - \bar{x}_{ik})\left(x_{jkm} - \bar{x}_{jk}\right), i, j = \overline{1,p},$$

where x_{ikm} – is the value of the i feature for the m element in the class k, $\bar{x}_{ik} = (1/n_k)\sum_{m=1}^{n_k} \bar{x}_{ikm}$ – the mean value of the i feature in the class k, $\bar{x}_i = (1/n)\sum_{k=1}^{g}(n_k \bar{x}_{ik})$ – the mean value of the i feature in all classes, n_k – the number of elements in the class k.

The more the criterion value, the more the partibility of classes.

Suppose $x = \left[x_1, x_2 \ldots x_p\right]^T$ – is the original feature vector. Let us consider the algorithm of forming new features of y= $\left[y_1, y_2 \ldots y_p\right]^T$.

1. For the matrix $T^{-1}B$ let us define the values of eigen vectors $\boldsymbol{v_i}, i = \overline{1,p}$.
2. Let us define the vector of standardized coefficients $\boldsymbol{\beta_i} = \left[\beta_0, \beta_1 \ldots \beta_p\right]^T, i = \overline{1,m}$, where the elements $\beta_i, i = \overline{0,p}$ are computed as follows:

$$\beta_0 = -\sum_{i=1}^{p} \beta_i \overline{x_i}, \beta_i = v_i\sqrt{n-g}, i = \overline{1,p}.$$

3. Let us compute the elements of the vector of new features by the formula:

$$y_i = \beta_0 + \beta_1 x_1 + \ldots + \beta_p x_p, i = \overline{1,m}.$$

The exhaustive algorithm forms a group of new features using the discriminant analysis algorithm, thus

keeping the value of the intragroup criterion of features partibility. In order to form new features, all possible combinations of the original features are used. Besides, to compute the criteria, all possible combinations of the formed features are also used. The group of the formed features is to be selected, based on the value of the intragroup partibility criterion. The exhaustive search of all possible combinations of features guarantees the best division in the definite classification problem [3].

3 Results

A feature vector is calculated for each image. The classification error value is evaluated, based on the obtained data. Then, the basic features are subjected to the discriminant analysis procedure, and a set of new features is formed. After that, the classification error value is evaluated according to the formed features set. The classification error estimate was carried out by means of a support vector machine. The synthesis of a classifier was conducted by using the U-method. In order to implement the U-method, we have used the one-object elimination method that lies in the fact that all objects are included in a learning sample. By excluding one object, the classifier is synthesized by the remaining objects, and a test sample is formed by an unused object. This procedure is repeated for all sample objects, and the number of incorrectly classified objects is calculated. The classification error is defined as the ratio of the number of incorrectly classified objects to the total number of objects in the whole sample [6].

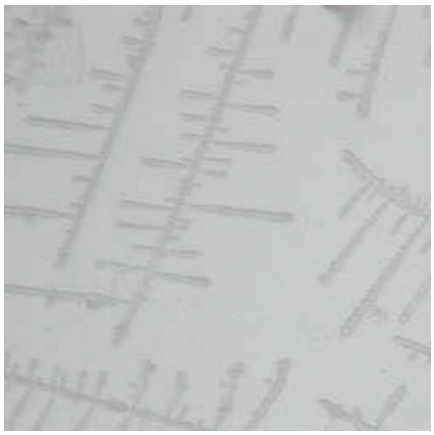
The basic data for the experiments is a set of diagnostic crystallogram images with a resolution of 256 by 256 pixels and consisting of 256 half-tone color tones. The set of basic data was divided into two classes, based on an increase value, which was used while shooting. The first class includes 76 images of dendritic crystallograms obtained at 100 times magnification (an example is shown in Fig. 2(a)). The second class includes 72 images of dendritic crystallograms obtained at 200 times magnification (an example is shown in Fig. 2(b)).

As a result of the experiment a new features was formed by multiplying basic features on vectors of standardized coefficients ($\boldsymbol{\beta}$). "The Formed Feature 1" has been formed from five basic features. The features "Density of the Original Image C_{ps}" and "Thickness of Dendrites C_t" were not used for the forming. "The Formed Feature 2" was formed from all seven basic features and added for the comparison. The value of partibility criteria for all characteristics are presented in Table 1.

From the table above it can be concluded that the feature "Thickness of Dendrites C_t" was not used, thus, as judged by the value of the partibility criterion, it does not contain any meaningful information for classification. The feature "Density of the Original Image C_{ps}" was not used to form a new feature, since it significantly correlates with many other features that are used for the formation (Table 2). Classification error with using all seven basic features is 0.081, for "The Formed Feature 1" 0.061 and for "The Formed Feature 2" same 0.061.



(a)



(b)

Fig. 2 Image of dendritic crystallograms (a) at 100 times magnification, (b) at 200 times magnification.

Table 1 The value of features partibility criteria and classification error.

Feature	J_1	**Classification error**
Density of the original image (C_{ps})	0,38397	0.081
Thickness of dendrites (C_t)	1,6E-07	
The average distance between processes (C_l)	0,64174	
Growth rate (C_{pd})	0,03821	
Density of skeletonized dendrites (C_g)	0,36071	
Angle factor (C_a)	0,23939	
Symmetry factor (C_s)	0,00854	
The Formed Feature 1	0,81747	0.061
The Formed Feature 2	0,81798	0.061

Despite the fact that the value of the partibility criterion "The Formed Feature 1" is little less than "The Formed Feature 2", their classification error values are

equal. Hence, it follows that the proposed algorithm of forming features does not only allow to evaluate the effectiveness of original features, but also allows to create new, more effective, criteria to solve the proper classification problem.

Table 2 Correlation matrix of the original features.

	C_{ps}	C_t	C_l	C_{pd}	C_g	C_a	C_s
C_{ps}	1,00	-0,02	-0,63	-0,33	0,78	-0,24	-0,45
C_t	-0,02	1,00	0,08	0,11	0,46	0,05	0,13
C_l	-0,63	0,08	1,00	-0,12	-0,55	0,44	0,12
C_{pd}	-0,33	0,11	-0,12	1,00	-0,31	-0,04	0,66
C_g	0,78	0,46	-0,55	-0,31	1,00	-0,12	-0,39
C_a	-0,24	0,05	0,44	-0,04	-0,12	1,00	-0,25
C_s	-0,45	0,13	0,12	0,66	-0,39	-0,25	1,00

4 Conclusion.

The algorithm of forming the space of efficient features based on the discriminant analysis was used in the classification problem of images of dendritic crystallograms. The algorithm allows to improve the efficiency of the classification of dendritic crystallograms taken at different magnifications, whereas the classification error of crystallograms is maximum 6.1%.

It is shown that the algorithm allows to evaluate the effectiveness of the used features to solve classification problems and to eliminate the linear dependence between the features. It is also worth pointing out that the more the initial features are used in the algorithm, the more accurate links would be set up between the features. The used algorithm of forming features possesses a sufficient level of universality and may be applied to increase the informativeness of any feature set. Implementation of the algorithm of forming efficient features enables to reduce the classification error.

Acknowledgments

This work was performed with the support of the Ministry of Education and Science of the Russian Federation within the framework of implementation of measures of the Program for Improving the SSAU Competitiveness among the World's Leading Research and Educational Centers for the Period of 2013-2020s; under the RFBR grant (the Russian Foundation for Basic Researches) 14-01-00369-a, 14-07-97040-r_povolzhje_a; within the Basic Research Program ONIT RAN of the Russian Academy of Sciences "Bioinformatics, Advanced Information Technologies and Mathematical Methods in Medicine" 2015.

Zernike phase spatial filter for measuring the aberrations of the optical structures of the eye

Svetlana N. Khonina[1*], Victor V. Kotlyar[2], Dmitriy V. Kirsh[2]

[1] Image Processing Systems Institute of the Russian Academy of Sciences, 151 Molodogvardejskaya st., Samara 443001, Russian Federation

[2] Samara State Aerospace University, 34 Moskovskoe shosse, Samara 443086, Russian Federation

[*] **e-mail:** khonina@smr.ru

Abstract. To measure directly the wavefront aberration coefficients, we propose to use the multi-order diffractive element fitted with the set of Zernike polynomials. Polynomials of lowest degree describe defocusing (ametropy) and astigmatism. Coefficients of highest degree correspond to the spherical aberration of oblique rays that occurs as a consequence of misalignment of the crystalline lens and foveola, as well as deflection at the periphery of the crystalline lens. Multi-order elements allow several tens of expansion coefficients to be measured simultaneously, which will enable to investigate insufficiently known high-order aberrations for the differentiated diagnostics of eye diseases. © 2015 Samara State Aerospace University (SSAU).

Keywords: wavefront aberrations, eye optical system, Zernike polynomials, multi-order diffractive elements, expansion coefficients.

Paper #2468 received 2015.05.29; revised manuscript received 2015.06.23; accepted for publication 2015.06.25; published online 2015.06.30.

References

1. M. S. Smirnov, "Measurement of the wave aberration of the human eye," Biofizika 6, 776–795 (1961).
2. H. C. Howland, and B. Howland, "A subjective method for the measurement of monochromatic aberrations of the eye," J. Opt. Soc. Am. 67(11), 1508–1518 (1977).
3. F. Berny, and S. Slansky, "Wavefront determination resulting from Foucault test as applied to the human eye and visual instruments," Optical Instruments and Techniques, 375–386 (1969).
4. P. Artal, J. Santamaría, and J. Bescós, "Retrieval of the wave aberration of human eyes from actual point-spread function data," J. Opt. Soc. Am. 5(8), 1201–1206 (1988).
5. D. A. Atchison, "Invited review recent advances in measurement of monochromatic aberrations of human eyes," Clin Exp Optom 88(1), 5–27 (2005).
6. A. S. Goncharov et al., "Modal tomography of aberrations of the human eye," Laser Physics, 16(12), 1689–1695 (2006).
7. M. Lombardo, and G. Lombardo, "New methods and techniques for sensing the wave aberrations in human eyes," Clin Exp Optom 92(3), 176–186 (2009).
8. P. Artal, "Optics of the eye and its impact in vision: a tutorial," Advances in Optics and Photonics 6(3), 340–367 (2014).
9. G. Artzner, "Microlens arrays for Shack-Hartmann wavefront sensors," Opt. Eng. 31(6), 1311-1322 (1992).
10. J. Liang et al., "Objective measurement of the WA´s aberration of the human eye with the use of a Hartmann-Shack sensor," J. Opt. Soc. Am. 11, 1949–1957 (1994).
11. American National Standards Institute, Inc. American National Standards for Ophthalmics – Methods for Reporting Optical Aberrations of Eyes. ANSI Z80.28 (2004).
12. International Organization for Standardization (ISO). Ophthalmic Optics and Instruments – Reporting Aberrations of the Human Eye. Geneva, Switzerland (2008).
13. R. A. Applegate et al., "Visual acuity as a function of Zernike mode and level of root mean square error," Optom Vis Sci 80(2), 97–105 (2003).

14. D. L. Golovashkin et al., Computer Design of Diffractive Optics, V. A. Soifer (Ed.), Cambridge Inter. Scien. Pub. Ltd.& Woodhead Pub. Ltd., Cambridge (2012).
15. S. N. Khonina et al., "Experimental selection of spatial Gauss-Laguerre modes," Optical Memory and Neural Networks 9(1), 69–74 (2000).
16. V. V. Koltyar, and S. N. Khonina, "Multi-order diffractive optical elements to process data," Chapter 2 in Perspectives in Engineering Optics, K. Singh, V. K. Rastogi (Eds.), Anita Publications, Delhi, 47–56 (2003).
17. S. N. Khonina et al., "Generation and selection of laser beams represented by a superposition of two angular harmonics," Journal of Modern optics, 51(5), 761–773 (2004).
18. V. V. Kotlyar et al., "Coherent field phase retrieval using a phase Zernike filter," Computer Optics 17, 43–48 (1997).
19. S. N. Khonina et al., "Phase reconstruction using a Zernike decomposition filter," Computer Optics 18, 52–56 (1998).
20. S. N. Khonina, V. V. Kotlyar, and Ya Wang, "Diffractive optical element matched with Zernike basis," Pattern Recognition and Image Analysis 11(2), 442–445 (2001).
21. M. Born, and E. Wolf, Principles of Optics, Pergamon Press, Oxford (1968).

1 Introduction

Wave aberrations of the eye can be measured using various subjective and objective methods. The subjective methods are based on the collection of the patient's visual responses, while the objective methods do not require the cooperation with the patient and are based on the image recording after the double-pass through the ocular lens. Among the methods developed over the years, the following methods can be singled out: the Vernier method – alignment [1], aberroscopy [2], the Foucault knife-edge method [3] and the method for phase retrieval from the retina image [4].

Existing clinical aberrometers provide sufficiently accurate measurements of deflection of the eye's wavefront [5-8]. In this case high-order aberrations are measured to assess the personal deflections of the wavefront, including those related to the professional activity or age-related changes, in order to optimise the optical (with contact or intraocular lenses) or surgical correction of the human eye.

Currently, the most widely used method for the measurement of the eye aberration is the Hartmann-Shack wavefront sensor [9, 10]. The sensor consists of a microlens array optically conjugated to the pupil and a camera located in the focal plane of the microlens array. If a plane wavefront reaches the microlenses then the perfectly regular grid of light spots is formed on the camera. However, if the wavefront is distorted by aberrations, the light spots are located irregularly. The displacement of each spot from the reference position is proportional to the wavefront derivative in each microlens area. Thus, the wavefront is reconstructed from the displacements of the light spots recorded by the Hartmann-Shack sensor, and then the aberrations are calculated.

A common representation of the wavefront is a set of Zernike polynomials, which correspond to different wavefront aberrations [11, 12]. Coefficients for the expansion of the wavefront in orthogonal Zernike polynomials make it possible to determine the root mean square error of the deflection from an ideal wavefront. The coefficients with high absolute value automatically indicate to the aberrations that distort the wavefront in the highest degree and consequently allow to significantly speed up and simplify the analysis of patient's vision [13].

In this paper, we propose to use diffractive optics methods for the direct optical measurement of amplitudes of coefficients for the expansion of the individual visual system wavefront in Zernike polynomials [14].

The diffractive optical elements (DOE) forming simultaneously several laser beam modes in different diffraction orders (so-called multi-order or multi-channel elements) are successfully used as a spatial filters for the analysis of a set of laser beam transverse modes [14-17].

Similar multi-order DOE fitted with the set of Zernike polynomials can be used in the wavefront analysis and reconstruction [18-20].

In this paper, wavefront aberrations are analysed using a phase spatial filter, with orthogonal circular Zernike polynomials used as a basis of the light field expansion. Note that in this case, not the phase field but the complex amplitude is expanded into the Zernike basis, with the intensity generated in the spatial plane of Fourier-spectrum and proportional to the field expansion coefficients. The coefficient modules measured are then used for computing the argument of the light field complex amplitude. We are also concerned with iterative algorithms for computing the Zernike filter phase and the phase of light field complex amplitude.

2 Theoretical bases

There is a complete set of orthogonal functions with angular harmonics in a circle of radius r_0. These are the circular Zernike polynomials [21]:

$$\Psi_{nm}(r,\varphi) = A_n R_n^m(r) exp(im\varphi), \quad (1)$$

where

$$A_n = \sqrt{\frac{n+1}{\pi r_0^2}},$$

$$R_n^m(r) = \sum_{p=0}^{(n-m)/2} \frac{(-1)^p (n-p)! \times}{\times \left[p!\left(\frac{n+m}{2}-p\right)!\left(\frac{n-m}{2}-p\right)!\right]^{-1} \times} \times \left(\frac{r}{r_0}\right)^{n-2p},$$

$R_n^m(r)$ are the radial Zernike polynomials:

$$R_n^{-m}(r) = R_n^m(r), \quad R_n^{\pm 1}(r_0) = 1,$$
$$R_{2k+1}^{2l}(r) = 0, \quad R_{2k}^{2l+1}(r) = 0, \quad |m| \le n, \quad R_0^0(r) = 1,$$

and (r,φ) are polar coordinates.

The expansion of the light field with complex amplitude $E(r,\varphi)$ into a series in terms of the functions in Eq. (1) is given by

$$E(r,\varphi) = \sum_{n=0}^{\infty} \sum_{m=-n}^{n} C_{nm} \Psi_{nm}(r,\varphi), \tag{2}$$

$$\int_0^{r_0} R_n^m(r) R_p^m(r) r\,\mathrm{d}r = \frac{r_0^2}{2(n+1)} \delta_{np},$$

$$C_{nm} = \int_0^{r_0} \int_0^{2\pi} E(r,\varphi) \Psi_{nm}^*(r,\varphi) r\,\mathrm{d}r\,\mathrm{d}\varphi. \tag{3}$$

In the plane of a spatial Fourier-spectrum that may be generated by a spherical lens of focal length f, the light field complex amplitude $F(\rho,\theta)$ takes the form

$$F(\rho,\theta) = \frac{k}{2\pi f} \times \times \int_0^{r_0} \int_0^{2\pi} E(r,\phi) exp\left[-i\frac{k}{f} r\rho\, cos(\phi-\theta)\right] r\mathrm{d}r\mathrm{d}\phi, \tag{4}$$

where $k=2\pi/\lambda$ is the wavenumber of light, λ is the wavelength, and (ρ,θ) are the polar coordinates. Based on Eq. (2), the light field expansion, Eq. (4), in terms of the Zernike polynomials of Eq. (1) is given by

$$F(\rho,\theta) = = \frac{k}{f} \sum_{n=0}^{\infty} \sum_{m=-n}^{n} (-i)^m C_{nm} A_{nm} e^{im\theta} \int_o^{2\pi} R_n^m(r) J_m\left(\frac{k}{f} r\rho\right) r\,\mathrm{d}r. \tag{5}$$

In deriving Eq. (5), we made use of the integral representation of the Bessel functions of the first kind and m-th order:

$$J_m(x) = \frac{i^m}{2\pi} \int_0^{2\pi} exp(-ix\cos t + imt)\,\mathrm{d}t.$$

The integral in Eq. (5) may be taken explicitly [21]:

$$W_{nm}(\rho) = \int_o^{r_0} R_n^m(r) J_m(kf^{-1} r\rho) r\,\mathrm{d}r = = (-1)^{(n-m)/2} r_0^2 \frac{J_{n+1}(kf^{-1} r_0 \rho)}{(kf^{-1} r_0 \rho)}. \tag{6}$$

From Eq. (6), one can see that at $n>0$ the complex amplitude at central points $\rho=0$ is equal to zero:

$$W_{nm}(\rho=0) = \begin{cases} 0, n>0, \\ \frac{r_0^2}{2}, n=0. \end{cases}$$

Hence, at $n > 0$ the intensity distribution in diffraction orders of the Fourier-plane will be circular in structure.

An optical configuration of the spectral Zernike analyser to illustrate the use of a phase Zernike filter in analysis of the wavefront of amplitude $E(r,\varphi)$ is shown in Fig. 1. Similar to the Hartman-Shack wavefront sensor [9, 10], the Zernike filter is mounted directly in the plane of the wavefront to be studied, with a spherical lens L of focal length f placed immediately behind it. A photoreceiver array matched to the computer PC is placed in the rear focal plane of the lens L.

In our formulation of the problem, lens aberrations are not included. We believe they will be substantially less than the analysed aberrations of an eye.

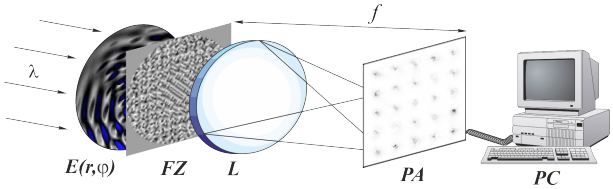


Fig. 1 Optical configuration of the Zernike analyser: ZF is the Zernike filter, L is a spherical lens, PA is a photoreceiver array, and PC is a computer.

3 Design of the phase-only multi-order Zernike filter

In order for the transmission function of the ZF to be phase-only:

$$\tau(r,\varphi) = exp[iS(r,\varphi)] \tag{7}$$

it should be sought for in the form

$$\tau(r,\varphi) = \\ = \sum_{n=0}^{N}\sum_{m=-n}^{n} \Psi^{*}_{nm}(r,\varphi)\times \\ \times exp\left[ikf^{-1}r\rho_{nm}cos(\varphi-\theta_{nm})+\nu_{nm}\right], \quad (8)$$

where (ρ_{nm},φ_{nm}) are the vectors of the carrier spatial frequencies in polar coordinates and ν_{nm} are the free parameters of the task to be fitted in such a manner as to make Eq. (8) an exact equality. Once the light intensity proportional to the squared modulus of the expansion coefficients in Eq. (2),

$$I_{nm} = \left|C_{nm}\right|^2 \quad (9)$$

has been measured at discrete points of the Fourier-plane (see Fig. 1), one must perform additional computation in order to find the light field phase from Eq. (2):

$$Q(r,\varphi) = arg\, E(r,\varphi). \quad (10)$$

To do this, one may use an algorithm similar to the algorithm of Eqs. (3) and (4) and find the phase estimate of light field in the (k+1)-th iteration in the form

$$Q_{k+1}(r,\varphi) = \\ = arg\left\{\sum_{n=0}^{N}\sum_{m=-n}^{n}\sqrt{I_{nm}}\Psi_{nm}(r,\varphi)exp\left[i\nu_{nm}^{(k)}\right]\right\}, \quad (11)$$

where $\nu_{nm}^{(k)}$ are the free parameters in the k-th iteration derived from the equation

$$\nu_{nm}^{(k)} = arg\left\{\int_0^{r_0}\int_0^{2\pi} exp\left[iQ_k(r,\varphi)\right]\Psi^{*}_{nm}(r,\varphi)r\,dr\,d\varphi\right\}, \quad (12)$$

where $Q_k(r,\varphi)$ is the sought-for phase estimate in the k-th iteration.

Since the wavefront aberrations met with in optical systems are described by even functions relative to the azimuth angle φ [21], the wave field $E(r,\varphi)$ may be written as

$$E(r,\varphi) = exp\left\{i\sum_{n=0}^{N}\sum_{m=-n}^{n} B_{nm}R_n^m(r)cos(m\varphi)\right\}. \quad (13)$$

In this connection, instead of the general expansion in Eq. (9) one should use the expansion in terms of the even functions

$$E(r,\varphi) = \sum_{n=0}^{\infty}\sum_{m=-n}^{n} C_{nm}\overline{\Psi}_{nm}(r,\varphi),$$

$$\overline{\Psi}_{nm}(r,\varphi) = \varepsilon_m\sqrt{\frac{n+1}{\pi r_0^2}}R_n^m(r)cos(m\varphi),$$

where $\varepsilon_m = \begin{cases} 2, & m \neq 0, \\ 1, & m = 0. \end{cases}$

For small aberrations, the relation between the expansion coefficients B_{nm} and C_{nm} is linear

$$1 + iB_{00} = \frac{C_{00}}{\sqrt{\pi r_0^2}},\ iB_{nm} = \varepsilon_m\frac{C_{nm}}{\sqrt{\pi r_0^2}}.$$

For arbitrary aberrations, the relation between B_{nm} and C_{nm} is non-linear and on measuring the modules $\left|C_{00}\right|^2$ one has to use the algorithm of Eqs. (11) and (12) in order to derive the phase $Q(r,\varphi)$ of Eq. (10). Then, using Eq. (13) one derives the wave aberration coefficients, B_{mn}.

Note that since $R_0^0(r) = 1$, the Zernike polynomial basis contains the unit as an expansion term, which means that when illuminated by a plane wave of amplitude $E(r,\varphi)$=const, the Zernike filter yields only one non-zero coefficient of the expansion in Eq. (10):

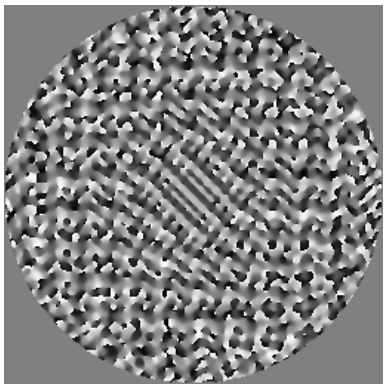
$$\left|C_{00}\right|^2 \neq 0.$$

From Eq. (6) it also follows that the diffraction orders corresponding to the basis functions with different numbers m, but with the same numbers n, will have similar diffraction patterns (circular structures at $n > 0$) in the Fourier-plane:

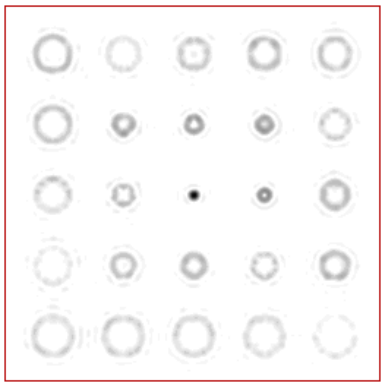
$$\left|W_{nm}(\rho)\right| = r_0^2\frac{\left|J_{n+1}\left(kf^{-1}r_0\rho\right)\right|}{\left(kf^{-1}r_0\rho\right)}.$$

The simulation parameters were as follows: 256 pixels on the radius r and 256 pixels on the angle φ, r_0 = 1 mm, $k = 10^4$ mm^{-1}, f = 100 mm. We designed a 25-channel filter [18] that generates diffraction orders for the basis functions with the numbers (n,m): $m \le 8$ and $n \le 8$, propagated at some angles to the optical axis.

Figure 2 depicts: (a) the half-tone Zernike filter phase (black colour corresponds to the phase value of 0 and white to 2π), (b) 25 diffraction orders generated in the lens frequency plane (negative), and (c) the correspondence between the numbers (n,m) and diffraction orders.



(a)



(b)

(7,1)	(6,6)	(6,4)	(6,2)	(6,0)
(7,3)	(3,1)	(2,2)	(2,0)	(5,5)
(7,5)	(3,3)	(0,0)	(1,1)	(5,3)
(7,7)	(4,0)	(4,2)	(4,4)	(5,1)
(8,0)	(8,2)	(8,4)	(8,6)	(8,8)

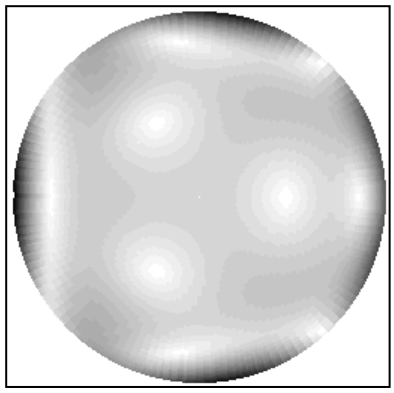
(c)

Fig. 2 (a) The half-tone phase of the Zernike filter, (b) the intensity distribution in the lens focal plane, and (c) the correspondence between the numbers (*n,m*) and diffraction orders.

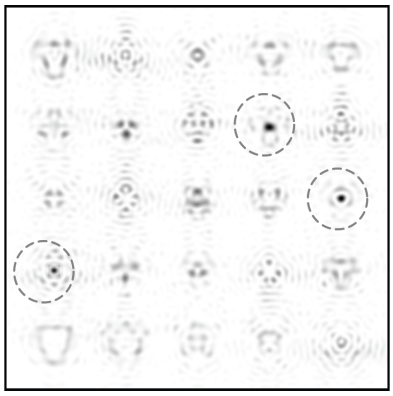
The filter is assumed to be illuminated by a plane wave. In this case, the analyser "splits" the incident beam onto 25 beams of approximately the same energy. 80% of the total illuminating beam energy is accounted for by these diffraction orders. From Fig. 2(b) the intensity is seen to be zero at all central points of the Fourier plane except for the zero order, (0,0), so meaning that the illuminating wavefront is aberration-free.

Figure 3 depicts the result of operation of the same 25-channel Zernike filter illuminated by the beam composed of three basis Zernike functions with the same weights and numbers, (*n,m*): (2,0)+(5,3)+(7,7). Shown in Fig. 3 are: (a) the illuminating beam intensity and (b) the diffraction pattern in the Fourier plane.

When compared with the distribution of mode numbers between the orders (Fig. 2(c)), Fig. 3(b) suggests that the intensity is non-zero (black spots in Fig. 3(b)) at the central points of the diffraction orders with the numbers (2,0), (5,3), and (7,7). Table 1 gives the corresponding averaged values in the vicinity of the central points for all orders (the vicinity size is 3x3 pixels).



(a)



(b)

Fig. 3 Operation of the Zernike filter (see Fig. 2(a)): (a) the illuminating beam intensity and (b) the diffraction pattern in the Fourier plane.

Table 1 Averaged intensity values in the vicinity of central points for the Fourier-plane orders. The Zernike filter (Fig. 2(a)) is illuminated by a beam composed of three modes: (2,0)+(5,3)+(7,7).

(7,1) **0,011**	***(6,6)*** **0,028**	***(6,4)*** **0,005**	***(6,2)*** **0,006**	***(6,0)*** **0,035**
(7,3) **0,103**	***(3,1)*** **0,013**	***(2,2)*** **0,018**	***(2,0)*** **0,977**	***(5,5)*** **0,008**
(7,5) **0,004**	***(3,3)*** **0,007**	***(0,0)*** **0,059**	***(1,1)*** **0,003**	***(5,3)*** **1,000**
(7,7) **0,683**	***(4,0)*** **0,056**	***(4,2)*** **0,000**	***(4,4)*** **0,001**	***(5,1)*** **0,001**
(8,0) **0,004**	***(8,2)*** **0,014**	***(8,4)*** **0,018**	***(8,6)*** **0,006**	***(8,8)*** **0,026**

One can see from Table 1 that the coefficients with the same weights in the input beam of the Zernike analyser possess different weights at the output:

$$\left|C_{20}\right|^2 = 0{,}977\ , \qquad \left|C_{53}\right|^2 = 1{,}000\ , \qquad \left|C_{77}\right|^2 = 0{,}683.$$

In addition, the intensity in the other orders is not zero. This is due to the fact that in an effort to obtain a purely phase filter in Eqs. (7) and (8), the amplitude is replaced by a constant value. Thus, the squared modules of coefficients at the Zernike analyser output are seen to have been measured with a relative error of 20%. There are two ways for reducing the error: a more exact computation of the Zernike filter phase combining different algorithms [14] and more accurate localisation of the diffraction order centres in which the coefficient modules are measured. In this section, an averaging value on area of 3x3 pixels was used. Such approach is less demanding for localisation but leads to a greater error. In the following section, we use another algorithm for centres' localisation.

4 Wavefront reconstruction using a multi-order Zernike filter

If in image recognition it suffices to compute the modules of the coefficients expanded in some orthogonal basis, this procedure is insufficient when reconstructing the light field complex amplitude. The unique reconstruction of the light field also requires the knowledge of the phase of the expansion coefficients.

We can reconstruct the coefficient phases if to the filter in Eq. (8) some linear combination of neighbouring basis functions is added [19]:

$$s_{nm}(r,\varphi) = \left\{\Psi^*_{nm}(r,\varphi) + \Psi^*_{n'm'}(r,\varphi)\right\} \times \\ \times exp\left[ikf^{-1}r\rho'_{nm}cos\left(\varphi - \theta'_{nm}\right) + \nu'_{nm}\right],$$

$$p_{nm}(r,\varphi) = \left\{\Psi^*_{nm}(r,\varphi) + i\Psi^*_{n'm'}(r,\varphi)\right\} \times \\ \times exp\left[ikf^{-1}r\rho''_{nm}cos\left(\varphi - \theta''_{nm}\right) + \nu''_{nm}\right].$$

In this case, the light intensity in the additional channels corresponding to the Fourier-spectrum points with spatial frequencies (ρ'_{nm}, θ'_{nm}) and (ρ''_{nm}, θ''_{nm}) are as follows:

$$S_{nm} = \left|C_{nm}\right|^2 + \left|C_{n'm'}\right|^2 + 2\left|C_{nm}\right|\left|C_{n'm'}\right|cos\left(\phi_{n'm'} - \phi_{nm}\right),$$

$$P_{nm} = \left|C_{nm}\right|^2 + \left|C_{n'm'}\right|^2 + 2\left|C_{nm}\right|\left|C_{n'm'}\right|sin\left(\phi_{n'm'} - \phi_{nm}\right),$$

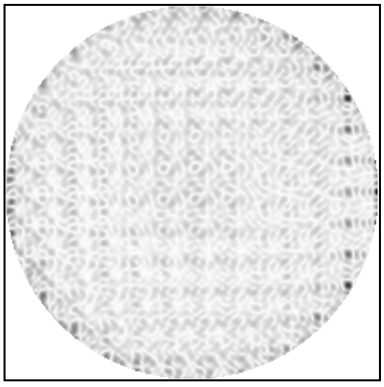
thus allowing the derivation of the phases ϕ_{nm}, for example, assuming $\phi_{00}=0$.

The recursive relationship for the sought-for phases may be written in the form

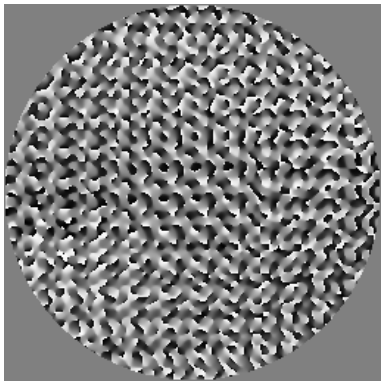
$$\phi_{n'm'} - \phi_{nm} = tan^{-1}\left(\frac{P_{nm} - I_{nm} - I_{n'm'}}{S_{nm} - I_{nm} - I_{n'm'}}\right).$$

Thus, the optical method under consideration makes it possible to find the complex coefficients of the light field expansion in terms of an orthogonal basis and to reconstruct this field.

We designed a 25-channel Zernike filter that can generate modes in different diffraction orders with the numbers (n,m): $n \le 4$ and $m \le 4$ (nine modes altogether) and their linear combination (8+8 altogether).



(a)



(b)

S8	S7	S6	S5	S4
P1	(3,1)	(2,2)	(2,0)	S3
P2	(3,3)	(0,0)	(1,1)	S2
P3	(4,0)	(4,2)	(4,4)	S1
P4	P5	P6	P7	P8

(c)

Fig. 4 (a) The half-tone amplitude and (b) phase of the Zernike filter, and (c) the distribution of modes numbered (n,m) and their linear combinations between the orders.

Figure 4 depicts (a) the half-tone amplitude and (b) the phase of the Zernike filter, and (c) the distribution of modes with the numbers (*n,m*) and their linear combinations between the orders.

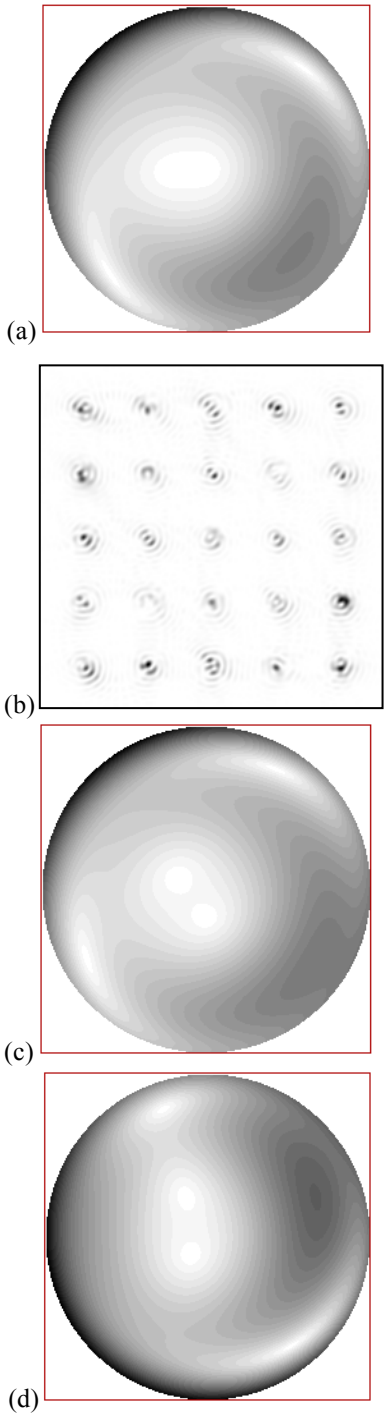


Fig. 5 (a) The intensity of the beam under analysis, (b) the diffraction pattern in the Fourier-plane produced by a purely-phase Zernike filter (shown in Fig. 4(a), (b)), (c) the light field reconstructed by an amplitude-phase filter, and (d) the light field reconstructed by the purely-phase filter.

Figure 5 depicts how such a 25-channel Zernike filter operates when illuminated by a beam composed of three modes with the coefficients C_{nm}: $C_{11}=exp(i0)$, $C_{33}=exp(i\pi/2)$ and $C_{42}=exp(i\pi)$. Shown in Fig. 5 are (a) the intensity of the beam under analysis, (b) the diffraction pattern in the Fourier plane for a phase-only filter, (c) the light field reconstructed by an amplitude-phase filter, and (d) the light field reconstructed by the phase-only filter.

Intensities of expansion coefficients are shown in Table 2. To measure coefficients' values, we search the maximum value in the defined vicinity of diffractive orders' localisations. Such approach gives a smaller error of coefficients measurement than the averaging used in the previous section. In particular, for phase-only filter the error has decreased from 20 % to 9 %. Thus, it is shown that correct definition of positions of diffractive orders is very important for correct solution of the problem.

The example suggests that in a wavefront analysing, when it will suffice to measure the modules of expansion coefficients, a phase-only filter may be used to advantage. When diffractive orders are localised sufficiently correct the error in measuring the modules of the expansion coefficients is less than 9%. At the same time, reconstructing the full information about the light field also requires the knowledge of the phase of the expansion coefficients. In this case, an amplitude-phase filter should be used.

5 Conclusions

Multi-ordered diffractive element fitted with the set of Zernike polynomials was proposed to use for the direct measurement of the wavefront aberration coefficients of eye optical system.

Investigations suggest that in a wavefront analysing, when it will suffice to measure the modules of expansion coefficients, a phase-only filter may be used to advantage (the error in measuring the modules of the expansion coefficients is less than 9% when diffractive orders are localised sufficiently correct). At the same time, reconstructing the full information about the light field also requires the knowledge of the phase of the expansion coefficients. In this case, an amplitude-phase filter should be used.

Thus, it is shown numerically that multi-order phase diffractive elements allow to confidently and simultaneously detect several tens of expansion coefficients. We conducted simulation experiments with different coefficients corresponding to aberrations of both low and high orders. Therefore, we do not expect significant variations in the measurement error due to the presence of large number of modes in the wave front. This will enable to investigate insufficiently known high-order aberrations for the differentiated diagnostics of eye diseases.

Acknowledgments

The work was in part financially supported by the Russian Foundation for Basic Research (grant ##13-07-00266, 14-29-07133, 15-29-03823) and the Ministry of education and science of the Russian Federation.

Table 2 Results of reconstructing the complex coefficients by an amplitude-phase and phase-only filters.

Coefficients	$\lvert C_{11}\rvert^2$	$\lvert C_{33}\rvert^2$	$\lvert C_{42}\rvert^2$	Error	$\phi_{33}-\phi_{11}$	$\phi_{42}-\phi_{33}$
Initial	1	1	1		1,57	1,57
Reconstructed by the amplitude-phase filter	0,272	0,274	0,279	3,1%	1,46	1,54
Reconstructed by the phase-only filter	12,12	14,83	14,59	8,6%	0,95	1,53

Compact optical tweezer capable of dynamic control

Alexander Korobtsov[1], Svetlana Kotova[1,2], Nikolay Losevsky[1,2], Aleksandra Mayorova[1,2*], Sergey Samagin[1]

[1] Lebedev Physical Institute, 221 Novo-Sadovaya Str., Samara 443011, Russia

[2] Samara State Aerospace University (SSAU), 34 Moskovskoye Shosse, Samara 443086, Russia

[*] **e-mail:** mayorovaal@gmail.com

Abstract. The extension of capabilities towards the formation of controlled complex-shaped optical traps is demonstrated for the compact laser tweezer based on the four-channel LC modulator. The experimental results on the yeast cell manipulation, including the particles larger than 10 μm, are presented. The capture and confinement of the object with the dimensions 37 μm × 13 μm was realized by means of the use of the ellipse-shaped trap. The maximal escape velocity of this object was about 20 μm/s. © 2015 Samara State Aerospace University (SSAU).

Keywords: compact laser tweezers, optical manipulation, liquid crystal modulators, biological microobjects.

Paper #2473 received 2015.06.02; revised manuscript received 2015.06.19; accepted for publication 2015.06.25; published online 2015.06.30.

References

1. T. C. Bakker Schut, E. F. Schipper, B. G. de Grooth, and J. Greve, "Optical-trapping micromanipulation using 780-nm diode lasers," Optics Letters 18(6), 447-449 (1993).
2. R. Afzal, and E. Treacy, "Optical tweezers using a diode laser," Rev. Sci. Instrum. 63(4), 2157-2163 (1992).
3. S. Smith, S. Bhalotra, A. Brody, B. Brown, E. Boyda, and M. Prentiss, "Inexpensive optical tweezers for undergraduate laboratories," Am. J. Phys. 67(1), 26-35 (1999).
4. A. Ashkin J. M. Dziedzic, and T. Yamane, "Optical trapping and manipulation of single cells using infrared laser beams," Nature 330, 769-771 (1987).
5. J. Bechhoefer, and S. Wilson, "Faster, cheaper, safer optical tweezers for the undergraduate laboratory," Am. J. Phys. 70(4), 393-400 (2002).
6. M. Šery, Z. Lošt'ak, M. Kalman, P. Jakl, and P. Zemanek, "Compact laser tweezers," Proc. of SPIE 6609, 66090N (2007).
7. Y. Ogura, K. Kagawa, and J. Tanida, "Optical manipulation of microscopic objects by means of vertical-cavity surface-emitting laser array sources," Applied Optics 40(30), 5430-5435 (2001).
8. T. Suzuki, T. Maeda, O. Sasaki, and S. Choi, "Enhancement of optical gradient force employed in optical tweezers using a pulsed laser diode," Conference Paper Optical Trapping Applications (Monterey, California, United States, April 4-6, 2011), OTMD4p.pdf (2011).
9. T. Piñón, L. Hirst, and J. Sharping, "Fiber-Based Dual-Beam Optical Trapping System for Studying Lipid Vesicle Mechanics" in Optics in the Life Sciences, OSA Technical Digest (CD), OTTuB2.pdf (2011).
10. K. Taguchi, J. Okada, Y. Nomura, and K. Tamura, "Three-Dimensional Optical Trapping for Cell Isolation Using Tapered Fiber Probe by Dynamic Chemical Etching," Journal of Physics: Conference Series 352, 012039 (2012).
11. K. Taguchi, S. Hirota, H. Nakayama, D. Kunugihara, and Y. Mihara, "Optical Manipulation of Symbiotic Chlorella in Paramecium Bursaria Using a Fiber Axicon Microlens," Journal of Physics: Conference Series 352, 012040 (2012).
12. K. Taguchi, H. Ueno, T. Hiramatsu, and M. Ikeda, "Optical trapping of dielectric particle and biological cell using optical fiber," Electron Lett. 33, 413-414 (1997).
13. K. Taguchi, and N. Watanabe, "Single-beam optical fiber trap," Journal of Physics: Conference Series 61, 1137–1141 (2007).
14. C. Xie, M. A. Dinno, and Y.-Q. Li, "Near-infrared Raman spectroscopy of single optically trapped biological cells," Optics Letters 27(4), 249-251 (2002).

15. R. W. Applegate, Jr., J. Squier, T. Vestad, J. Oakey, and D. W. M. Marr, "Optical trapping, manipulation, and sorting of cells and colloids in microfluidic systems with diode laser bars," Optics Express 12(19), 4390-4398 (2004).
16. R. W. Applegate, J. Squier, T. Vestad, J. Oakey, and D. W. M. Marr, "Fiber-focused diode bar optical trapping for microfluidic flow manipulation," Applied Physics Letters 92, 013904 (2008).
17. R. W. Applegate, Jr., J. Squier, T. Vestad, J. Oakey, D. W. M. Marr, P. Bado, M. A. Dugan, and A. A. Said "Microfluidic sorting system based on optical waveguide integration and diode laser bar trapping," Lab Chip. 6(3), 422-426 (2006).
18. R. Applegate, Jr., D. Marr, J. Squier, and S. Graves, "Particle size limits when using optical trapping and deflection of particles for sorting using diode laser bars," Optics Express 17(19), 16731 (2009).
19. S. Cran-McGreehin, T. Krauss, and K. Dholakia, "Integrated monolithic optical manipulation," Lab Chip 6, 1122–1124 (2006).
20. F. C. Cheong, C. H. Sow, A. T. S. Wee, P. Shao, A. A. Bettiol, J. A. van Kan, and F. Watt, "Optical travelator: transport and dynamic sorting of colloidal microspheres with an asymmetrical line optical tweezers," Appl. Phys. B 83, 121–125 (2006).
21. A. A. Ambardekar, Y.-Q. Li, "Optical levitation and manipulation of stuck particles with pulsed optical tweezers," Optics Letters 30(14), 1797-1799 (2005).
22. I. Sraj, D. W. M. Marr, and C. D. Eggleton, "Linear diode laser bar optical stretchers for cell deformation," Biomedical Optics Express 1(2), 483-488 (2010).
23. I. Sraj, J. Chichester, E. Hoover, R. Jimenez, J. Squier, C. D. Eggleton, and D. W. M. Marr, "Cell deformation cytometry using diode-bar optical stretchers," J. Biomed. Opt. 15(4), 047010-1 (2010).
24. C. Xie, C. Goodman, M. A. Dinno, and Y.-Q. Li, "Real-time Raman spectroscopy of optically trapped living cells and organelles," Optics Express 12(25), 6208-6214 (2004).
25. W. Cheng, X. Hou, and F. Ye, "Use of tapered amplifier diode laser for biological-friendly high-resolution optical trapping," Optics Letters 35(17), 2988-2990 (2010).
26. H. Schneckenburger, A. Hendinger, R. Sailer, M. H. Gschwend, W. S. Strauss, M Bauer, and K. Schütze, "Cell viability in optical tweezers: high power red laser diode versus Nd:YAG laser," J Biomed Opt. 5(1), 40-44 (2000).
27. T. Suzuki, T. Maeda, O. Sasaki, and S. Choi, "Enhancement of optical gradient force employed in optical tweezers using a pulsed laser diode," Conference Paper Optical Trapping Applications (Monterey, California United States April 4-6, 2011) (2011)
28. Y. F. Chen, Y. P. Lan, "Spontaneous pattern formation in a microchip laser excited by a doughnut pump profile," Appl. Phys. B. 75, 453-456 (2002).
29. Y. F. Chen, and Y. P. Lan, "Transverse pattern formation of optical vortices in a microchip laser with a large Fresnel number," Physical Review A 65, 013802 (2001).
30. P. Genevet, S. Barland, M. Giudici, J. R. Tredicce, "Bistable and Addressable Localized Vortices in Semiconductor Lasers," Physical Review Letters 104, 223902 (2010).
31. V. Voignier, J. Houlihan, J. R. O'Callaghan, C. Sailliot, and G. Huyet, "Stabilization of self-focusing instability in wide-aperture semiconductor lasers," Phys. Rev. A 65, 053807 (2002).
32. J. Mukherjee, and J. G. McInerney, "Lateral mode dynamics in high-power wide-aperture quantum dot laser," Proc. SPIE 6468, 64681A (2007).
33. A. A. Krents, and D. A. Anchikov, "The vortex lattices in large-aperture lasers," Izvestiya of Samara scientific center of the Russian Academy of Sciences 14(4), 201-205 (2012) [in Russian].
34. D. A. Anchikov, A. A. Krents, and A. V. Pahomov, "Stability of transvers optical patterns in wide-aperture," Izvestiya of Samara scientific center of the Russian Academy of Sciences 15(4), 99-103 (2013) [in Russian].
35. R. Skidanov, M. Rykov, G. Iannacchione, and S. Krivoshlykov, "The modification of laser beam for optimization of optical trap force characteristic," Computer optics 36(3), 377-386 (2012).
36. S. Fore, J. Chan, D. Taylor, and T. Huser, "Raman spectroscopy of individual monocytes reveals that single-beam optical trapping of mononuclear cells occurs by their nucleus," J. Opt. 13, 044021 (2011).
37. S. Kotova, V. Patlan, and S. Samagin, "Tunable liquid crystal focusing device: I. Theory," Quantum Electron. 41, 58–64 (2011).
38. S. Kotova, V. Patlan, and S. Samagin, "Tunable liquid crystal focusing device: II. Experiment," Quantum Electron. 41, 65–70 (2011).
39. S. Kotova, V. Patlan, and S. Samagin, "Focusing light into a line segment of arbitrary orientation using a four channel liquid crystal light modulator," J. Opt. 15, 035706 (2013).
40. A. Korobtsov, S. Kotova, N. Losevsky, A. Mayorova, V. Patlan, and S. Samagin, "Optical trap formation with a four-channel liquid crystal light modulator," J. Opt. 16, 035704 (2014).
41. A. Korobtsov, S. Kotova, N. Losevsky, A. Mayorova, and S. Samagin, "Formation of contour optical traps with a four-channel liquid crystal focusator," Quantum Electron. 44, 1157–1164 (2014).

42. S. Kotova, A. Mayorova, and S. Samagin, "Tunable 4-channel LC focusing device: summarized results and additional functional capabilities," J. Opt. 17, 055602 (2015).
43. A. Korobtsov, S. Kotova, N. Losevsky, A. Mayorova, S. Samagin, and V. Volostnikov, "Trapping of microscopic objects by contour optical traps formed by 4-channel liquid crystal modulator," Journal of Physics: Conference Series 605, 012007 (2015).
44. R. V. Skidanov, A. A. Morozov, A. P. Porfirev, "Composite light beam and mixroexplosion for optical micromanipulation," Computer optics 36(3), 371-376 (2012).

1 Introduction

For technological applications of optical tweezers (e.g., their introduction into the clinical practice for solving particular biomedical problems) it is important to simplify the construction and the control system of these devices, to reduce their size and cost. From this point of view the semiconductor lasers seem to be attractive due to their high efficiency, compactness, and easy control of the radiation characteristics directly by varying the pumping current. The first publications on the use of laser diodes for fabricating a relatively cheap and compact optical tweezer appeared in the middle of nineties of the last century [1-3]. Later the semiconductor lasers have been used in laser tweezers based on optical fibres, which allowed the construction of a compact Raman tweezer. The laser diode-based optical tweezers have found wide application in microfluidic techniques.

On the other hand, the optical tweezers based on the semiconductor lasers possess a number of advantages exactly for biomedical applications, related, first of all, to the radiation wavelength range of the semiconductor lasers. The optical trapping stability in the infrared range with the possibility of significant reduction of the damage of living cells as compared to the visible range was clearly demonstrated in Ref. [4]. In the patent by Ashkin and Dziedzic it was recommended to use the lasers with the wavelength 0.8 – 1.8 μm for capturing the microobjects of the biological origin. There are a number of commercially available semiconductor lasers in this spectral range.

In this paper we present a brief review of the studies, devoted to the invention and development of optical tweezers based on semiconductor lasers, as well as to their use in biomedical applications. But it must be noted that due to laser techniques development not only semiconductor lasers but also small-size DPSS laser modules, including laser pointers, can be used as a source of radiation in compact inexpensive laser tweezers. In this paper we consider the specific technical features of the compact optical tweezer constructed by us, for which the capabilities of forming the traps with different shapes and dynamic manipulation can be essentially extended by means of using the four-channel LC modulator (LC focusing device).

2 Using semiconductor lasers in optical tweezers

2.1 Specific features of beam formation and technological advantages

The main problem discussed in the first papers on the use of semiconductor lasers in optical tweezers was the problem of sharp focusing of the beam from a semiconductor laser that possesses ellipticity and astigmatism. This problem was solved by correcting the beam asymmetry with anamorphotic prisms [2, 3], diaphragms, single-mode fibres, or objective aperture. In these methods the loss of up to 50% of power is observed, however, they all have been successfully used by the authors of Ref. [3] for trapping polystyrene particles, as well as the yeast and bacteria cells, by the optical tweezer based on the semiconductor laser. In Ref. [5] the problem of preliminary correction of the ellipticity and astigmatism for the beam from the laser diode was solved by means of using cylindrical optics. For the formation of the optical trap the laser diode with the miniature cylinder (Blue Sky Research) built in the case was used. An alternative approach was used by the authors of Ref. [1] who formed an optical trap using the aspheric CD lenses (Philips) specially manufactured for focusing strongly diverging beams. It was noted that the outgoing beam after the lens was elliptic, and the intensity profiles were more flat-top shaped in comparison with Gaussian beams. As sources of radiation, the single-mode gain-guided GaAlAs lasers with the maximal output power 40-50 W and the radiation wavelength 780 nm were used. The formation of traps was implemented using the microscope objectives (32×, NA=0.4) that allowed the focusing of the beam into a spot with the diameter 1.5 μm. The authors formed two types of traps, the single-beam trap and the double-beam one (in which two laser diodes were used). The optical manipulation experiments were performed with aqueous suspensions of polystyrene spheres having the diameter 9.6 μm and the refractive index 1.58, as well as with the human lymphocytes.

The authors of Ref. [6] presented the so called compact optical tweezers (COT) based on laser diodes. The specific feature of their tweezer is that the laser diode (Sanyo DL-8031-031A, radiation wavelength 808 nm, maximal power 200 mW) together with the correcting optics (aspherical lens, anamorphotic prism, mirrors) was inserted directly into the microscope tube

between the ocular and objective. The optical system was optimised by means of the original program (Zemax optical program) to provide the sharp (optimal) beam focusing. The power stability in the focus was provided by the temperature stabilisation of the laser diode using the special module Supercool PE-017-06-11. The authors use the term COT for the entire construction, including all elements mentioned above. The COT was designed to provide the minimal size, simplicity of the use, and modularity. The system was installed into the inverted microscope (Olympus IX-70, 100x), the objective of which formed the optical trap. The trapping was demonstrated for polystyrene particles with the size from 0.5 μm to 30 μm, suspended in water, and for the yeast cells.

Semiconductor lasers were successfully used for the construction of multiple traps. For the first time this technique was described in Ref. [7]. For optical trapping the authors used an array of vertical-cavity surface-emitting lasers (VCSEL array). In particular, they used the 8×8 VCSEL array (NTT Photonics Laboratory) with the radiation wavelength 854±5 nm, the output power exceeding 3 mW, the aperture diameter 15 μm, and the mesh 250 μm. The advantage of such tweezer is the possibility of controlling the radiation of every laser independently, which allows flexible manipulation of microscopic objects. Besides that, the, VCSEL array is easily combined with microoptics, the control of the displacement is implemented by switching on and off the appropriate elements, which allows the technological simplification of the system. The experiments on simultaneous trapping and moving of two microscopic objects (polystyrene microspheres with the diameter 6 μm and 10 μm) with two elements of the array switched on were demonstrated. The displacement of the particles in the liquid was implemented by moving the substrate. The power of radiation in the trap was less than 10 mW. It was also shown that the microobject can be moved along a certain trajectory (in particular, the L-shaped trajectory was realized) by switching the individual elements of the array. In Ref. [8] the multiple-beam optical trap for manipulating of several objects at once was formed using the acoustooptical deflector (AOD). The beam of the semiconductor laser with the radiation wavelength 780 nm and the output power 90 mW was incident on the AOD and then the first diffraction order was focused on the sample. The multiple trapping was implemented by fast scanning of the beam over the AOD. The aqueous suspensions of polymer spheres were used as samples.

Semiconductor lasers were used in optical fibre laser tweezers, both in the double-beam one based on two single-mode fibres and two diode lasers with the wavelength 980 nm [9], and in the single-beam tweezer developed by the research team from Japan [10,11]. In the latter the sharply focused beam was formed at the output from the optical fibre with high numerical aperture. Such optical tweezer was proposed by the authors in Ref. [12]. The laser semiconductor module was used for the first time in their tweezer for the experimental study of the dependence of trapping efficiency upon the distance (along the z-axis) between the fibre and the substrate [13]. The radiation wavelength was 1.48 μm. The role of microscope objectives was played by polystyrene and silicon particles with the diameter 10 and 5 μm, respectively, dispersed in ethanol. In these experiments the 2D trap was implemented. Later the 3D trapping was achieved at the expense of the specially shaped tip of the optical fibre. The chemical etching method was used to form the sharp tip (17°) [10] or axicon [11]. In these papers the laser module with the wavelength 980 nm was used, which allowed one to perform experiments with biological objects.

The use of a low-power laser diode (the wavelength 785 nm) simultaneously for optical trapping and for exciting the Raman scattering allowed the authors of Ref. [14] to create a compact laser tweezers Raman spectroscopy (LTRS) system. To provide the trap formation, the beam from the semiconductor laser was introduced into the inverted microscope with high numerical aperture of the objective (100×, NA=1.3). The same laser could be used to excite the Raman scattering from the trapped particle. The scattered radiation was collected by the same objective and entered into a spectrograph. The laser was switched from one power value to another; for trapping the power of 2 mW (directly on the sample) was used, and to excite the scattering the power was switched to 15 mW for a short period of time. The experiments were performed with the aqueous suspensions of RBCs and yeast cells (living and dead). The spectral difference between the different types of cells was observed. It is worth noting that the studies on combining the optical trapping methods with IR and Raman spectroscopy have been carried out by other authors too, and not only for identification of biological objects. The specific feature of the studies performed by the group of Ch. Xie is just the use of a semiconductor laser for this goal.

Optical tweezers based on laser diodes have found wide application in microfluidic systems. Thus, a series of papers [15-18] by R. Applegate Jr., D. Marr, J. Squier, S. Graves et.al. (USA) are devoted to the microfluidic flow manipulation of microobjects using a bar of diode lasers. The authors of the paper report the simple and relatively cheap technique that allows the control of a large capture zone without the necessity of laser beam scanning or varying its phase. In Ref. [15] the trap in the form of a light segment was formed by using a bar of laser diodes (JDS Uniphase, SDL-6300) with the dimensions 100 μm×1 μm, radiating at the wavelength 980 nm and having the power up to 3W. To form sharply focused beams the microscope objective 40× with the numerical aperture 0.65 was used. The resulting segment allowed simultaneous trapping and alignment of several particles along the light line. The results of such experiments were demonstrated for polystyrene particles having the diameter 1.8 μm, 10 μm, as well as for red blood cells. Increasing the dimensions of the diode lasers bar to 460 μm×1 μm with

the maximal output power 5 W at the wavelength 808 nm made it possible to trap and sort larger (exceeding 100 μm) particles [18]. The proposed technique was further developed by using an optical fibre instead of the microscope objective for focusing [16]. This allowed R. Applegate Jr. et al. to construct a portable optical tweezer for using in microfluidic techniques and to make the injection of radiation into the microfluidic systems and the control of the optical trap inside them easier by using the optical fibres. To form the optical trap in the form of a light segment, the bar of diode lasers (Snoc Electronics, LD-005) with the built-in cylindrical microlens was used. The bar dimensions were 200 μm× 1 μm, the mean power was 3 W, and the radiation wavelength was 808 nm. The output radiation was projected directly onto the sample through the polymer fibre with the diameter 1 mm with the refractive index 1.49 (Industrial Fiber Optics), placed perpendicularly to the beam trajectory. A unique module for optical manipulation was presented in Ref. [19]. A specific feature of the device is that the microfluidic channels are formed directly in the laser active medium. The module is fully portable and does not require alignment. In the module four lasers were used placed in pairs against each other. The counter-propagating optical beams in each pair formed the optical trap. The device was based on the GaAs/AlGaAs heterostructure with InAs quantum dots and radiated at the wavelength 1290 nm. A similar system operating at the wavelength 980 nm was fabricated on the base of the heterostructure with GaAs quantum wells. The microchannels were etched chemically inside the structure. The authors experimentally demonstrated the capabilities of the module for solving many manipulation problems. In particular, one particle or a few particles of polystyrene with the diameter of 5 μm were captured and trapped. The trapped particle was then released from the trap by switching on and off the appropriate pair of lasers forming the trap. The possibility of transferring the particles from one trap to another between the traps separated by 100 μm in the direction, perpendicular to the flow, was demonstrated. The possibilities of trapping a biological particle, aligning a few colloid particles along the line, perpendicular to the flow, etc., were also demonstrated.

The so called optical travolator (horizontal transporter) for transporting and dynamical sorting of colloid particles in aqueous suspensions was presented in Ref. [20]. The travolator is an optical trap in the form of a light segment with the asymmetric intensity profile, shaped using the diode laser (SUWTech LDC-2500) with the radiation wavelength 1064 nm and the maximal output power 400 mW in combination with cylindrical lenses. The laser beam was split into two beams using a beam splitter. Each beam was passed through a cylindrical lens (the lenses were tilted and shifted with respect to the optical axis) and then the light from two arms was collected and sent to the microscope. In the setup the inverted microscope (Nikon TE300) with the immersion objective (100×, NA=1.3) was used. The samples were aqueous suspensions of negatively charged particles of polystyrene or silicon. To create a liquid flow in the cuvette with the sample the voltage from 0 to 110 V was applied using the picoamperemeter to the especially built-in copper electrodes in the cuvette. The applied electric field provided a uniform flow, and the velocity of the particles motion was controlled by the value of the applied voltage. Using the formed light segment, the authors carried out the experiments on transporting silicon microspheres with the diameter 1.58 μm along the segment. Moreover, they placed two segments at some angle to each other to redirect the particles (polystyrene spheres with the diameter 1.2 μm) and to concentrate them in the bounded volume. In the paper the results of the experiment on sorting the particles of two sizes, 1.2 μm and 3.2 μm, were also presented. The possibility of manipulating the objects of biological origin was demonstrated by the authors by the example of yeast cells.

An interesting technique of trapping and manipulating the microobjects of different nature (polystyrene particles, yeast cells, *Bacillus cereus* bacteria) was described in Ref. [21]. To tear the microobjects from the substrate the authors used the infrared (the wavelength 1.06 μm) pulsed laser. The great gradient force (up to 10^9 N) arising for the short time (about 45 microseconds) allowed the particle to overcome the substrate adhesion. Then the continuous-wave low-power diode laser with the radiation wavelength 785 nm was used to trap and manipulate the particle, lifted above the substrate.

2.2 Applications in biomedical studies

In fact, the authors of all the papers mentioned above pointed out the promising potentialities of the optical tweezers based on laser diodes of the infrared range for biomedical applications and demonstrated the possibility of optical manipulation for the objects having the biological origin, e.g., bacteria [3, 21], yeast cells [3, 6, 10, 14, 20], human erythrocytes [14, 22, 23] and lymphocytes [1]. In Ref. [10] the experiments on isolating the symbiotic chlorella from *Paramecium Bursaria* were described. The dependences of the stretching of single-layer liposome membranes upon the radiation power and the relative refractive index were studied by the authors of Ref. [9]. The liposomes were stretched by means of the double-beam optical fibre tweezer, the power being varied from 30 mW to 53 mW. To change the refractive index of the aqueous solution the special polymer (polyethylene glycol, PEG) was added in different concentrations. The results of the experiments on erythrocyte stretching both in stagnant fluid and in the flow, obtained using the technologically simple asymmetric optical trap based on an inexpensive diode laser, are presented in Refs. [22, 23]. Interesting results for biomedical applications were obtained using the compact LTRS system. The technique proposed in Ref. [14] and described above in Section 2.1 acquired further development, namely, the variations of Raman

spectra of cells and yeast depending on the solution temperature were studied, the *in vivo* spectra were measured for the living pine cells, e-coli, and a number of other biological objects [22].

Of particular interest are the studies performed by the authors of Ref. [25], where the advantages of laser diode-based optical tweezers with the wavelength 830 nm are discussed in comparison with those using the Nd:YAG laser (1064 nm). The authors point out the drawbacks of using the radiation at the wavelength 1064 nm in optical tweezers. These drawbacks include the heating of water, the formation of temperature gradient close to the radiation focus, and the production of active forms of oxygen (in the presence of a stabiliser) that lead to the destruction of the biological samples. In particular, the destruction of nucleic acids and phosphodiester bonds was reported. It was asserted that there are two optimal wavelengths for the trapping of living cells, 830 nm and 970 nm. Just at these wavelengths the phototoxicity is minimal. Besides that, the authors ascribe to the drawbacks of the radiation wavelength 1064 nm the high transmittance of silicon at the wavelengths exceeding 1 μm, which leads to problems with the response of silicon detectors. As already mentioned, the experiments were carried out using two lasers, 830 nm and 1064 nm, respectively. A double-beam trap was formed, in which two diverging beams propagated towards each other. This trap was used to stretch the RNA. The experiments on trapping the mammary gland cells were also performed. It was shown that the cells did not die, in spite of relatively high power delivery (the observations were carried out during a few hours). Besides that, the authors experimentally found that at the wavelength of 830 nm the two-photon excitation of green fluorescence in the protein molecules occurs. This is expected to allow the future study of single protein molecules in a living cell.

Note, that the studies devoted to the comparative analysis of optical tweezers based on laser diodes of the visible range and the laser of the infrared range have been carried out significantly earlier. Thus, the paper by H. Schneckenburger, et al. [26] presents the results of direct comparison of the viability of the cultivated Chinese hamster ovary cells under different doses of irradiation in the course of trapping with optical tweezers based on the laser diodes, emitting in the visible range (670-680 nm), and on the Nd:YAG laser (1064 nm). On the one hand, the experimental results demonstrated the advantages of IR range, when the radiation doze is large (2.4 GJ/cm^2). On the other hand, it was shown that no cell destruction occurs also for the visible-range radiation with the dose of 340 MJ/cm^2.

The authors of Ref. [27] have found that for the same powers of radiation the gradient force in the trap using a pulsed laser is much larger as compared to the continuous-wave laser. To the opinion of the authors, this fact allows one to expect easy formation of optical tweezers for operating with biological samples, since the trap based on pulsed laser diodes is simultaneously characterised by sufficient rigidity (from the point of view of optical trapping) and softness (from the point of view of minimal damage of the samples).

2.3. Possible prospects

In the context of optical manipulation the beams with nonzero angular momentum are of particular interest. Due to the angular momentum transfer, the so called vortex beams are able to rotate the microobjects, move them along the predetermined trajectories, and cause different types of deformation. From this point of view the wide-aperture surface-emitting semiconductor lasers with vertical cavity are rather interesting, since in their cross section stable arrays of vortices arise. The construction of such semiconductor lasers provides the generation of a single longitudinal mode and a large number of transverse modes. The nonlinear interaction between high-order transverse modes gives rise to the appearance of complex optical field structures, in particular, to the formation of regular arrays of optical vortices and spiral waves. The spontaneous (without additional optical elements) formation of such stable structures was experimentally observed in Refs. [28-30]. For example, in Ref. [28] the variation of the transverse structure of a wide-aperture vertical-cavity laser under the variation of the pumping current was studied experimentally. It was found that with the growth of the pumping current beyond the threshold values the arrays of vortices can be observed. In Ref. [30] P. Genevet et al. experimentally demonstrated that the localised states in wide-aperture lasers can possess the orbital angular momentum. A number of papers were devoted to the studies, aimed at the development of a complete theory explaining and describing the dynamics of birth, existence and destruction of complex structures in wide-aperture lasers [31-34].

Obviously, the arrays of optical vortices arising in wide-aperture semiconductor lasers are of a certain interest for the problem of optical manipulation, however, no papers on the implementation of optical tweezers using such lasers could be found.

3 Compact setup for manipulating microscopic objects

Figure 1 presents the compact laser micro-manipulator based on the optical microscope XSP-104.

In the manipulator any small-size semiconductor laser module, or small-size DPSS laser modules, including laser pointers, can be used as a source of radiation. To apply a certain type of the laser module with definite wavelength, it is necessary to adjust the appropriate dichroic mirror in the especially fabricated adapter together with the corresponding optical filters at the input of the adapter and the input of the digital camera. The particular experiments were carried out with the semiconductor laser module DMH-650-60 (the wavelength 650 mn, the maximal power 60 mW), DPSS module DME-532-80 (the wavelength 532 nm, the maximal power 80 mW), portable DPSS module (laser pointer) LPH-532-150star (the wavelength 532 nm, the

power 50 mW, and the wavelength 1.06 μm, the power 90 mW). When operating with LPH-532-150star, the selection of radiation at the desired wavelength was implemented using the appropriate optical filters.

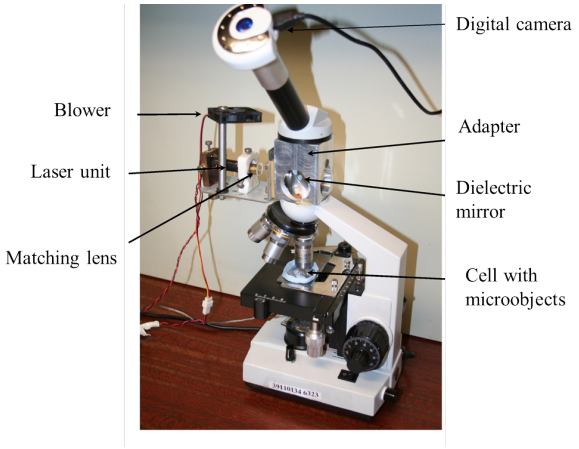


Fig. 1 Photograph of the compact laser tweezer.

The cooling of the laser module is implemented by means of the miniature blower attached to the stage with the supply voltage 12 V. The negative lens with the optical power 6 dioptres is glued to the output face of the laser module coaxially with the beam, output from the module. This lens provides the matching of the laser radiation focusing plane and the plane where the microobjects are found within the operating zone of the manipulator. Moreover, this lens expands the laser beam to the diameter of the entrance aperture of the microscope objective, which allows the reduction of the focusing spot. The module is supplied from the standard power supply unit, providing the control of the laser output power.

The microscope was upgraded by installing the especially fabricated adapter between the ocular unit and the microscope objective unit. Inside the adapter the adjustable bushing is placed, to which the dielectric mirror (the reflection coefficient 70% at the wavelength 0.65 μm for the light incident at the angle of 45°) is attached, tilted by the angle 45° with respect to the optical axis of the microscope. The adapter also incorporates the additional bushing for mounting optical filters that provide the attenuation of laser radiation, coming from the working zone to the photodetector of the digital camera. On the outside the rigid metallic plate is attached to the case of the adapter, on which the laser module alignment device is assembled. The alignment device provides the translational movement of the laser module in two mutually perpendicular transverse directions and the tilt of the module in two angles. The video recording is implemented using the ocular digital camera DCM-130 with the resolution of 1.3 megapixels, from which the image is transmitted to the computer.

The cell with microobjects suspended in a liquid is placed on the object stage of the microscope. The laser beam passing through the microscope objective (100×, NA=1.25) is focused into a spot with the diameter about 1.5 μm, thus forming a point optical trap. The calibration of the optical trap using the force drag method, the direct measurement of the optical trap forces depending on the parameters of the captured objects, their position, and also the characteristics of the trap itself, the quantitative assessment of micromechanical properties of complex liquid media (polymers, membranes, biotissues), and a number of other problems imply the implementation of the controlled movement of the microscope object stage with sub-micrometre accuracy. For this goal the stage of the microscope XSP-104 was equipped with the step motors (SY 35ST26-0284A) and the appropriate drives with the step 0.132 μm of the displacement in the horizontal plane. The especially designed control unit and the developed software (graphic user interface) allow the real-time control of the step motors operation from the monitor screen, where the operating field of the microscope is displayed. In particular, the system allows one to put the cell into the starting position for the initial capture of the microobject and to move the stage with the cell with microobjects with given initial velocity and constant acceleration. Similarly, a special module provides the movement of the stage with the cuvette and particles along the z axis with the step 125 nm. Thus, the considered compact manipulator allows the formation of point optical traps and the control of their position with high precision.

4 Contour trap formation

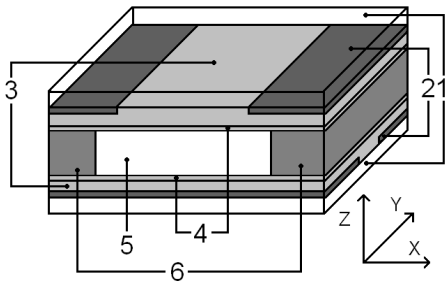
In some problems it is required to form optical traps with the shape more complex than the point trap, namely, with the shape of rings, ellipses, light segments, etc. In biomedical studies the interest to such optical traps is related, first of all, to the problem of minimising the negative effect of laser radiation on the trapped object. As mentioned above, the essential reduction of this effect is possible at the expense of the optimal choice of the wavelength, in particular, using the diode lasers operating in the infrared range. Nevertheless, as it was correctly pointed out in Refs. [35, 36], for trapping of single eukaryotic cells with the size greater than the point trap, the maximal impact is at the nucleus as the most dense structure of the cell. Hence it is desirable to provide the stable capture of a cell by its peripheral part using the traps having the shape of rings, ellipses, or arcs. Correspondingly, the interest to the traps having the form of light segments can be related to the necessity of capturing and orientation of elongated objects.

The multi-pixel liquid crystal spatio-temporal light modulators (LC STLMs) possess unique capabilities for forming complex-shaped traps and dynamic control of their configuration, so they are widely used in the optical manipulation. However, their use in compact, technologically simple and relatively inexpensive optical tweezers can be unreasonable. Alongside with the high cost and the operation in the reflected light (which leads to the increase of the dimensions of the

optical tweezer system), the drawbacks of the LC STLMs include the relatively low diffraction and energy efficiency. As an alternative to the multi-pixel modulator, we use the four-channel LC modulator (LC focusing device) for the formation of complex-shaped traps in the compact optical tweezer setup. The schematic diagram illustrating the construction of LC focusing device is presented in Fig. 2 and considered in detail in Refs. [37-43]. The device consists of two cylindrical modal LC lenses, joined into a single unit. The layer of nematic LC is enclosed between two glass substrates with transparent high-resistance coatings and low-resistance strip contacts deposited on them. The substrates are placed so that their contact electrodes are perpendicular to each other. By controlling the electrophysical parameters of the device one can vary the distribution of the electric voltage over the aperture. Under the action of the voltage the reorientation of molecules (S-effect) occurs in the LC layer. This leads to the change of the spatial distribution of the phase shift, contributed by the LC layer to the phase of the transmitted light wave.



a



b

Fig. 2 Exterior view (a) and schematic diagram (b) of the LC focusing device: 1 – glass substrates, 2 – contact electrodes, 3 - high-resistance conducting layer, 4 – orienting coating, 5 - LC layer, 6 – spacers. The diameter of the white case is 5.5 cm, the area of the small spot in the centre of the device (aperture) is 1 mm×1 mm.

The scheme of experimental setup is presented in Fig. 3. The specific feature of the optical trap formation using the four-channel LC modulator is that the device operates in the transmission mode. This fact allows the simplification of the optical tweezer scheme and the reduction of its dimensions. In order to get the complex-shaped optical traps in a compact optical tweezer the device is placed after the laser module and collimator. For controlling the LC focusing device we used the computer-controlled four-channel generator of sinusoidal oscillations [38]. The control unit allows the application of four independent potentials having the same frequencies, the controlled amplitudes in the range from 0 to 12.5 V, and the phase shift from 0 to 2π to the contacts of the focusing device. Thus, using only four control contacts one can produce different intensity distributions, control their shape and size, and move them across the focusing device aperture.

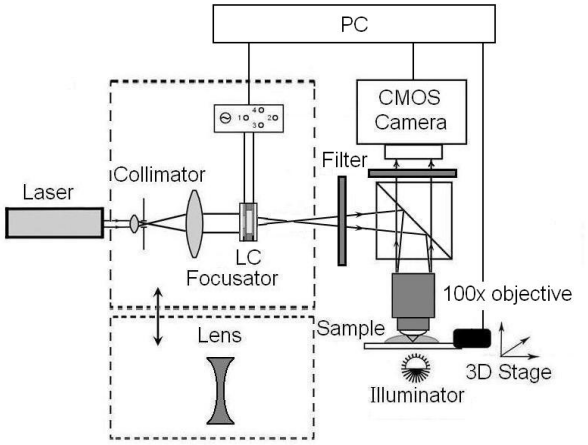


Fig. 3 The scheme of experimental setup. The frame with collimator and LC focusing device is used for the contour traps formation and the frame with diverging lens is used for the point trap formation.

Note, that the light field intensity distributions having the contour shapes are typically produced at the distance from 3 to 6 cm from the focusing device. The distance and the form of the contour trap depend on the phase shift profile, the deflection value, and the distribution width. To get the desired light distribution in the plane of microobject manipulation, one has to match the microscope observation plane with the plane where the contour filed is formed after the LC focusing device. Thus one can create optical traps having the shape of a segment, ring, ellipse, arc, etc. [40, 41, 43]. Examples of the possible types of optical traps are presented in Fig. 4.

Surely, such intensity distributions and the corresponding optical traps can be successfully synthesised using the stationary diffraction optical elements (DOEs). However, due to the variety of shapes and sizes of biological objects it seems important to have the possibility to vary the shape and size of the trap in real time, depending of the trapped objects. The displacement, size and shape of the traps, produced by the focusing device, can be controlled very smoothly (in theory - continuously). This is due to such important feature of the LC focusing device, as the use of a solid electrode for creating the voltage distribution within the aperture limits, which allows the formation of a smooth continuous profile of the phase delay and the smooth change of the voltage distribution at the focusing device aperture at the expense of varying the potentials at the

contact electrodes. Practically, the possibility of smooth control of the ring size is limited by the discreteness of the controlling voltages, applied from the control unit, and can be improved by decreasing the discretization step. The possibility of continuous phase profile formation leads to the reduction of diffraction losses. Moreover, the device possesses sufficiently high radiation resistance: in the experiments the radiation power density, incident on the focusing device, approached 30 W/cm ^{2}.

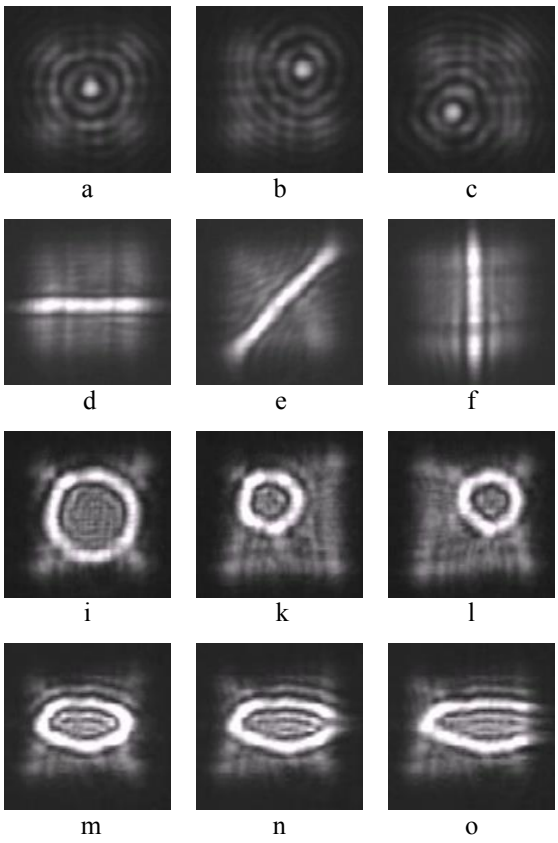


Fig. 4 Possible shapes of optical traps: controllable point traps (a-c), controllable trap in the form of a segment (d-f), ring trap (j-l), ellipse-shaped trap (m), C-shaped traps (n, o). The wavelength is 870 nm (a-f), and 650 nm (j-o).

As an example of using the compact optical tweezer based on the LC focusing device, let us present the results of the experiments, in which the *Saccharomy cescerevisiae* yeast cells suspended in water were used as the objects for micromanipulation, and the optical trap had the shape of an ellipse. The experiments were carried out at the radiation wavelength 532 nm. The radiation power in the optical trap amounted to 5.6 mW. The so called escape velocities were measured, i.e., the maximal velocities of the object stage motion for which the microobject remained to be captured by the optical trap. The measurements were performed with the displacement of the stage along the major semiaxis of the ellipse and along the minor one. Figure 4 presents the fragments of the video record, illustrating the capture and confinement of an individual yeast cell by the ring optical trap. The dependence of the escape velocity of the microobject upon its size for different directions of the displacement is presented in Table 1.

As seen from Table 1, the ellipse-shaped trap formed by means of the compact four-channel LC modulator allows the confinement of the trapped microobjects under the motion of the stage with the velocities of nearly 15 μm/s. If the dimensions of the trapped particle are smaller than the dimensions of the trap, then the shape of the trap plays an essential role. The escape velocity under the displacement along the minor semiaxis is greater than that in the case of moving along the major semiaxis (see the third row of Table 1). Similar results were obtained for trapping the latex microspheres with the diameter 2.4 μm. These particles were captured by the ellipse with the dimensions 3.9 μm × 4.8 μm. The escape velocity was 8.2±0.8 μm/s when moving along the major semiaxis of the ellipse and 14.0±1.4 μm/s when moving along the minor semiaxis.

Figure 6 presents the selected frames from a video record, demonstrating the possibility of capture and confinement of a relatively large particle. The object was the yeast cells, aggregated into a single particle with the dimensions 37 μm × 13 μm. The velocity of detachment of the object from the elliptic trap with the dimensions 4.8 μm × 4.2 μm for the displacement along its minor semiaxis amounted to 18.8±1.9 μm/s. The importance of manipulating large objects was repeatedly discussed in the literature [18, 44]. In biomedical applications this problem is related to the variety of sizes of the biological objects. The possibility of trapping and moving the microobjects larger than 10 μm by means of a contour trap will make it possible to avoid the nucleus damage when trapping the nucleated cells.

5 Conclusion

We demonstrate the scheme of a compact optical tweezer, in which the small-size semiconductor laser modules and small-size DPSS laser modules, including laser pointers, are used as a radiation source. It is shown that the use of the four-channel LC modulator (LC focusing device) in the scheme of the compact optical tweezer allows essential extension of its functional capabilities, namely, the formation of tuneable traps with a variety of shapes and the control of their position. The technological features of the four-channel LC modulator allow saving compactness and technological simplicity of the device. The operability of the compact laser manipulator with extended capabilities is demonstrated in the experiments with yeast cells.

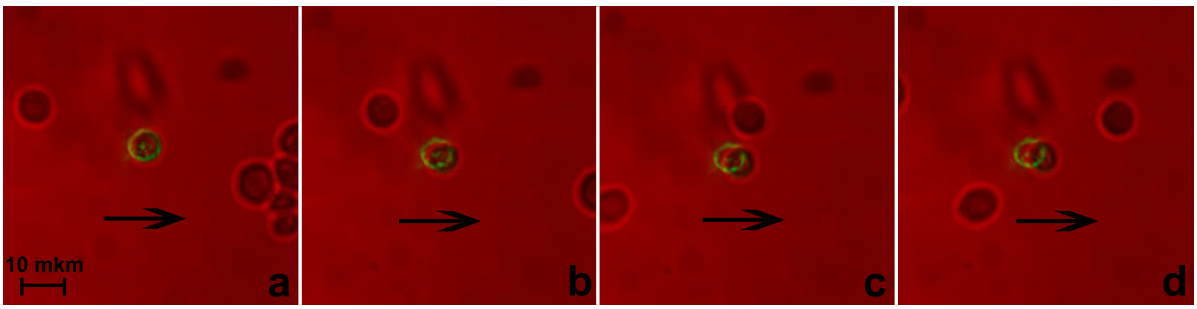


Fig. 5 Capture and confinement of a single *Saccharomy cescerevisiae* cell. The arrow shows the direction of the microscope stage movement.

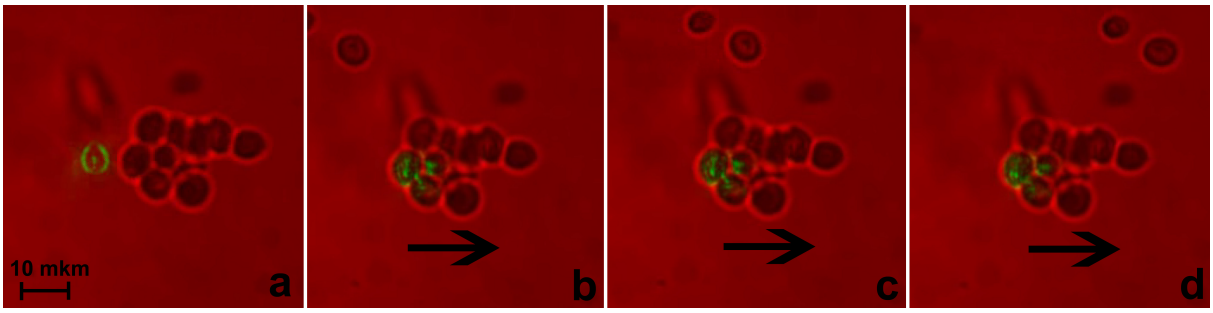


Fig. 6 Trapping and confinement of a large microparticle. The arrow shows the direction of the microscope stage movement.

Table 1 Escape velocities versus the size of the microobject (*Saccharomy cescerevisiae* yeast cells).

Particle size	Contour trap size	Escape velocity of the trap, μm/s	
		Displacement along the minor semiaxis	Displacement along the major semiaxis
5.0 μm × 5.6 μm	4.8 μm × 4.2 μm	15.3±1.5	15.0±1.5
4.9 μm × 6.3 μm		17.1±1.7	16.4±1.6
3.1 μm × 3.4 μm		16.7±1.7	12.7±1.3

Acknowledgments

This work was supported by the Russian Foundation for Basic Research (grant No. 14-02-31376), the Program for Basic Researchers of the Physical Sciences Department of RAS “Fundamentals and experimental realization of promising semiconductor lasers in the interests of industry and technology” and by the Ministry of Education and Science of the Russian Federation.

Backscattering spectroscopy for assessing skin tumor

Valery P. Zakharov[1], Pavel E. Timchenko[1*], Elena V. Timchenko[1], Larisa A. Zherdeva[1], Sergey. V. Kozlov[2], Alexander A. Moryatov[2]

[1] Samara State Aerospace University (SSAU), 34 Moskovskoye Shosse, Samara 443086, Russia

[2] Samara State Medical University, 89 Chapaevskaya str., Samara 443099, Russia

[*] **e-mail:** timpavel@mail.ru

Abstract. The results of in vitro backscattering spectral studies of 7 nevuses and 27 samples of different skin cancer are presented. The pathology type classification in the two-dimensional phase space formed by the scattering indices at the wavelengths 560 nm, 650 nm, 700 nm, and 760 nm scaled to the healthy skin scattering coefficient value is proposed. It is shown that the sensitivity and specificity of differentiation between the benign and malignant tumors exceeds 86% and 96%, respectively, and their value for selecting melanoma among other malignant tumors falls by 5-8% due to partial overlap of classes in the phase space. © 2015 Samara State Aerospace University (SSAU).

Keywords: Differential backscattering, discriminant analysis, tumor, noninvasive diagnostics, optical coefficient, melanoma, basal cell carcinoma, nevus.

Paper #2489 received 2015.05.05; revised manuscript received 2015.06.19; accepted for publication 2015.06.25; published online 2015.06.30.

References

1. L. V. Wang, "Skin cancer detection by spectroscopic oblique-incidence reflectometry: classification and physiological origins," Appl. Opt. 43, 2643–2650 (2004).
2. A. V. Novik, "Skin melanoma: novel approaches," Prakticheskaya onkologiya 1(12), 36–42 (2011).
3. M. Mogensen, and G. B. Jemec, "Diagnosis of nonmelanoma skin cancer/keratinocyte carcinoma: a review of diagnostic accuracy of nonmelanoma skin cancer diagnostic tests and technologies," Dermatol Surg 33(10), 1158–1174 (2007).
4. S. W. Fosko, W. Hu, T. F. Cook, et al., "Positron emission tomography for basal cell carcinoma of the head and neck," Arch Dermatol 139, 1141–1146 (2003).
5. V. P. Zakharov, K. V. Larin, and I. A. Bratchenko, "Increasing the informativity of optical coherence tomography in skin pathology diagnistics," Proceedings of SSAU 2(26), 232-239 (2011).
6. A. Alex, J. Weingast, B. Hofer, M. Eibl, M. Binder, H. Pehamberger, W. Drexler, and B. Povazay, "3D optical coherence tomography for clinical diagnosis of nonmelanoma skin cancers," Imaging Med 6, 653–674 (2011).
7. A. Scope, U. Mahmood, D. S. Gareau, M. Kenkre, J. A. Lieb, K. S. Nehal, M. Rajadhyaksha, "In vivo reflectance confocal microscopy of shave biopsy wounds: feasibility of intraoperative mapping of cancer margins," Br J Dermatol 163, 1218–1228 (2010).
8. J. Zhao, H. Lui, D. I. McLean, and H. Zeng, "Real-time Raman spectroscopy for noninvasive in vivo skin analysis and diagnosis," New developments in biomedical engineering 24, 455-474 (2010).
9. A. Garcia-Uribe, J. Zou, M. Duvic, J. H. Cho-Vega, V. G. Prieto, and L. V. Wang, "In Vivo Diagnosis of Melanoma and Nonmelanoma Skin Cancer Using Oblique Incidence Diffuse Reflectance Spectrometry," Cancer Res 72(11), 2738-2745 (2012).
10. J. de Leeuw, N. van der Beek, W. D. Neugebauer, P. Bjerring, and H. A. Neumann, "Fluorescence detection and diagnosis of non-melanoma skin cancer at an early stage," Lasers Surg Med 41(2), 96-103 (2009).
11. V. P. Zakharov, I. A. Bratchenko, O. O. Myakinin, D. N. Artemyev, D. V. Kornilin, S. V. Kozlov, and A. A. Moryatov, "Multimodal diagnostics and imaging of oncological pathologies," Quantum Electron 44(8), 726–731 (2014).
12. A. Pradhan, B. B. Das, K. M. Yoo, R. R. Alfano, J. Cleary, R. Prudente, and E. Celmer, "Time-resolved UV photoexcited fluorescence kinetics from malignant and non-malignant breast tissues," Proc. SPIE Conference 1599, 81–84 (1992).

13. C. Y. Wang, H. M. Chen, C. P. Chiang, C. You, and T. C. Hsiao, "Time-resolved autofluorescence spectroscopy for classifying normal and premalignant oral tissues," Lasers Surg. Med 37(1), 37–45 (2005).
14. P. V. Butte, B. K. Pikul, A. Hever, W. H. Yong, K. L. Black, and L. Marcu, "Diagnosis of meningioma by time resolved fluorescence spectroscopy," J. Biomed. Opt 10(6), 064026 (2005).
15. N. P. Galletly, J. Mcginty, C. Dunsby, F. Teixeira, J. Requejo-Isidro, I. Munro, D. S. Elson, M. A. A. Neil et al., "Fluorescence lifetime imaging distinguishes basal cell carcinoma from surrounding uninvolved skin," Br. J. Dermatol 159(1), 152–161 (2008).
16. J. Mcginty, N. P. Galletly, C. Dunsby, I. Munro, D. S. Elson et al., "Wide-field fluorescence lifetime imaging of cancer," Biomed. Opt. Express 1(2), 627–640 (2010).
17. R. Cicchi, A. Crisci, A. Cosci, G. Nesi, D. Kapsokalyvas, S. Giancane, M. Carini, and F. S. Pavone, "Time- and Spectral-resolved two-photon imaging of healthy bladder mucosa and carcinoma in situ," Opt. Express 18(4), 3840–3849 (2010).
18. X. He, K. Wang, and Z. Cheng, "In vivo near-infrared fluorescence imaging of cancer with nanoparticle-based probes," Nanomed Nanobiotechnol 2, 349–366 (2010).
19. G. Wagnieres, J. Mizeret, A. Strudzinski, and H. Van den Bergh, "Frequence-domain fluorescence lifetime imaging for endoscopic clinical cancer photodetection: apparatus design and preliminary results," J. Fluoresc. 7, 75-83 (1997).
20. A. Garcia-Uribe, E. B. Smith, M. Duvic, and L. V. Wang, "White light oblique-incidence diffuse reflectance spectroscopy for classification of in vivo pigmented skin lesions," Proc. SPIE 6435, 64350L (2007).
21. I. Kuzmina, I. Diebele, D. Jakovels, J. Spigulis, L. Valeine, J. Kapostinsh, and A. Berzina, "Towards non-contact skin melanoma selection by multi-spectral imaging analysis," J. Biomed. Opt. 16(6), 1-3 (2011)
22. A. J. Thompson et.al., "In vivo measurements of diffuse reflectance and time-resolved autofluorescence emission spectra of basal cell carcinomas," J. Biophotonics 5(3), 240–254 (2012).
23. P. J. Matts, P. J. Dykes, and R. Marks, "The distribution of melanin in skin determined in vivo, British Association of Dermatologists," British Journal of Dermatology 156, 620–628 (2007).
24. G. Z. A. Dimou, I. Bassukas, D. Galaris, A. T. E. Kaxiras, "Melanin absorption spectroscopy: new method for noninvasive skin investigation and melanoma detection," Journal of Biomedical Optics 13(1), 014017 (2008).
25. R. O. Duda, P. E. Hart, and D. G. Stork, Pattern Classification, 2nd Edition, Wiley (2000).
26. M. Mogensen et al., "Optical coherence tomography for imaging of skin and skin diseases," Semin. Cutan. Med. Surg. 28, 196 –202 (2009).

1 Introduction

The intensified impact of technology factors on man, the worsening of ecologic conditions, and the increase of the carcinogen air pollution lead to the growth of the number of skin oncologic diseases among the population, namely, basal cell carcinoma, squamous cell carcinoma and melanoma [1]. The latter kind of tumor is the most dangerous one, since its appearance is like that of the benign tumor (nevus), and the lately detected melanoma is hardly treatable and often is accompanied with the development of metastases. At early melanoma stages the depth of invasion is insignificant and the efficiency of its treatment is essentially higher [2].

A commonly accepted method of the tumor type assessment is the histologic analysis of a tissue sample taken for biopsy. In application to the skin oncologic diseases the histology is performed after the surgical operation and, therefore, the unambiguous information about the tumor type is absent at the moment of operation. This leads to the increased amount of surgical intervention due to the uncertain invasion depth, as well as to excess surgical operations of purely benign tumors [3].

In this connection it is an urgent problem to develop methods for high-efficiency express diagnostics of the neoplasm kind during the pre-surgery period, which can essentially reduce the numbers of recurrent tumours. For the noninvasive skin cancer diagnostics the application of biomedical imaging is known, such as PET [4], optical coherence tomography [5, 6], confocal microscopy [7]. However, the imaging methods are labour-consuming and expensive, and their application is reasonable for updating the already established diagnosis, planning and control of the treatment process.

The screening of skin oncologic diseases is most convenient using optical methods, e.g., Raman scattering [8], backscattering [9], and fluorescence analysis [10]. Due to small cross section the Raman scattering requires long signal acquisition time for random noise elimination, which hampers its mass application without combining with optical imaging methods [11]. As a rule, the fluorescence is excited with UV radiation [12, 13], because the strongest absorption lines of natural fluorochromes are in the UV region. The reliability of fluorescence diagnostics can be improved by using either the complicated methods of time-resolved fluorescence spectroscopy [14-16], or the multiphoton fluorescence analysis [17] using laser sources with high peak power of probing radiation. An alternative method of improving the fluorescence analysis efficiency is the gold nanoparticles injection [18]. Having a number of positive properties, the fluorescence methods suffer from limitations, they are unable to determine the true boundaries of the tumour

with enough precision and to assess the condition of perifocal zones surrounding the tumour without injection of artificial fluorochromes [19].

The application of reflection spectroscopy to the study of skin spectral properties [20] demonstrated the possibility to use it for the assessment of malignant and benign skin tumors [21, 22]. It was shown that the spectral intensity of backscattering essentially differs for the basal cell carcinoma and the adjacent healthy skin at the wavelengths 540 and 575 nm, corresponding to the haemoglobin absorption bands. This is due to the enhancement of capillary network in the tumor. This fact allowed to formulate a method for basal cell carcinoma differentiation based on the difference in spectral properties of the scattered radiation [22]. However, due to high variability of skin spectral properties in different patients [20, 23] the sensitivity of this method is insufficient for screening examination. The authors of Refs. [21, 24] proposed to use the difference in melanin absorption in the visible and near infrared spectral regions for the melanoma test. However, this approach does not allow differentiation of malignant melanoma from the benign nevus, since both are characterised by the increased melanin concentration.

The goal of the present paper is to develop the backscattering method for differentiation of tumors with the individual human skin features taken into account.

2 Experimental technique

The object of study were 27 samples of skin malignant tumors (12 melanomas, 5 samples of squamous cell carcinoma, and 10 samples of basal cell carcinoma) and 7 samples of benign skin tumor (pigment nevus). All samples were obtained after surgical resection in the State Health Institution Samara Regional Oncology Clinic (SHI SROC) and investigated according to the protocol, approved by the Bioethics Committee of Samara State Medical University. The tissue samples were kept in sterile boxes at +4 ± 2 °C and were tested not later than in four hours after resection. Each tumour examination was accompanied by histologic analysis for the final diagnosis. Alongside with the tumour region, in each sample the optical properties of healthy skin adjacent to the tumor region were also studied.

The registration and spectral analysis of radiation, scattered from the sample, were carried out using the experimental setup presented in Fig. 1. The broadband optical radiation, generated by the source 1, was supplied via the coupler 2 to the input 3 of the first receiver channel of the spectrometer 4 and via the fiber 5 onto the studied object 6. The light scattered from the sample 6 was collected and supplied via the fiber 7 to the second receiver channel of the spectrometer 4. The sample was attached to the microtransporter 8 with linear step motor 9. The control of the setup was performed from the personal computer 10.

The radiator 1 generated optical radiation in the spectral range from 300 to 1100 nm with the intensity maximum at 750 nm. The spectrograph 4 was the six-channel Shamrock SR-303i (focal length 303 mm) with integrated digital camera ANDOR DV-420A-OE (1024*256, 26 μm2, 16 bit), which provided the registration of the scattered radiation spectrum with the error ±0.2 nm in the entire spectral range of the radiation source. The fibers 5 and 7 were fastened at the distance 1 mm from each other and formed a singe fiber-optical unit placed at the height of 1 mm above the sample 6. The height was determined experimentally to provide the maximal backscattering signal intensity. The diameter of the light spot at the sample 6 for this height was about 1 mm. The use of microtransporter 8 allowed scanning the region of interest with the step 1 mm and the linear translation velocity 2 mm/s. This allowed rapid recording of the biotissue optical properties at 16 -25 points of the object of interest.

Simultaneous registration of incident (reference) and scattered (measuring channels 3 and 7 of the spectrometer 4) signal intensity allowed the elimination of power fluctuations of the source 2 and the thermal drift of its spectrum. For this aim at each moment of time the normalisation of the spectral density of scattered radiation to the spectral density recorded in the reference channel was carried out.

All experiments were carried out under similar temperature conditions, room illumination and setup geometry. To increase the signal-to-noise ratio the signal was accumulated during 0.2 s and smoothed using the median and averaging filters.

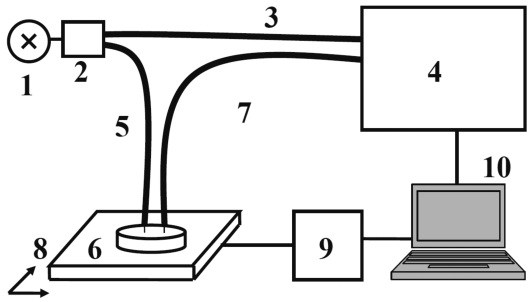


Fig. 1 Schematic diagram of the experimental setup: 1 – broadband radiation source, 2 -coupler, 3 – reference signal optical fiber, 4 – multichannel spectrometer, 5 – radiating fiber, 6 – object of study, 7 – diagnostic fiber, 8 – transporter, 9- step motor, 10 – computer.

3 Spectral differentiation of skin tumors

Let us introduce the scattering indices to characterise the skin optical properties at the point (x,y)

$$k(x,y)=\frac{I_{760}(x,y)}{I_{560}(x,y)},$$
$$m(x,y)=lg\left(I_{650}(x,y)\right)-lg\left(I_{700}(x,y)\right), \quad (1)$$

where $I_\lambda(x,y)$ is the intensity of scattering at the point (x,y) scaled to the intensity of the radiation source at the wavelength λ.

In fact the index k is related to the density of capillary network in dermis in the region of backscattering registration and the index m is proportional to the melanin concentration. As it is known [21], the tumor growth is accompanied by intense formation of capillary network that changes the skin optical properties in the region of tumor in the spectral regions of minimal and maximal haemoglobin absorption (the wavelengths 760 nm and 560 nm, respectively). And in the melanoma or nevus case the increase of the melanin concentration manifests itself in exponential decrease of the intensity in the spectral range 560-700 nm. In order to exclude the influence of hemoglobin content variations on melanin index m we use only near IR part of the range between wavelengths 650 nm and 700 nm.

On the other hand, the optical properties of the skin are individual, and the concentration of melanin and other pigments essentially changes depending on the skin type. In the experiments carried out the samples belonged to the skin type II – light (light-skin Europeans) and III – medium-light (dark European). To compensate the difference in coefficients (1) the coefficients measured in the tumour were scaled to the average value of these coefficients for normal skin

$$K(x,y)=\frac{k(x,y)}{\overline{k_{norm}}},\ M(x,y)=\frac{m(x,y)}{\overline{m_{norm}}} \qquad (2)$$

The averaged values of the coefficients k_{norm} and m_{norm} for the healthy skin were determined at 3-5 points located near the tumour at the distance 5-10 mm from its visible boundary.

Each measurement of the backscattered spectral intensity at the point (x,y) of the tumour can be presented by a point in the phase plane (K,M). Then the points located beyond the tumour will cluster about the centre with coordinates (1,1) in the phase plane, and the rest space corresponds to the tumor region.

In Fig. 2 each studied sample is presented by the point (K_{max}, M_{max}) that corresponds to the maximal deviation of the coefficients (2) from their averaged values in normal skin, i.e., from the phase point (1,1). Using the histologic analysis of the samples as the reference method, each experimental point in the phase plane (K, M) in Fig. 2 can be associated with a certain type of cancer or healthy tissue.

For selecting classes in the phase space (K,M) we used the canonical linear discriminant analysis [25]. The quality of approach was characterised by its sensitivity and specificity. Varying the class priorities one can shift the boundary line, achieving the required proportion of sensitivity and specificity.

The sequential discriminant analysis appeared to be the most efficient one (Table 1):

1. Selection of nevus (straight line 1) with the sensitivity 86% and specificity 96% from all cancer types - Class I.

2. Selection of basalioma (straight line 2) with the sensitivity 90% and specificity 94% from all studied malignant tumors – Class II.

3. Differentiation of melanoma (Class III) and squamous cell carcinoma (class IV) – the straight line 3.

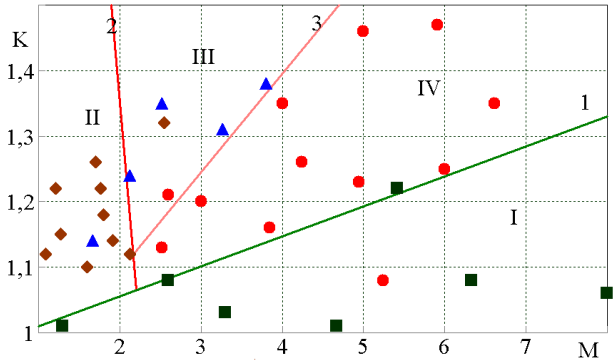


Fig. 2 Phase diagram for different types of skin cancers: nevus (square), basalioma (rhombus), squamous cell carcinoma (triangle), melanoma (circle). Class I – the region of nevus and normal skin, Class II – the region of basalioma, Class III—the region of squamous cell carcinoma, and Class IV – the region of melanoma.

4 Tumor boundary inedtification

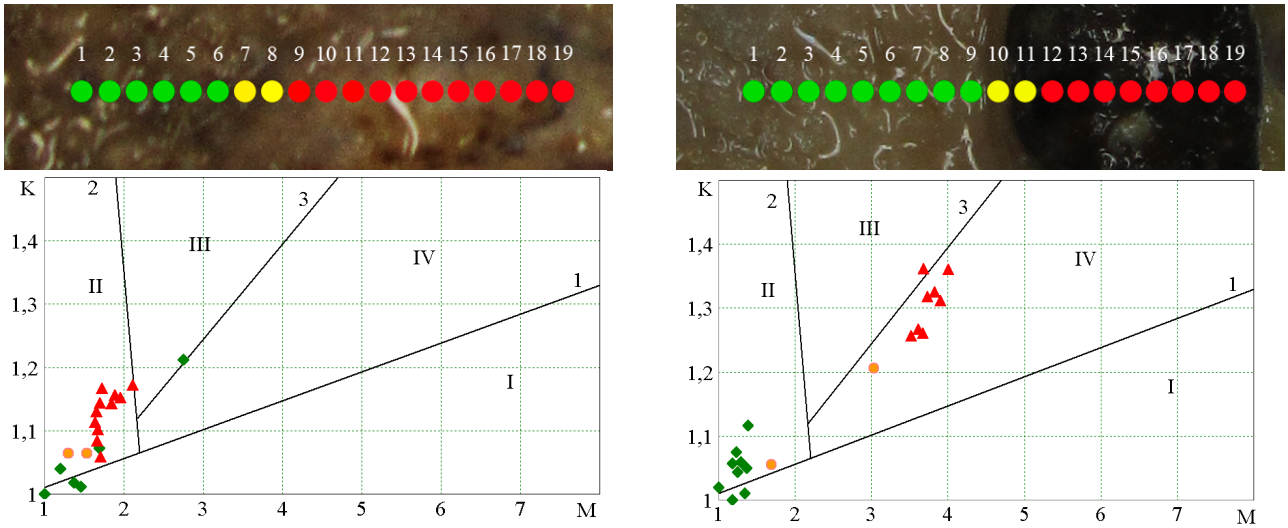
The proposed approach can be used not only for determining the cancer type, but also for rapid identification of its boundary. The latter is of particular importance when preparing for surgical operation, or observing in the course of chemotherapy treatment.

Figure 3 presents a typical pattern of distributions of optical characteristics in the phase plane (K,M) recorded at the points (x,y) along the tumour section for basalioma (a) and melanoma (b). In all experiments the scanning was performed starting from the region of definitely healthy skin, passing the tumor and reaching the healthy skin or the centre of inhomogeneity (in the case of sample excision). The scanning step is 1 mm, the diameter of focal spot of the optical radiation on the skin surface about 1.5 mm. The spectrum was recorded at 16—25 points for each experimental series.

It is seen that for basalioma the points corresponding to healthy skin lie either in the region belonging to class I (benign tumors) or near the point (1,1) in the region of Class II. As we move towards the tumour centre, the corresponding points in the phase plane move up along the axis K, while the value of M remains unchanged within the measurement error. This corresponds to the fact that for basalioma the melanin concentration changes weakly in comparison with that of the healthy skin adjacent to the tumour. On the contrary, for melanoma the increase of melanin concentration and density of capillaries is typical, as we move towards the tumour centre, which leads to the prolate distribution of the tumour points in the phase plane region belonging to Class IV. And the points corresponding to the healthy tissue are localised beyond the region of class IV, near

Table 1 Neoplasms classification.

Stage	Samples	Histology	Backscattering		Sensitivity	Specificity
			Region A	Region B		
1	A. Nevus	7	6	1	86%	96%
	B. Other neoplasms	27	1	26		
2	A. Basalioma	10	9	1	90%	94%
	B. Melanoma, squamous cell carcinoma	17	1	16		
3	A. Melanoma	12	10	2	83%	80%
	B. Squamous cell carcinoma	5	1	4		



a) Basal cell carcinoma b) Melanoma

Fig. 3 Distribution of scanning point in the two-dimensional plane of spectral indices (*K, M*) for basal cell carcinoma (a) and melanoma (b). The rest notations correspond to Fig. 2.

the line 1, separating the classes of malignant and benign tumors.

5 Conclusion

We propose a method for detection and classification of skin pathologies, based on differential analysis of backscattered spectral intensities with the individual features of the human skin optical characteristics taken into account. The approach allows differentiation of benign tumors from the malignant ones with high sensitivity and specificity. However, the classes of malignant tumors partially overlap in the phase plane of normalised scattering indices (K,M). This fact reduces the sensitivity of the malignant tumour type identification. For example, for melanoma the sensitivity is limited by 83% and the specificity by 80%. Thus, it was achieved the increase 7% for sensitivity and 5% for specificity in comparison with known methods [26]. The main reason for such enhancement of sensitivity and specificity is connected with better accuracy of two-dimensional phase space analysis and spectral normalization of optical indexes on their values in neighboring healthy skin, which exclude the influence of individual characteristics of skin associated with a sunburn or skin phenotype.

Generally, one can assert that the method of differential scattering allows the localisation of tumor boundary with the error about 1 mm, limited by the focusing spot size and the region of efficient scattering of the probing radiation.

With low probability of missing the disease and the personalisation of the analysis, this approach can be used in mass examinations of population. And the capability of precise boundary determination is important for both the treatment planning and the treatment efficiency skin cancer.

Acknowledgments

This research was supported by the Ministry of Education and Science of the Russian Federation.

The combination of optical coherence tomography and Raman spectroscopy for tissue characterization

Kokila D. Egodage[1], Sebastian Dochow[1,2], Thomas W. Bocklitz[1], Olga Chernavskaia[1], Christian Matthäus[1,2], Michael Schmitt[1,2], Juergen Popp[1,2*]

[1] Institute of Physical Chemistry and Abbe Center of Photonics, Friedrich-Schiller University Jena, Helmholtzweg 4, 07743 Jena, Germany

[2] Leibniz Institute of Photonic Technology Jena e.V., Albert-Einstein-Str. 9, 07745 Jena, Germany

[*] **e-mail:** juergen.popp@ipht-jena.de

Abstract. The visualization as well as characterization of diseased tissue are of vital diagnostic interest for an early diagnosis to increase patients' survival rate. In this study we introduce an imaging device combining optical coherence tomography (OCT) and Raman spectroscopy (RS), allowing to record 2D and 3D OCT cross sectional images of bulk tissue samples, as well as the acquisition of Raman spectra from small areas of interest in order to aid the detection process with molecular information. The design of the OCT/RS imaging device consists of commercially available cage components. The probe head involves a CCD camera chip for visualization purposes and galvanic mirrors for scanning the sample in x and y directions with a scan line rate up to 76 kHz. The OCT/RS imaging approach has been successfully evaluated by investigating pork samples. OCT and Raman data were correlated and different tissue types within the samples were successfully identified and clustered separately. Finally, pork skin samples with visual defects were characterized. Overall, the presented OCT/RS device allows for recording of large morphological overview OCT images to define points of interest, which are afterwards characterized in more detail on a molecular level by means of Raman spectroscopy. © 2015 Samara State Aerospace University (SSAU).

Keywords: optical coherence tomography, Raman spectroscopy, probe, multimodal imaging.

Paper #2503 received 2015.06.20; revised manuscript received 2015.06.29; accepted for publication 2015.06.30; published online 2015.06.30.

References

1. A. Alwan, "Global status report on noncommunicable diseases 2010," Italy: World health organization (2011).
2. S. Edge, D. R. Byrd, C. C. Compton, A. G. Fritz, F. L. Greene, and A. Trotti, "Cancer Staging Manual," AJCC 7 (2010).
3. M. Kerkhof, H. Van Dekken, E. W. Steyerberg, G. A. Meijer, A. H. Mulder, A. De Bruïne, et al., "Grading of dysplasia in Barrett's oesophagus: substantial interobserver variation between general and gastrointestinal pathologists," Histopathology 50, 920-927 (2007).
4. L. Y. Robles, S. Singh, and P. M. Fisichella, "Emerging enhanced imaging technologies of the esophagus: spectroscopy, confocal laser endomicroscopy, and optical coherence tomography," Journal of Surgical Research 195, 502-514 (2015).
5. O. Old, M. L. Almond, R. Griggs, G. R. Lloyd, J. Horsnell, C. Kallaway, L. Fullwood, K. Das, J. Hutchings, M. Isabelle, C. Kendall, N. Stone, and Hugh Barr, "In Vivo Optical Imaging of Early Cancer and Tumours," in In Vivo Optical Imaging. Vol. 1, W. Liu (Ed.), OMICS Group, California (2014).
6. E. de Boer, N. J. Harlaar, A. Taruttis, W. B. Nagengast, E. L. Rosenthal, V. Ntziachristos, et al., "Optical innovations in surgery," British Journal of Surgery 102, e56-e72 (2015).
7. M. Mogensen, T. M. Joergensen, B. M. NÜRnberg, H. A. Morsy, J. B. Thomsen, L. Thrane, et al., "Assessment of Optical Coherence Tomography Imaging in the Diagnosis of Non-Melanoma Skin Cancer and

Benign Lesions Versus Normal Skin: Observer-Blinded Evaluation by Dermatologists and Pathologists," Dermatologic Surgery 35, 965-972 (2009).
8. V. R. Korde, G. T. Bonnema, W. Xu, C. Krishnamurthy, J. Ranger-Moore, K. Saboda, et al., "Using optical coherence tomography to evaluate skin sun damage and precancer," Lasers in Surgery and Medicine 39, 687-695 (2007).
9. T. Gambichler, A. Orlikov, R. Vasa, G. Moussa, K. Hoffmann, M. Stücker, et al., "In vivo optical coherence tomography of basal cell carcinoma," Journal of Dermatological Science 45, 167-173 (2007).
10. J. M. Olmedo, K. E. Warschaw, J. M. Schmitt, and D. L. Swanson, "Optical coherence tomography for the characterization of basal cell carcinoma in vivo: A pilot study," Journal of the American Academy of Dermatology 55, 408-412 (2006).
11. N. D. Gladkova, G. A. Petrova, N. K. Nikulin, S. G. Radenska-Lopovok, L. B. Snopova, Y. P. Chumakov, et al., "In vivo optical coherence tomography imaging of human skin: norm and pathology," Skin Research and Technology 6, 6-16 (2000).
12. L. Themstrup, C. A. Banzhaf, M. Mogensen, and G. B. E. Jemec, "Optical coherence tomography imaging of non-melanoma skin cancer undergoing photodynamic therapy reveals subclinical residual lesions," Photodiagnosis and Photodynamic Therapy 11, 7-12 (2014).
13. K. Jina, B. William, R. M. Jason, L. Howard, and W. Adam, "Functional optical coherence tomography: principles and progress," Physics in Medicine and Biology 60, R211 (2015).
14. H. Ra, E. González-González, M. J. Uddin, B. L. King, A. Lee, I. Ali-Khan, et al., "Detection of Non-Melanoma Skin Cancer by in vivo Fluorescence Imaging with Fluorocoxib A," Neoplasia 17, 201-207 (2015).
15. J. B. Ross, D. Huh, L. B. Noble, and S. F. Tavazoie, "Identification of molecular determinants of primary and metastatic tumour re-initiation in breast cancer," Nat Cell Biol 17, 651-664 (2015).
16. S. Dochow, D. Ma, I. Latka, T. Bocklitz, B. Hartl, J. Bec, et al., "Combined fiber probe for fluorescence lifetime and Raman spectroscopy," Analytical and Bioanalytical Chemistry, doi://10.1007/s00216-015-8800-5 (2015).
17. C. Krafft, S. Dochow, I. Latka, B. Dietzek, and J. Popp, "Diagnosis and screening of cancer tissues by fiber-optic probe Raman spectroscopy," Biomedical Spectroscopy and Imaging 1, 39-55 (2012).
18. E. Drakaki, T. Vergou, C. Dessinioti, A. J. Stratigos, C. Salavastru, and C. Antoniou, "Spectroscopic methods for the photodiagnosis of nonmelanoma skin cancer," Journal of biomedical optics 18, 061221 (2013).
19. K. Eberhardt, C. Stiebing, C. Matthäus, M. Schmitt, and J. Popp, "Advantages and limitations of Raman spectroscopy for molecular diagnostics: an update," Expert Review of Molecular Diagnostics 15, 773-787 (2015).
20. C. Krafft, B. Dietzek, M. Schmitt, and J. Popp, "Raman and coherent anti-Stokes Raman scattering microspectroscopy for biomedical applications," Journal of Biomedical Optics 17, 0408011 (2012).
21. P. C. Ashok, B. B. Praveen, N. Bellini, A. Riches, K. Dholakia, and C. S. Herrington, "Combined information from Raman spectroscopy and optical coherence tomography for enhanced diagnostic accuracy in tissue discrimination," in Biomedical Vibrational Spectroscopy VI: Advances in Research and Industry, 89390L (2014).
22. K. Kong, C. J. Rowlands, S. Varma, W. Perkins, I. H. Leach, A. A. Koloydenko, et al., "Diagnosis of tumors during tissue-conserving surgery with integrated autofluorescence and Raman scattering microscopy," Proceedings of the National Academy of Sciences 110, 15189-15194, (2013).
23. M. Calin, S. V. Parasca, R. Savastru, M. Calin, and S. Dontu, "Optical techniques for the noninvasive diagnosis of skin cancer," Journal of Cancer Research and Clinical Oncology 139, 1083-1104 (2013).
24. C. Krafft, B. Dietzek, and J. Popp, "Raman and CARSmicrospectroscopy of cells and tissues," Analyst 134, 1046-1057 (2009).
25. J. Popp, M. Schmitt, B. Dietzek, C. Krafft, R. Möller, and P. Rösch, "Raman meets medicine: Raman spectroscopy: a powerful tool in biophotonics,", 75030N (2009).
26. P. C. Ashok, B. B. Praveen, N. Bellini, A. Riches, K. Dholakia, and C. S. Herrington, "Multi-modal approach using Raman spectroscopy and optical coherence tomography for the discrimination of colonic adenocarcinoma from normal colon," Biomedical Optics Express 4, 2179-2186 (2013).
27. C. A. Patil, N. Bosschaart, M. D. Keller, T. G. van Leeuwen, and A. Mahadevan-Jansen, "Combined Raman spectroscopy and optical coherence tomography device for tissue characterization," Optics Letters 33, 1135-1137 (2008).
28. C. A. Patil, J. Kalkman, D. J. Faber, J. S. Nyman, T. G. van Leeuwen, and A. Mahadevan-Jansen, "Integrated system for combined Raman spectroscopy–spectral domain optical coherence tomography," Journal of Biomedical Optics 16, 011007 (2011).
29. C. A. Patil, H. Kirshnamoorthi, D. L. Ellis, T. G. van Leeuwen, and A. Mahadevan-Jansen, "A clinical instrument for combined raman spectroscopy-optical coherence tomography of skin cancers," Lasers in Surgery and Medicine 43, 143-151 (2011).

30. S. Narendran, Q. Ji, D. Y. Eric, J. L. Alexander, C. L. Dina, E. P. Raphael, et al., "Line-scan Raman microscopy complements optical coherence tomography for tumor boundary detection," Laser Physics Letters 11, 105602 (2014).
31. J. A. Izatt, and M. A. Choma, "Theory of Optical Coherence Tomography," in Optical Coherence Tomography, W. Drexler, and J. Fujimoto (Eds.), Springer, Berlin Heidelberg, 47-72 (2008).
32. T. Bocklitz, A. Walter, K. Hartmann, P. Rösch, and J. Popp, "How to pre-process Raman spectra for reliable and stable models?" Analytica Chimica Acta 704, 47-56 (2011).
33. C. G. Ryan, E. Clayton, W. L. Griffin, S. H. Sie, and D. R. Cousens, "SNIP, a statistics-sensitive background treatment for the quantitative analysis of PIXE spectra in geoscience applications," Nuclear Instruments and Methods in Physics Research Section B: Beam Interactions with Materials and Atoms 34, 396-402 (1988).
34. J. Zhao, H. Lui, D. I. McLean, and H. Zeng, "Real Time Raman Spectroscopy for Noninvasive in vivo Skin Analysis and Diagnosis," in Recent Advances in Biomedical Engineering, In-tech, Vienna, Austria, 455-474 (2010).

1 Introduction

Cancer is one of the leading causes of death [1]. The specific type and grade of tumors are of vital interest to determine the appropriate medical treatment for cancer patients. The term benign is given to tumors when they do not have the tendency to spread whereas cancerous refers to those that may spread and develop tumors in other parts of the body (metastasis). This grading system, which is essential for further treatment depends mainly on the location, size and growth of the tumor as well as on the extent of cancer invasion into the lymph system (nodes) or on metastasis. Based on the tumor grading further treatments such as surgery, chemo- or radiation therapy will be evaluated [2]. Since grading is crucial, well qualified histopathologists conduct assessments which are subjective and can have a large interoperator variation [3]. Endoscopy has not been satisfactory for an accurate disease detection [4]. Currently existing imaging techniques such as wide-field detection, often coupled with fluorescence and staining agents, have low specificity and/or sensitivity. Confocal microscopy on the other hand allows cellular information but it is time consuming and requires training. Elastic scattering spectroscopy is under development but it requires many spectral acquisitions and might have a low accuracy to precede clinical trials [5].

New non-invasive imaging strategies are required for an intraoperative tumor grading i.e. for differentiation between tissue types and providing valuable visual information especially about the depth of tumor penetration and dimensions. Within the last years optical coherence tomography (OCT) has shown its potential for optical guidance during surgeries [6]. For example, OCT is able to identify non-melanoma skin cancers and pre-cancers *in vivo* [7, 8]. In the case of basal cell carcinoma OCT images were successfully correlated with histopathological data [9-12]. Apart from OCT providing morphological information [13] spectroscopic approaches such as fluorescence imaging [14, 15], fluorescence lifetime imaging [16] and Raman spectroscopy [17] allow for retrieving molecular tissue information and therefore offer the potential for tumor grading [18]. Especially Raman spectroscopy has been proven as a powerful spectral histopathological tool for taking optical biopsies without the need for extraction of samples from patients [19, 20]. Thus, tumor grading and identification of tumor types [21-23] can be applied based on the acquired Raman data. For a large variety of different cancer types, such a Raman-based spectral histopathology has been demonstrated in literature [24, 25]. However, the major drawback of Raman spectroscopy is its low sensitivity resulting in acquisition times of several seconds per spectrum hindering imaging large areas. Therefore, the combination of a highly specific technique such as Raman spectroscopy with a fast "red flag technique" such as OCT is desirable. This combination is able to locate tissue borders or suspicious regions based on OCT imaging which are subsequently chemically analyzed by Raman spectroscopy. Such a combination features the scanning speed of OCT imaging and the specificity of Raman spectroscopy. Previous work on the combination of Raman spectroscopy and OCT using chemometry has proven to be promising and shows higher classification accuracies although the measurements were carried out on separate instruments [26].

The combination of OCT and Raman spectroscopy was pioneered by the group Anita Mahadevan-Jansen [27, 28, 29]. Within their research, different wavelengths for both modalities were chosen i.e. 785 nm excitation for Raman spectroscopy and 855 nm central wavelength for OCT which enabled the use of a single detector for both spectral regions [28]. In general a high penetration and imaging depth is desirable for detecting tumor margins since deeper structures need to be resolved as seen in skin cancer [29, 30]. Therefore, the OCT/RS approach presented in the following utilizes a spectrometer based system with 1325 nm central excitation wavelength for OCT. The OCT system achieves an imaging depth of 7 mm in air and ~ 2.5 mm in tissue limited by the radiation penetration depth. The presented OCT/RS setup has been implemented with commercially available parts only. Several imaging objective lenses were characterized with respect to their feasibility in terms of throughput

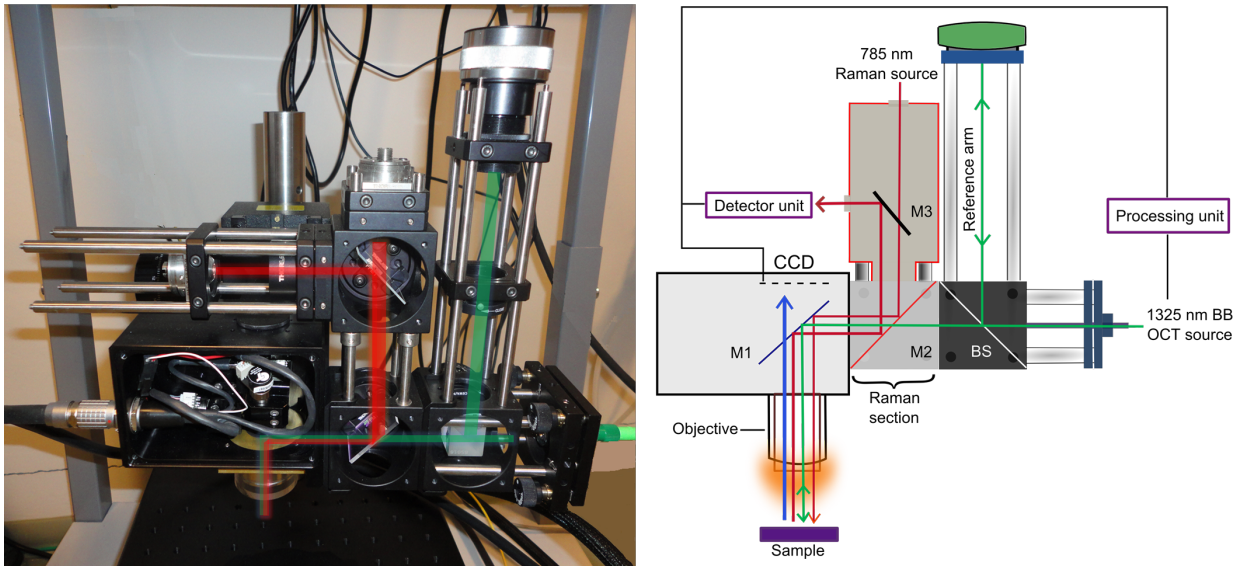


Fig. 1 Photograph of the OCT/RS system, where the different beam paths are visualized (A) and sketch of the combined OCT/RS system (B). M1, M2 and M3 represent the mirrors and BS denotes the beam splitter cube.

and background signals for both modalities. To demonstrate the feasibility of the OCT/RS setup for skin measurements different pork skin samples were analyzed.

2 Method

2.1 Raman spectrometer system

A Raman spectrometer (RAMAN RXN1, Kaiser Optical systems, USA) equipped with a 785 nm multimode laser source (Invictus^{TM} 785-nm NIR laser, Kaiser Optical Systems, Inc.,) was used. Measurements with the tested objective lenses (see section 3.2) resulted in an output laser power of ~ 40 mW at the sample plane which was kept constant for all experiments. The integration time was 1 second during all experiments. The Stokes scattered Raman light was dispersed by a *HoloPlex*, holographic transmission volume grating and imaged on a CCD camera (Andor iDus 420 BB-DR).

2.2 OCT system

The spectral domain (SD) OCT device from Thorlabs (TelestoII 1325 LR) is equipped with a 1325 nm broadband superluminescent diode (SLD), with a bandwidth of 200 nm. The excitation wavelength of 1325 nm allows for deep tissue penetration due to low scattering effects [31]. The reference arm, objective, CCD for recording visual images and the scanning optics are all integrated into a probe head, which will be explained in detail in the next section. The ThorImage OCT software was used to view and to adjust the image contrast of 3D surface images post acquisition. The device is capable of taking A- (single point), B- (line) and C- (3D volumetric) scans.

2.3 OCT probe head

The OCT probe head consists of a galvanic scanning unit, an objective or an achromatic doublet lens (see section 3.2) surrounded by an LED illumination ring for better visualization of the sample and a reference arm. The galvanic scanning unit consists of two scanning mirrors (M1 in Fig. 1B) for beam positioning in the x-y sample plane. The ‘slow’ scanning mirror was modified that it transmits visible light received from the sample onto a CCD chip in order to be able to record visual images. The second ‘fast’ galvanic mirror was used to scan the other coordinate of the x-y sample plane. The OCT source and spectrometer are coupled to the probe head by a FC/APC fiber. The light from the super luminescent diode (SLD) is collimated and directed to a beam splitter cube (BS in Fig. 1B) where the beam is split 50/50 into the sample and reference beam. The sample beam is directed to the galvanic scanning unit and then passes the objective. The back reflected sample light is collected through the objective, merged with the light from the reference arm and recoupled into the FC/APC fiber towards the OCT spectrometer. The optimum OCT reference intensity is regulated with the variable aperture placed in the reference arm.

2.4 OCT/Raman device implementation

In order to combine both OCT and Raman spectroscopy we used a probe cage consisting of the OCT components from Thorlabs (see sections 2.2 and 2.3) which was modified to incorporate the Raman modality (see Fig. 1A).

We have separated the OCT and Raman beam paths using dichroic mirrors at certain junctions where both beam paths cross (see Fig. 1B):

- M 1 (AHF Analysentechnik, Tübingen, Germany) represents two galvo scanning mirrors one of which is a dichroic mirror allowing visible light (~ 350 – 650 nm, blue arrow, Fig. 1B) to pass to the inspection CCD while reflecting 700 – 1500 nm with reflectivities higher than 93% (see Fig. 1B).

- M 2 (AHF Analysentechnik, Tübingen, Germany) redirects the Raman excitation and collection (750 – 1050 nm) onto the OCT beam path while remaining the OCT path unchanged. (Fig. 1B)

- M 3 (AHF Analysentechnik, Tübingen, Germany) separates the back reflected Raman signal from the Raman laser source. (Fig. 1B)

The alignment procedure proceeded with first aligning the OCT beam path such that the OCT laser beam was collimated onto the optical axis of the beam splitter cube and the reference arm (green beam path in Fig. 1A). Then mirror 2 was inserted and aligned such that the Raman beam path overlaps with the OCT beam path (overlaid beam path in Fig. 1A). Finally mirror 3 was aligned using a neon calibration lamp to achieve highest collection efficiencies (red beam path, in Fig. 1A). The reference arm length was adjusted according to the objective lens used (see section 3.2).

3 Experimental Section

3.1. Sample preparation

For a first validation of both subsystems (OCT and Raman) commercially available pork loin of ~ 1 cm thickness consisting of bone, fat and muscle tissue regions was used as a test sample. The pork loin sample was placed on a petri dish and characterized by the combined Raman – OCT (OCT/RS) system. For each measurement a freshly sectioned sample was used. A customized Labview program was used to scan a 10 x 10 mm pork loin sample to obtain a 3D OCT surface image by acquiring B-scans at sagittal sections. Subsequently the selected sample area was scanned with RS using 100 x 100 pixels with an integration time of 1 second per pixel. These measurements allow for a comparison between different objective lenses (see sections 3.2 and 4.1). The depth resolution achieved for the tested objective lenses (see section 3.2 and 4.1) was compared by analyzing B-scans of scotch tape. Finally pork skin samples with visual defects were used for realistically simulating skin measurements. These samples were extracted from pork belly, which was made for consumption.

3.2. Objective lenses

The two modalities OCT and Raman have contrary optical demands. While deep tissue OCT imaging requires long distance objectives with a rather low numerical aperture, Raman-spectroscopy on the other hand relies on high numerical apertures to achieve high collection efficiencies. The perfect objective for combining OCT and Raman measurements is therefore always a tradeoff between both modalities. However, for both cases an anti-reflection coating transmitting wavelengths from 700 – 1500 nm is advantageous. Initially we tested the following three different commercially available microscope objectives specially designed for OCT imaging systems and optimized for IR-OCT imaging:

- LSM02: Thorlabs, f = 18 mm, NA = 0.11, magnification of 10x, working distance 7.5 mm

- LSM03: Thorlabs, f = 36.0 mm, NA = 0.056, magnification of 5x, working distance 25.1 mm

- LSM04: Thorlabs, f = 54.0 mm, NA = 0.037, magnification of 3x, working distance 42.0 mm.

Additionally an achromatic doublet lens (35mm-NIRII; Edmund optics, US) with AR coating was tested, all with respect to achieve optimum Raman intensities, low Raman backgrounds as well as clear OCT images (see section 4.1). The three objectives are telecentric, which ensures minimal image distortions and a constant image resolution due to the spot size being constant in the flat image plane while scanning. Each time the objective was changed, the reference arm length was adjusted accordingly. In addition the probe head was calibrated for each objective prior to the measurement.

3.3. Data analysis

The analysis of the Raman spectra was carried out according to a standard protocol recently developed in our group [32]. First a wavenumber calibration was carried out based on Paracetamol as wavenumber standard. Thereafter, a baseline subtraction with the SNIP algorithm [33] was applied and a vector-normalization was performed. As analysis procedure, a k-means cluster analysis with k = 5 was applied in order to highlight spectral changes within the dataset. This k-means cluster analysis was carried out to allow for a comparison between the white light image, OCT scan and the Raman data. In general the generation of the false-color Raman images is not necessary and single point measurements are sufficient. Here Raman images were only generated to verify that with the measurement system, OCT and Raman images can be recorded for the same field-of-view. In future clinical applications, Raman spectra will be collected pointwise from regions of interest identified by a large OCT image.

4 Results and discussion

4.1 Objective lens comparison

As mentioned in section 3.2. OCT has contrary demands as compared to Raman spectroscopy with respect to the applied objective lenses. For Raman spectroscopy the applied objectives should show a good collection efficiency as well as a low Raman background signal, enabling cluster algorithms to differentiate different tissue types. To quantify the applicability of all objective lenses introduced in section 3.2 pork loin samples consisting of bone, muscle and fat tissue were measured and analyzed with both modalities. Fig. 2 shows OCT and Raman measurements recorded with

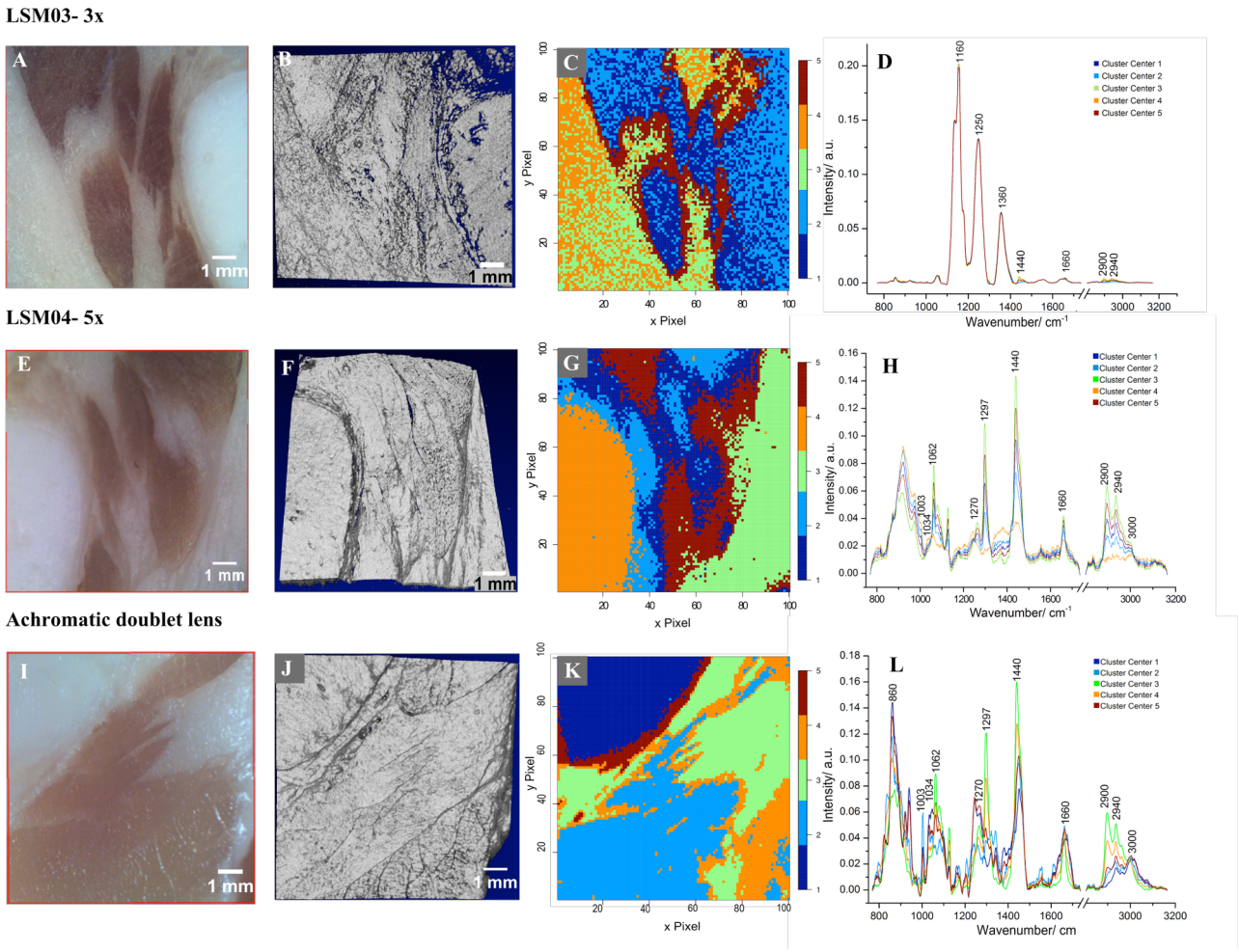


Fig. 2 Evaluation of different objective lenses (see section 3.2) for combined OCT/Raman measurements using pork loin samples. The rows are representing the results for each individual objective lens. The first column shows the microscopic white light images of the sample area (A, E, I). The second column shows the OCT C-scan as seen from the surface (B, F, J). The third row shows the k-means cluster image derived from the Raman raster scan of the same area (C, G, K) and the right row shows the corresponding cluster mean Raman spectra (D, H, L).

the two objectives (LSM03 and LSM04) and the achromatic doublet lens described in section 3.2. The objective LSM02 exhibiting the highest numerical aperture of all commercially available OCT objectives and therefore representing the best tradeoff for both modalities, had to be excluded from the study since it only transmits 10 % of the 785 nm Raman excitation laser. Fig. 2 shows white light images acquired with the probe head (left column), the corresponding top view C-Scans from the same area (second column), the resulting k-means Raman cluster images from raster scans of that area (third column) and the corresponding mean Raman spectra for each cluster (right column) for the two objectives LSM03, LSM04 and the achromatic doublet lens.

The white light images recorded with all three objective lenses highlight the sample distribution of fat, bone and muscle tissue. It is worth mentioning here, that the used galvanic mirror reflecting all wavelength higher than 650 nm has an impact on the sample image quality in a way that the red channel intensity is reduced, which will be also important for the experiments reported in section 4.3. The OCT C-Scans contain the complete volumetric 3D information of the tissue but are here displayed as 2D top view images for a better comparison with the morphology displayed in the white-light images. Both modalities (OCT and white light) show a good agreement with respect to the sample morphology.

The Raman spectra recorded with LSM03 show large Raman background signals of the objective itself that disturb the Raman spectra of the sample i.e. an overlap with the Raman bands that are particularly important for the differentiation between different tissue types. Here the clusters 3 and 4 displayed in Fig. 2 C seem to be distributed throughout the regions consisting of fat, while the clusters 1 and 2 can be mainly found within the muscle and bone regions. Cluster 5 depicts the meat- fat boundary. The three very intense Raman bands at 1160, 1250 and 1360 cm^{-1} observed when using the LSM03 objective (Fig. 2D) are most probably due to organic compounds present in the optical glue of the objective itself. Moreover, the loss of laser power due to the objectives is quite significant and only 30%

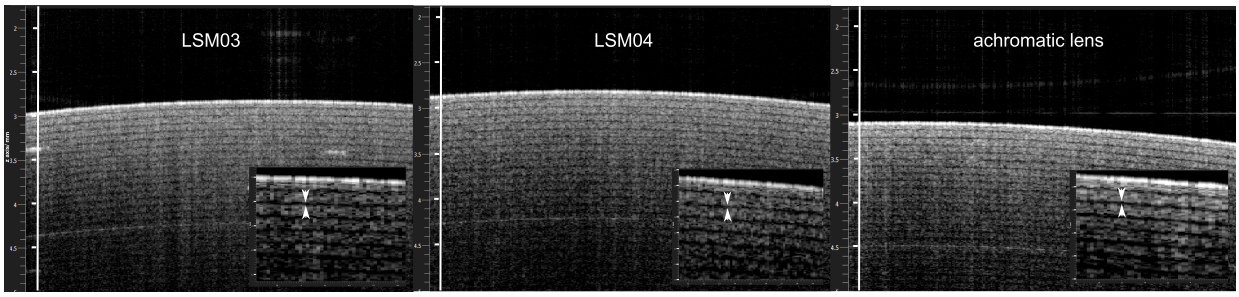


Fig. 3 Comparison of the axial resolution using scotch tape as a test sample with LSM03, LSM04 and the achromatic lens doublet as objective lenses. Inset: the adhesive in between tape layers was measured to be ~10µm shown by the white arrows.

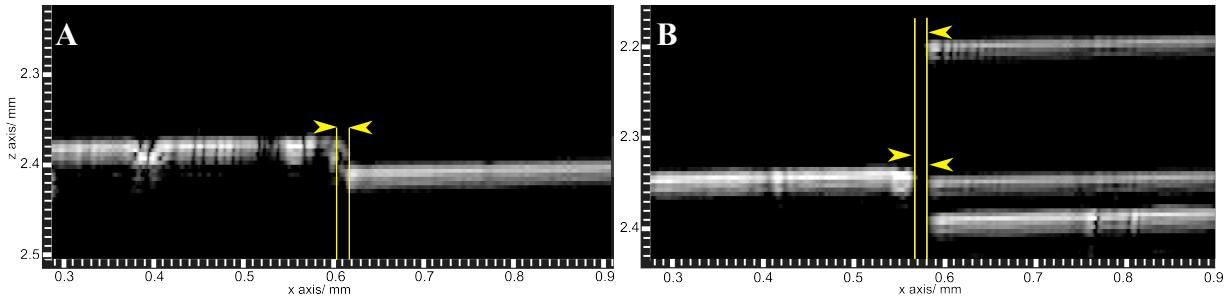


Fig. 4 B-scans of tape on a glass slide (A) and glass cover slip on a glass slide (B) to determine the lateral resolution of OCT in combination with the achromatic doublet. The mismatch of the proximal and distal surfaces shown by the yellow arrows was found to be 13 µm in both cases.

of the Raman excitation power is transmitted to the sample. These results clearly show that the objective LSM03 is not suitable for combined OCT/Raman measurements.

The microscope objective LSM04 shows only minimal background Raman signatures (see Fig. 2H) due to the objective itself and therefore leads to more significant Raman images (see Fig. 2G) as compared to LSM03. The application of LSM04 allows for clustering bone, fat and muscle tissues. The k-means Raman cluster image clearly correlates with the white-light and the OCT image (Figs. 2 E-G). Fig. 2G shows that cluster 1 relates to muscle tissue. The transition region between fat and muscle is separated by cluster 2 displayed in cyan. Bulk fat is highlighted by cluster 3 in green and bone is denoted by the 4th cluster plotted in orange. However, the overall transmission of the Raman excitation laser for this objective LSM04 is only 25%. This low transmission in combination with the rather low numerical aperture leads to a signal to noise ratio of 64.3 (calculated for the Raman peak at 1440 cm^{-1}, Fig. 2 H).

The achromatic doublet lens has a transmission loss of only 10% of the Raman excitation laser and therefore a much higher transmission for the whole Stokes Raman scattered light between 785 to 1050 nm as compared to the two microscope objectives LSM03 and LSM04. Therefore the achromatic doublet lens shows a good Raman collection efficiency while exhibiting the same numerical aperture than LSM03. The k-means cluster image (Fig. 2K) recorded with the achromatic doublet lens shows that all the pork tissue components can be better differentiated than for the LSM objectives. This is directly linked to the higher signal to noise ratio of the acquired Raman spectra. One drawback when using the doublet lens was that it prevented the ThorImage software from conducting its image calibration accurately. However, due to its superior Raman performance while simultaneously maintaining the quality of OCT scans, this achromatic doublet lens represents a very suitable tradeoff for both subsystems i.e. Raman and OCT. Overall, the SNR achieved with the doublet lens (SNR= 248.5) is 4 time better than the SNR obtained with the LSM04 (SNR= 64.3).

The axial resolution of the OCT subsystem is only dependent on the source bandwidth and the OCT-spectrometer resolution. These two properties do not depend on the applied objectives as can be seen in Fig. 3 where we analyzed B-scans of scotch tape.

Figure 3 shows that all three objective lenses exhibit a comparable depth resolution. Therefore, the achromatic lens doublet was chosen as the best suited objective lens for combining OCT and Raman. The following system characterization measurements were performed with the achromatic doublet lens only.

The lateral resolution of the OCT part in combination with the achromatic doublet lens was characterized by B-scans over a 50 µm tape, which was placed on a glass slide with the assumption that the tape has a straight edge. The resulting mismatch between the proximal and distal surfaces of the tape was found to be about 13 µm (Fig. 4 A).

In order to confirm this lateral resolution determined for the tape, a glass cover slide was also placed on a

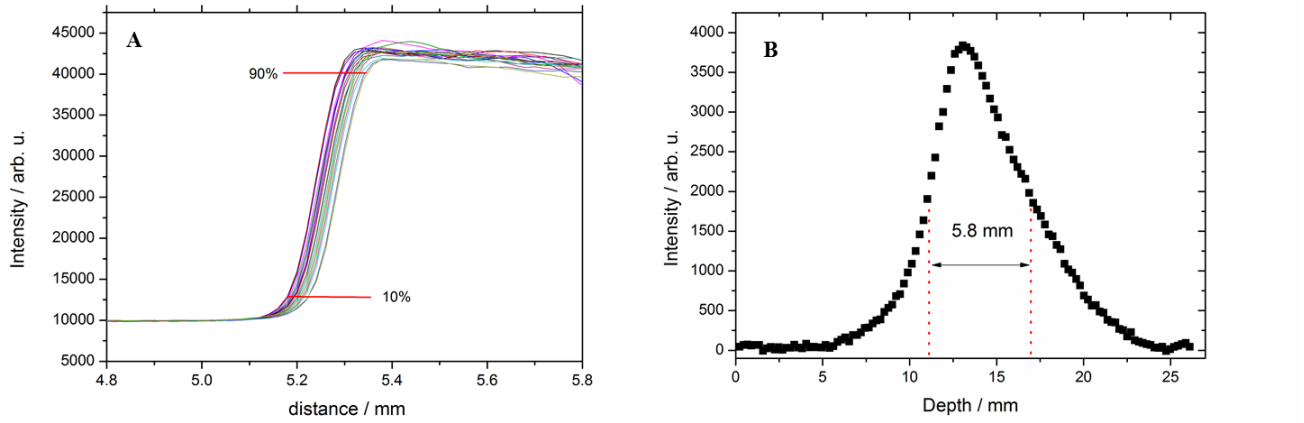


Fig. 5 Lateral resolution measured between 10 and 90% of the integrated Teflon Raman peak at 338cm^{-1} (A) of a Teflon layer and depth of field measurement (B) measured for a Raman peak at 493 cm^{-1} for scotch tape.

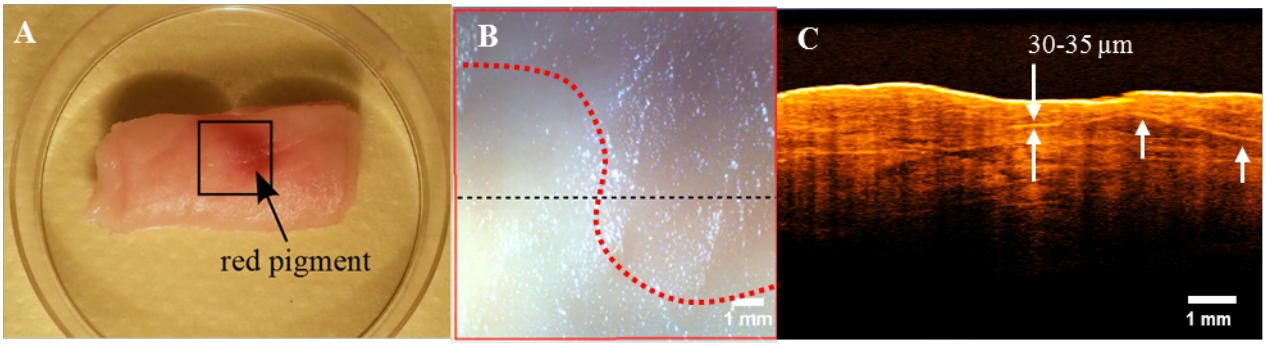


Fig. 6 Pork skin with a red pigment (A), zoom into a 10x10 mm region of interest (B) and a B-scan of the dashed red line shown in B emphasizing the position of the red pigment within the skin tissue (C).

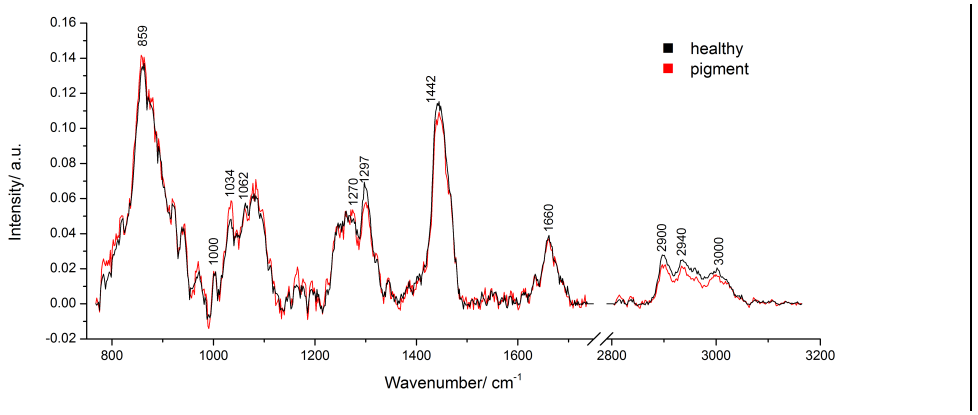


Fig. 7 Mean Raman spectra differentiating healthy and red pigmented areas on the pork skin sample shown in Fig. 6. Prominent Raman peaks are labeled (for details see text).

microscopy glass slide (Fig. 4B) and the mismatch between the proximal and distal surfaces was determined in analogy to the tape (Fig. 4A). This analysis also reveals a lateral resolution of 13 µm.

4.2 Raman characterization

In order to characterize the lateral resolution of the Raman modality with the achromatic lens doublet a raster scan was performed on a thin Teflon layer. The step size of the scan was set to 20 µm and a map with a dimension of 20 x 500 pixels was collected. Subsequently the generated image was analyzed for intensity variations at the representative Teflon Raman peak at 338 cm^{-1}. The lateral resolution was defined as the intensity variation from 10% to 90% of the integrated peak area, as shown in Fig. 5A resulting in an achievable resolution of 104 ± 6 µm for the Raman part,

which is in agreement to the core diameter of the Raman excitation fiber of 105 µm.

To characterize the depth of focus a thin layer (100 µm) of transparent scotch tape was measured over a length of 27 mm on the z-axis. Several Raman spectra in several focal positions were measured with a distance of 0.225 mm between consecutive points. Subsequently the data set was analyzed for intensity variations of the scotch tape Raman peak at 493 cm^{-1} and the depth of focus (DOF) was set to the full width half maximum of the peak intensity as depicted in Fig. 5 B resulting in a DOF of 5.8 mm. In conclusion these studies resulted in a sample penetration depth limited DOF of about 1 mm for 785 nm [34]. The focal volume thus can be visualized as having a high resolution laterally (~ 100 µm) and a low axial resolution (~ 700 – 1000 µm).

4.3 Skin tissue measurements

For validating our combined OCT/RS setup for later skin and skin cancer applications a pork skin sample with a red pigment on the surface was chosen as a model for skin studies. Fig. 6 displays the white-light images (Figs. 6A and B) as well as a B-scan through the sample area (Fig. 6C). The axial resolution of the OCT system was 9 µm allowing for the observation of morphological details of layer variations beneath the pork skin as can be seen in Fig. 6C.

It is obvious that the wavelength cutoff of the used galvanic mirror, which reflects all wavelengths higher than 650 nm, has an impact on the sample image quality and the pigmented area is barely visible in the white-light image shown in Fig. 6B. The tissue boundary is visualized by the red dotted line and the OCT B-Scan course shown in Fig. 6C is indicated by the black dotted line. The B-scan displayed in Fig. 6C shows a single tissue layer highlighted with a white arrow. Therefore we conclude that the red structures are a subcutaneous hemorrhage of the skin. The defect has a layer thickness of about 30 – 40 µm. Therefore ten Raman spectra inside the pigmented area as well as outside with a margin of 1 mm were recorded in order to analyze this red pigmented area in more detail on a molecular level. The mean Raman spectra derived from the ten spectra which were acquired from the hemorrhage and the skin region with a margin of 1 mm are shown in Fig. 7.

The main difference, that can be seen within the Raman spectra is a loss in intensity of CH-related modes (1298, 1443, 2850 - 3000 cm^{-1}). Skin mainly consists of fat. Due to the narrowness of the hemorrhage (35 µm) in comparison to the DOF (~ 700 – 800 µm), no obvious spectral components of the Heme-groups are visible. All expected Raman spectral features of skin (Amide I (1660), Amide III (1270), Nucleic Acids (1030) and Phenylalanine (1000)) are clearly visible and in agreement with the literature [28, 29].

5 Conclusion

The manuscript reports the successful implementation of a combined OCT/Raman device that is able to perform OCT scans and Raman maps or single point Raman measurements on bulk tissue samples. The most suitable optical system is an achromatic lens doublet, which represents a compromise between high OCT source penetration in tissue and high Raman signal collection efficiency. Furthermore this lens has a minimal intrinsic Raman background and showed a larger signal to noise level for the Raman part as compared with common OCT objectives. The 3D scans obtained from the OCT system can also provide axial (depth) information with a resolution of ~10 µm. By adjusting the image contrast post-acquisition, it is possible to clearly view the margins between different tissue types that would essentially help the user to better identify any abnormalities and the penetration depth of these. Essentially, this device is able to carry out fast scans to gather morphological information with OCT that helps the user identify abnormalities and then take pointwise Raman spectra for molecular diagnostics of the concerned region at a slower rate. One drawback of the system is the low axial resolution of the Raman part which is penetration depth limited to 700 – 1000 µm depending on the tissue type. This will have an impact on the model classification accuracies (e.g. cancer vs. non-cancer) since not only the tissue layer of interest can be measured. Hence, the Raman spectra are the result of a superposition of the Raman information of the different tissue layers. On the other hand, the system allows acquiring Raman spectra with short integration times and high SNRs from any point of large sample areas.

The optical setup can be potentially employed to characterize the surface of pathological tissue such as diseased skin tissue or to monitor wound healing processes. Having the advantage of being able to view cross sectional images via OCT and then carrying out diagnostic measurements with Raman spectroscopy would aid the user in making accurate diagnostic decisions. Further studies must be conducted to investigate the feasibility as well as the specificity and sensitivity of such a system.

Acknowledgments

Financial support by the Carl- Zeiss Stiftung is greatly acknowledged.